Toward Navigation Grade Acousto-Optic Gyroscope

Submitted in partial fulfillment of the requirements for

the degree of

Doctor of Philosophy

in

Electrical and Computer Engineering

Ashraf A. Mahmoud

B.S., ECE, Ain Shams University (2011)

M.S., Engineering Physics, Ain Shams University (2016)

Carnegie Mellon University

Pittsburgh, PA

February, 2020

ACKNOWLEDGEMENTS

First, I would like to thank my advisors, Professor Gianluca Piazza and Professor Tamal Mukherjee, for the priceless opportunity they offered me, and their constant guidance and support through the entire doctorate program. As mentors, they taught me valuable lessons which go beyond the mere technical knowledge. I will always admire their passion about scientific research and their vision. It was an honor to be one of their students.

I would also like to thank Professor James Bain and Dr. Igor Prikhodko for serving in my defense committee. Their suggestions and feedbacks have been fundamental in finalizing the present work.

I am thankful to all the present and past members of the PMaNS lab, and all the colleagues I had the honor to work with: Mohamed Mahmoud, Lutong Cai, Shafee Khan, Enes Calayir, Changting Xu, Ayaz Masud, Pietro Simeoni, Abhay Kochhar, Zachary Schaffer, James Best, Gabriel Vidal-Álvarez, Jitendra Pal, Hoe Joon Kim, Emad Mehdizadeh, Yuyi Shen, Mohammed Darwish, Matts Forssell and Jay Reddy.

As a CMU Nanofab enthusiast, I am deeply grateful to Matthew Moneck, Mark Weiler, Norman Gottron, Mason Risley, James Rosvanis, and Dante Boni for their hard, meticulous work, their patience and the precious suggestions they always shared with me.

Among my Pittsburgh friends, I would especially like to thank Mohamed Abdelmoula, Ahmed Hasan, Ahmed Abdelgawad and Ahmed Badwy for their unconditional friendship and support who made me feel at home. I am thankful to my parents, Ahmed Mahmoud and Eman Hasan, my siblings, Engy, Ehab and Ashrakat, and my lifetime friends, in particular Mohamed Tarek and Abdelrahman Ali, who supported me and encouraged me throughout this journey.

Finally, I would especially like to thank my family. My wife, Zinab has been extremely supportive of me throughout this entire process and has made countless sacrifices to help me get to this point.

This work was fully funded in the framework of the PRIGM-AIMS Project by the Defense Advanced Research Projects Agency (DARPA) under Award No. N66001-16-1-4025 .

To all the people who have supported me along this journey.

ABSTRACT

Accurate control of navigation is critical for many existing and emerging applications such as military missions, self-driving cars, pico-satellites and drones in high G-shock events and high-vibration environment. Precise and accurate navigation is made possible by the use of GPS. But what if GPS service is not available at all? This could happen due to several reasons related to the nature of the GPS communication as an RF signal. In those situations, the denial of GPS drives navigation systems to rely on the other systems.

Inertial Navigation Systems (INS), which rely on using inertial sensors such as gyroscopes and accelerometers, are a potential approach to achieve navigation in GPS-denied environments. Commercial MEMS INS have a small form factor and power consumption suitable for the emerging applications while they suffers from noise and drift. Tactical and navigation grade optical INS show better performance but at the expense of size and power. This leads to a technological challenge and opens research opportunities targeting the decrease of noise and increase of stability of inertial sensors at low power consumption and small form factor.

In this dissertation, we focus on one type of MEMS inertial sensors, namely a gyroscope, to enable positioning, navigation, and timing (PNT) in GPS-denied environments. We invented and demonstrated a new type of gyroscopes called the acousto-optic gyroscope (AOG). The AOG is based on the idea of the surface acoustic wave gyroscope (SAWG) but uses a photonic read-out to decrease input referred noise and increase signal stability.

The AOG offers well established performance in terms of high G-shock survivability, low g-sensitivity, and wide operating bandwidth. The AOG experiences challenges in achieving high sensitivity due to the relatively small Coriolis force. In the present work, the sensitivity of AOG and long-term stability are investigated.

Finite element and analytical methods are used to optimize the design of the AOG. These investigations resulted in improvements in AOG sensitivity by acting on the Coriolis mass and the quality factor of SAW resonators. Similarly, a fabrication process was developed to ensure that large masses could be synthesized and device non-idealities reduced.

The results of these investigation lead to the 1st functional prototype of both SAWGs and AOGs, which exhibited low noise to signal ratio expressed as angle random walk (ARW) as low as 0.25 $°/\sqrt{hr}$ are demonstrated.

Long-term stability was also studied using a monolithically integrated micro-oven, which helped maintaining the temperature and operating frequency variations within $\pm 10\mu K$ and$\pm 0.2\ ppm$, respectively. This study eliminated the impact of temperature and stress induced drifts, showing that these devices can attain record breaking stability up to 300 sec. SAW resonators were also tested at CMU and ARL surviving high G-shock of more than 50,000 Gs.

TABLE OF CONTENTS

LIST OF TABLES

LIST OF FIGURES

CHAPTER 1: INTRODUCTION

1.1. Motivation

Accurate control of navigation is critical for many existing and emerging applications such as military missions, self-driving cars, pico-satellites and drones. A breakthrough took place in navigation with the invention of longitude and clock [1] followed by the invention of gyroscopes. Since then, the resolution and accuracy of clocks and gyroscopes have been important factors in precise navigation [2].

Precise and accurate navigation is made possible by the use of GPS and inertial navigation systems. Fig. 1.1 shows the system block diagram of a modern navigation system where two methods of navigation are used. The first is trilateration based on distance calculation using GPS and the second is dead reckoning using an inertial navigation system (INS) formed by gyroscopes and accelerometers. Both systems are very advanced but come with limitations that could be compensated for by the other. On one hand, GPS has a low data rate in the range of 1-10 Hz [3] while INS has a higher rate in the range of 100-500 Hz. On the other hand, inertial sensors can detect only rate of change, so the position and orientation of the navigating body are calculated using numerical integrations. Since integration is a cumulative process, noise or drift in the sensor output will accumulate leading to a wrong estimation of position, which worsens over time [4]. A new type of gyroscopes called whole angle gyroscope based on Foucault Pendulum is developed to overcome the error integration issue where the sensor output is the angular position. Unlike rate gyroscope, this gyroscope runs in a free running mode, therefore requiring a high quality factor. In addition, the drive vibration is propagating radially which imposes very strict requirements on the symmetry of the device [5]. Due to the previous reasons, whole angle gyroscopes are still in the research and development phase. GPS is used to calibrate

the reading of the INS, but because of its low data rate, the navigation system cannot rely exclusively on the GPS information. But what if GPS service is not available at all? This could happen due to several reasons related to the nature of the GPS signal like navigation in underground, deep ocean, near tall buildings where RF signals cannot penetrate or in a battlefield where RF signals could be jammed [6]. In those situations, the navigation system can only rely on the INS, leading to a technological challenge and opening research opportunities targeting the decrease of noise and increase of stability of inertial sensors.

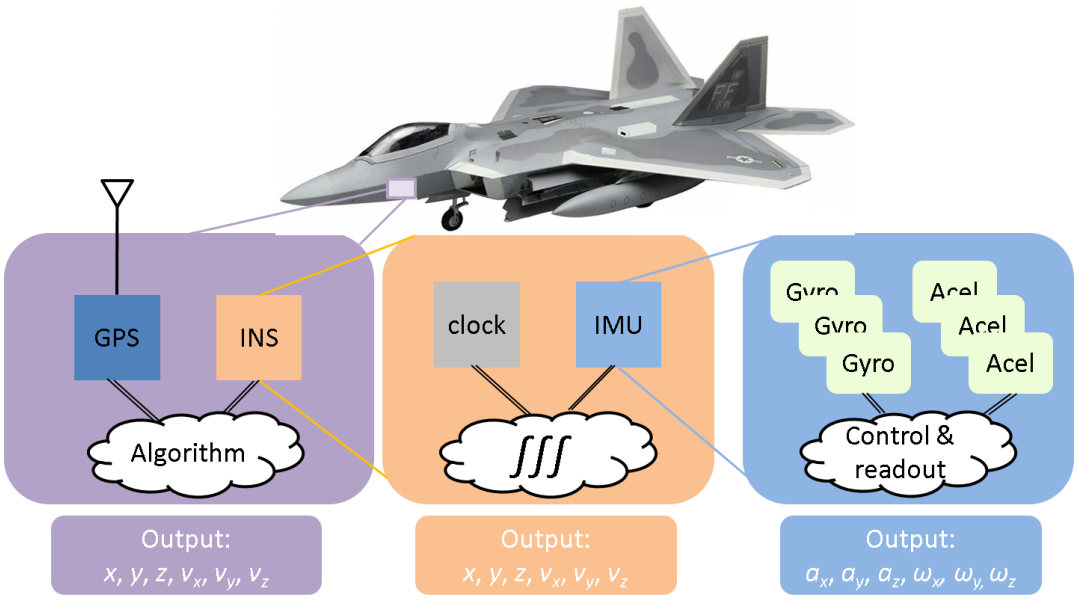

Figure 1.1: Block diagram of modern navigation system showing the different components and stages required to get reliable localization and attitude.

In this work, we focus on one type of inertial sensors, namely a gyroscope, to enable positioning, navigation, and timing (PNT) in GPS-denied environments. The focus of the research is on advanced inertial micro sensor technologies for future gun-hard, high-bandwidth, high-dynamic-range, GPS-free navigation. Specifically, we are called to explore alternative technologies and modalities for inertial sensing [7]. The thesis is focused on investigation and development of a new and alternative methods of building a gyroscope. The technology provided is expected to be used in future military and aerospace

applications such as smart long-range ammunition and micro-nano satellites and many aerial vehicles.

Table 1.1 summarizes the specifications of state-of-the-art gyroscopes. The gyroscope market is dominated by two types of gyroscopes, MEMS vibratory gyroscopes (MVG) and optical gyroscopes (OG . Table 1.1: Summary of the specifications for state-of-the-art gyroscopes

	Type	**ARW ($o/\sqrt{h}$)**	**Bias Instability (o/hr)**	**$\tau_{stability}$ (sec)**	**Power**	**Size (mm)**	**Shock (kG's)**	**Frequency**	**BW**
[8]	MVG	35	15	~50	Few μW	2.8x2.8	< 2	~10 kHz	125 Hz
[9]	MVG	6e-3	0.64	105	Few μW	6x5	low	7 kHz	100 Hz
[10]	RLG	20e-3	<0.1	-	2500 mW	34x34x34	-	Optical	-
[11]	HRG	4e-4	5e-3	-	4000 mW	37x37x33	3	Few kHz	-

MVGs have low cost (< $1), power (micro Watts) and small size (few mm per side). Research breakthroughs have led to lower noise MVGs resulting in decreased angle random walk (ARW) and bias instability, at the expense of increased Coriolis mass, thus decreased shock survivability and limited operating bandwidth. On the other side, OGs show outstanding noise performance and shock survivability at the expense of power (in Watts), size (tens of cm) and cost. The specifications dictated by the emerging applications require merging the advantages of both MVGs and OGs in a single device.

In this thesis, we focus on a different type of Coriolis based gyroscope using surface acoustic waves (SAW) combined with a high sensitivity optical read-out. The basic building block in acoustics is the interdigitated transducer (IDT). Fabricated on a piezoelectric substrate, it is capable of converting electrical signal to mechanical

propagating waves and vice versa. For better energy confinement and to achieve mechanical resonance, acoustic reflector gratings are used at both sides of the IDT. As shown in Fig.1.2, the vibration induced by the SAW are used to oscillate small masses placed at the locations of max displacements (in-plane or out-plane) and acting as the proof mass of the vibrating mass of the gyroscope. If an input rotation is applied orthogonal to the mass vibration, Coriolis force is induced; the forces on all the masses add because they are laid out in a specific checkerboard configuration. The overall induced force generates a secondary wave orthogonal to the drive wave and is detected by another IDT.

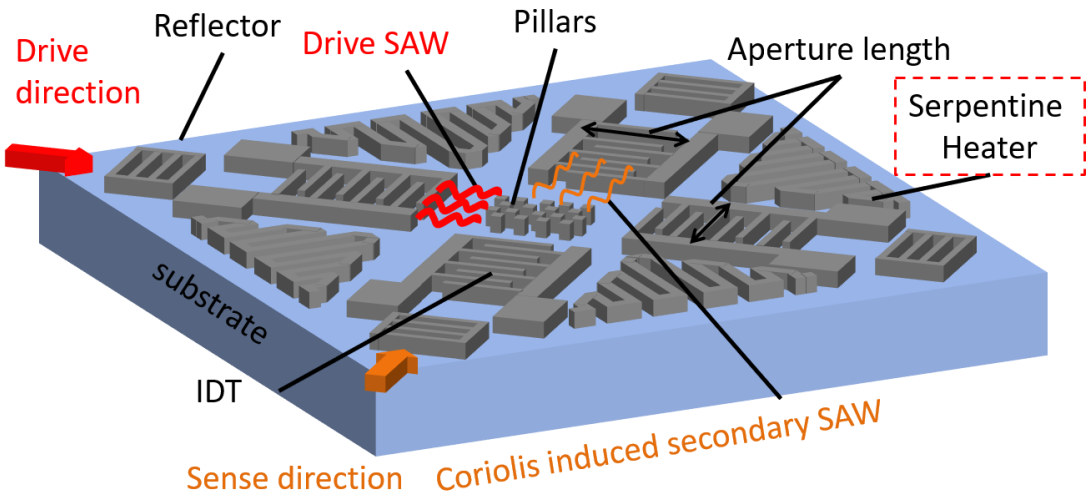

Figure 1.2: Graphic representation of the proposed SAWG.

The idea of this device has been previously introduced but all previous work did not result in working prototypes [12-13]. In this thesis, we present the design innovations we introduced to make the surface acoustic gyroscope (SAWG) exhibits a high sensitivity and successfully measure gyroscopic effects. In addition, we developed a new type of gyroscope called the Acousto-Optic Gyroscope (AOG) using SAWG and optical readout to combine both advantages of MVG and OG.

The AOG (shown in Fig. 1.3) is a promising type of gyroscope that has a great potential in meeting the specification required by emerging applications. Compared to MVGs, AOGs operate at high frequency (10s to 100 of MHz), which makes them immune to

environmental vibrations and provides wide bandwidth in matched mode operation. In addition, AOGs do not have released structures; a feature which significantly increases their shock survivability. Compared to OGs, AOGs have a smaller form factor and lower power consumption. The other advantages of the AOGs over a pure SAWG implementation are lower quadrature and higher stability due to the physical decoupling between the acoustic driving and optical sensing which was demonstrated in [14].

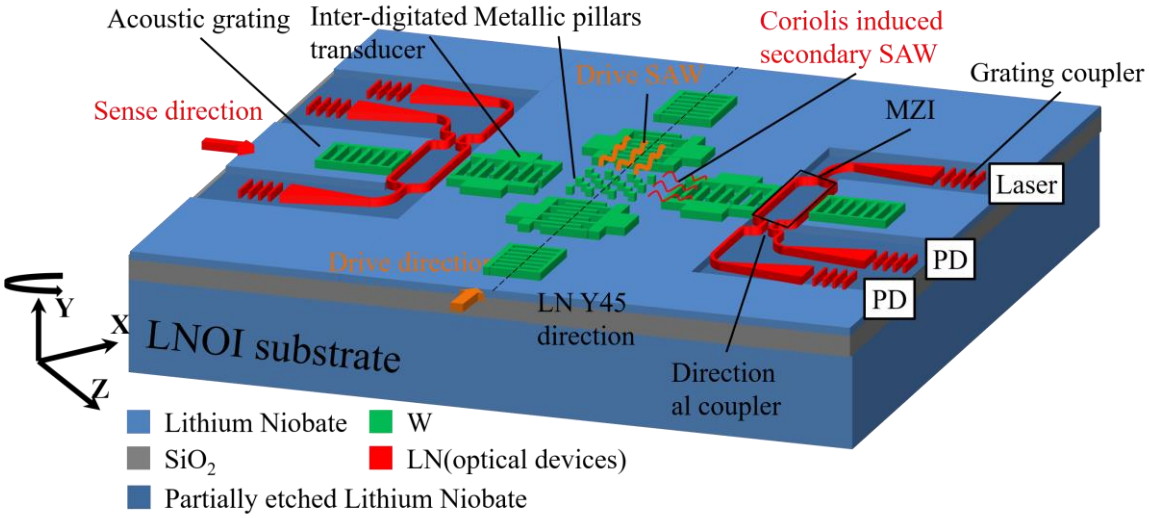

Figure 1.3: Graphic representation of the proposed AOG.

1.2. SAWG Literature Review

The concept of the SAWG was first introduced in [15] for an in-plane rotation pitch/roll gyroscope. It is a Coriolis based gyroscope which senses amplitude modulated wave induced due to the applied rotation. The schematics in the study showed the detailed operation and design parameters in both the drive and the sense directions. However, the fabricated prototype could not capture any gyroscopic behavior. It suffered from significant frequency mismatch between the drive and sense responses in addition to the weakness of the sense response. The work in [16] was the first to theoretically analyze and study the SAWG. It also considered its non-idealities such as wave scattering due to pillars and design techniques to mitigate it. However, this previous study considered only a traveling wave neglecting the wave amplitude boosting achieved using standing waves in a cavity.

Based on the previous considerations, the conclusion of that study was not recommending the SAWG as a high-grade inertial solution. The research done in [17] showed a sensitivity plot of the gyroscope but the noise performance was never characterized. Sensing was performed using an IDT instead of a cavity resonator, which has a significant impact on lowering the measured sensitivity. The concept of using two cavities for driving and sensing the SAWG was first introduced in [18]. The focus of the work was to have a two axes gyroscope capable of capturing both pitch and roll rotations by alternating the control signals of the cavities. The work discussed the concepts and the SAW designs but didn't provide measurements or characterization to verify the concept. In parallel to the amplitude modulated SAWG, a different type of SAWG was developed. It was designed to sense frequency modulation induced by input rotation. The idea was first developed in [19]. The highest reported performance of this gyroscope was $ARW \sim 33\ °/\sqrt{hr}$ and Bias instability $> 20^3\ °/hr$ which is far from fulfilling even consumer grade performance [20]. In addition, the structure of this device cannot be modified to include a photonic readout system. Due to all the previous considerations, we adopted the amplitude modulation SAWG technique and modified its design, process and system with photonic integration to enhance the gyroscope's sensitivity and stability.

1.3. Thesis Contributions and Outline

In summary, this PhD thesis is making the following contributions in advancing the state-of-the-art:

1. Enhancing the performance of SAWG in terms of sensitivity, damping loss minimization, and reducing its fabrication complexity and form factor by means of:

- Comprehensive analytical modeling and numerical simulations of SAWG. The analytical model captures the ARW of the sensor and the impact of the different design parameters on the noise performance and sensitivity.

- Demonstration of inherently matched operation of a SAWG leading to sensitivity boosting, reduction in the ARW, immunity and high rejection of common mode temperature and process variations [21].
- Modeling and design of efficient acoustic reflector gratings achieving record-breaking reflectivity and low intrinsic loss in a compact form factor using thick Tungsten (W) metal array (MA) and groove array (GA) designs [22].
- Comprehensive study of loss mechanisms in SAWG (radiation, beam steering, diffraction, bulk scattering and resistive loss) and various techniques to mitigate them and boost the SAW resonator's quality factor. Radiation loss was reduced by increasing acoustic reflector grating reflectivity and integration of metal array and grove array reflectors in a single structure. Diffraction loss was reduced by increasing the aperture while beam steering was solved by the skewing of the resonator structure. Resistive loss was minimized by the modification of the deposited film properties.
- The development of a simple and self-aligned SAWG fabrication process, which ensures high-yield manufacturability of the proposed device.

2. The first demonstration and testing of an AOG by system integration of SAWG for pillar driving with photonic read-out for gyroscope detection. Development of advanced control system of the AOG for noise rejection and enhancement of long-term stability by applying the following:

- System integration and testing of Mach Zehnder Interferometer (MZI) photonic read-out on Lithium Niobate over Insulator (LNOI) substrate achieving drive and sense decoupling, low quadrature and stable Zero-Rate Output (ZRO) [23].
- System integration and testing of photonic resonator such as race-track (RT) for sensitivity boosting exploiting optical field enhancement factor [24].

- Monolithic integration of W heaters on LNOI substrate for ovenization and thermal control leading to the minimization of thermal drift and long-term stability [25].
- Development of differential sensing system for common mode noise rejection [14].

The thesis is organized in the following chapter. In Chapter 2, the principle of operation of SAWGs and AOGs are explained. A parametric study was performed to serve as a guide for the optimization of design parameters and roadmap for modifications and enhancements. Different photonic systems are discussed while highlighting the pros and cons of each.

In Chapter 3, we demonstrate the various fabrication process techniques used to apply the design modifications and enhancements both in the acoustic and photonics parts. The challenges faced during assembly and packaging are also discussed in this chapter. In Chapter 4, the control system used to drive the gyroscope and sense the gyroscopic output is explained for both SAWG and AOG. In addition, the efforts to integrate optical source and detector on chip are discussed. Chapter 5 discusses the testing and characterization of both SAWG and AOG. In this chapter, the testing setup are used for gyro characterization are demonstrated showing the modification done to accommodate for SAWG, AOG and integrated AOG testing requirements. Then, the testing procedure of the gyroscope and techniques used to extract the performance are discussed. The survivability of the gyroscope is demonstrated using high shock testing of the SAW components. Finally, in Chapter 6, the entire body of the Ph.D. work is summarized, and some future research directions are presented.

CHAPTER 2: Design and Modeling

In this chapter, the analytical and FEM techniques used to model the sensor phenomena and the device components are demonstrated. We also explore the design space of SAWG and AOG showing the effect of the design parameters of various components and their effect on the final performance of the gyroscope.

2.1. Surface Acoustic Wave Gyroscope (SAWG)

In this section, the principle of operation of the SAWG is explained showing the functionality of each component. In addition, a parametric study is performed to serve as a guide for the optimization of design parameters and roadmap for modifications and enhancements.

2.1.1. Principle of Operation

As shown in Fig. 2.1, the SAWG consists of two orthogonal SAW resonators, sharing a common cavity with metallic pillars placed at the center of the cavity. The pillars act as the Coriolis mass of the gyroscope.

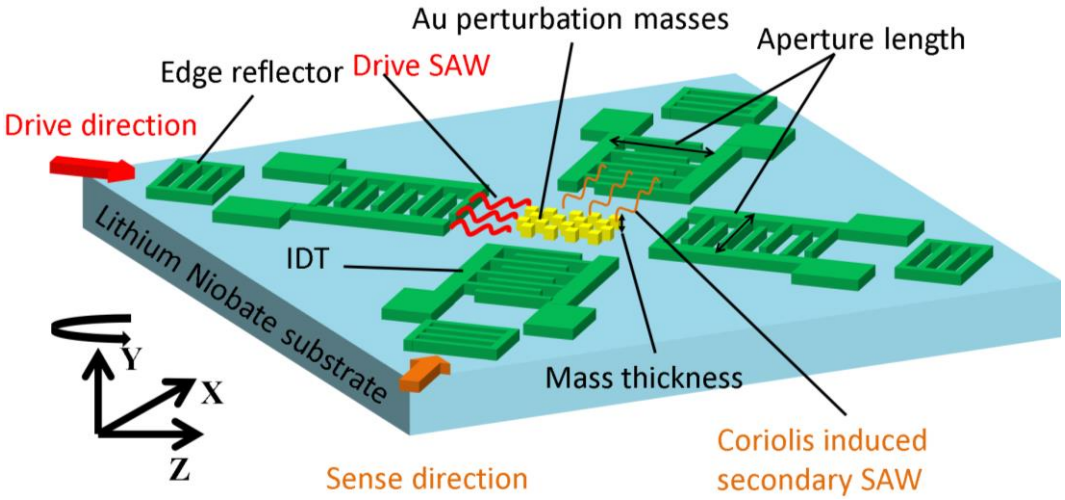

Figure 2.1: 3D sketch for the inherently matched SAWG of this work (IDT=InterDigitated Transducer).

A SAW standing wave pattern is established along the drive direction where pillars are driven into longitudinal vibrations with velocity v_p. When an out-of-plane rotation, Ω is

applied, a Coriolis force, F_{cor}, is induced on the vibrating pillars in the direction orthogonal to both the input rotation direction and the drive vibration direction as expressed in (Eq. 2.1).

$$F_{cor} = 2m_p\Omega \times v_p \tag{2.1}$$

The pillars are arranged in a checkerboard configuration such that constructive interference for a secondary SAW wave is established in the (sense) direction as shown in Fig 2.2.

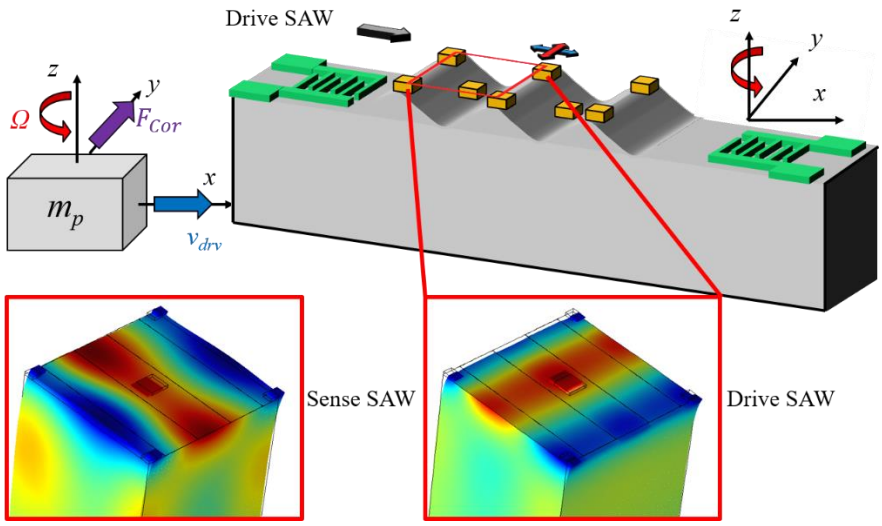

Figure 2.2: Cartoon showing the driving mechanism in SAWG and how the secondary wave is generated.

The secondary SAW wave is converted to a voltage using IDTs. Their functionality and design are discussed in section 2.3.2. For SAW wave amplification, the secondary wave is confined in an acoustic cavity using acoustic grating reflectors. The design and innovative techniques used to implement the gratings are discussed in details in section 2.3.4. Operating the cavity at resonance frequency, the cavity has the ability to amplify the amplitude of the wave with an amplification factor proportional to the quality factor of the cavity. This motivated us to study the quality factor and sources of losses in the SAWG in order to achieve maximum quality factor and eventually maximum sensitivity. The different loss mechanisms and the techniques to mitigate them are discussed in section 2.3.6. To solve the frequency matching and sensitivity issues faced by the initial SAWG

designs (presented in section 3.1.1), the SAWG was fabricated on a Y-cut Lithium Niobate (LN) substrate at ±45º from the Z-direction. The detailed study and analysis behind this orientation is discussed in details in section 2.3.1.

The principle of operation of the SAWG was first verified using FEM COMSOL Multiphysics simulations where coupled electric and structural mechanics modules were used. In 3D simulation, a unit wavelength (Λ) was simulated using periodic boundary conditions (PBC). The SAW wave was excited using virtual electrodes to simulate exactly a Λ pillar unit and still able to provide excitation force. Under applied input rotation rates of various amplitudes, Coriolis force induced on the pillars was recorded. In another simulation, a force simulating Coriolis force was applied to the pillars generating a SAW wave that was converted to output voltage by an IDT. As shown in Fig. 2.3, the displacement and the output voltage are linearly proportional to the rotation rate. In addition, the Coriolis signal is directly proportional to the pillar mass as expected from Eq. 2.1.

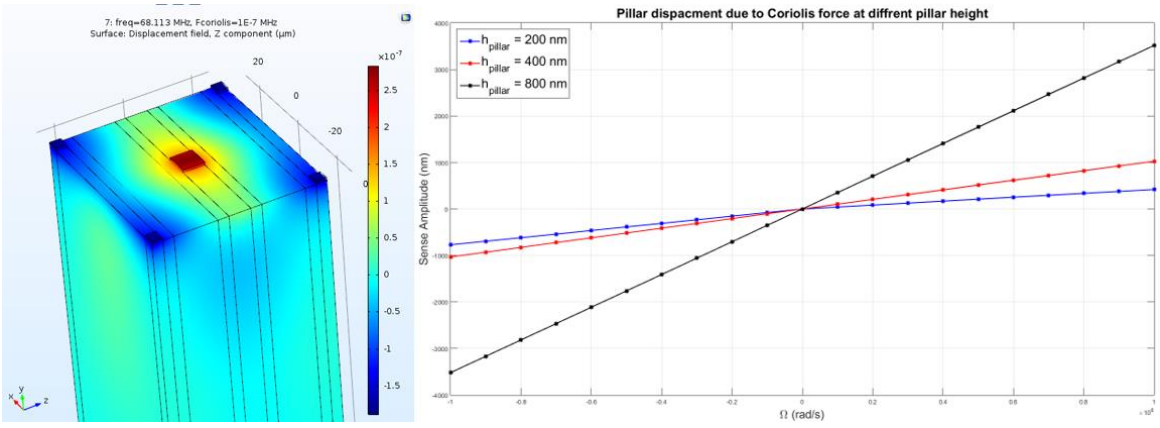

Figure 2.3: COMSOL simulations to verify the SAWG principle of operation where the a) is the test setup while b) is the extracted scale factor for various pillar mass.

2.1.2. Parametric Study

To achieve navigation accuracy while measuring through a high-shock event, there is a need to enhance SAWG noise performance, specifically lower Angle Random Walk

(ARW), bias instability and long term stability (drift) while maintaining a small form factor. ARW is defined as noise to signal ratio. It is a well know metric in the inertial sensors community to represent minimum detectable rotation rate limited by noise. Considering a white noise model cause by Brownian (mechanical) noise, ARW was derived as in Appendix B where the final formula is given by:

$$ARW = \omega \sqrt{\frac{2KTM_{res}}{m_p Q_{drv} Q_{sns-eff}\ P_{in}}} \tag{2.2}$$

Where ω is the angular resonance frequency of SAW, K is is Boltzmann constant, T is temperature in Kelvin, M_{res} is the effective mass of the drive resonator, m_p is the total effective mass of the pillars, Q_{drv} and Q_{sns} are the drive and sense quality factors and P_{in} is the input electrical power. In the equation for the ARW, we can assume that the sense and drive resonators are perfectly matched so that the resonator Q in the drive and sense directions can be fully harnessed. Using (Eq. 2.2) was rewritten as a function of design parameters only given by Using (Eq. 2.3) where κ_1 is a constant, ρ_{LN} and ρ_M are the densities of LN and the metal pillar, v_o is the surface velocity of SAW, H is the penetration depth of the SAW, F_m is the mechanical reflectivity constant, N_p and N_{IDT} are the number of pillars and IDT fingers while α is the ratio of pillar thickness to Λ.

$$ARW = f(\alpha, \Lambda, Q, N_p, P_{in}) = \kappa_1 \frac{1}{\Lambda Q} \frac{1}{\sqrt{p_{in}}} \frac{1 + \alpha\kappa_2}{\alpha^2 \sqrt{N_p}} \tag{2.3.a}$$

$$\kappa_1 = \frac{16\pi\rho_{LN} v_o H}{\rho_M F_m} \sqrt{KT}, \kappa_2 = f(N_p) = 2F_m \left(\sqrt{\frac{N_p}{2}} + N_{IDT} \right) \tag{2.3.b}$$

Using (Eq. 2.3), a parametric study of the effect of wavelength, number of pillars, thickness of pillars and power in minimizing ARW was developed as shown in Fig. 2.4. The values of the physical parameters used in this analysis were extracted from actual measurements of initial SAW resonator designs on Y-cut $\pm 45°$-direction on LN for which the maximum

Q measured was 14k. The study shows how the ARW decreases with the acoustic wavelength to a point where the SAWG is capable of achieving navigation grade performance in a small form factor (shaded operating region in Fig. 2.4.a).

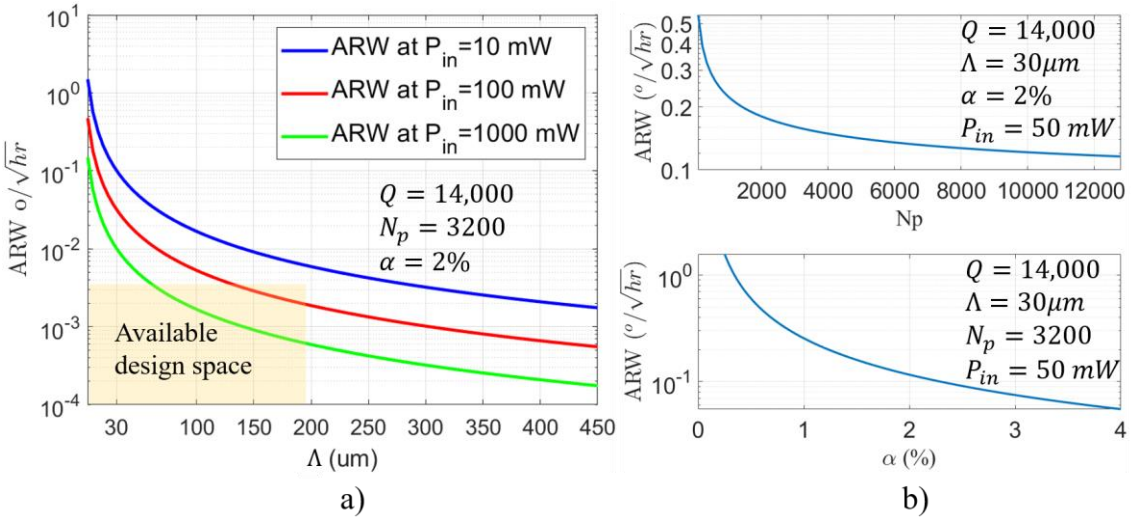

Figure 2.4: Parametric study of ARW for SAWG capturing the changes in ARW with various parameters where a) study Λ variation at three values of power,10mW, 100mW and 1000 mW while b) study the N_p and α variation.

According to this study, there is a need to drive pillars with higher mass using higher power to achieve higher displacements and boost the sensitivity. In section 3.1.2, we show how we modified the fabrication process to use low electromigration, high power handling and high mass density metals such as Tungsten (W) to achieve this purpose. The measurements of the SAWG that verify the impact of the cavity size on the total mass of pillars and sensitivity are demonstrated in section in section 5.2. In addition, we demonstrate in section 2.3.6 all the analysis and the efforts to minimize the acoustic losses and boost the quality factor of the SAW resonator.

2.2. Acousto-Optic Gyroscope (AOG)

In this section, the principle of operation of the AOG is explained showing the functionality of its components. In addition, different photonic systems are introduced showing the pros and cons of each approach.

2.2.1. Principle of Operation

The AOG is based on the concept of the SAWG, in which the Coriolis force detection is performed optically instead of acousto-electrically. The optical sensing can provide extremely low noise levels, gain boosting by field enhancement, and physical decoupling of the drive and sense mechanisms leading to low quadrature and stable readout. In addition, the optical modulation method significantly simplifies and relaxes the dynamic range requirement of the electronic readout. For acoustic and photonic compatibility, a new substrate was used composed of thin film LN over insulator (LNOI) [26].

The insulator is made of SiO_2 which acts as a cladding material due to its low refractive index ($n_{SiO_2} = 1.44$) compared to that of LN ($n_{LN} = 2.2$). The acoustic devices are built on the surface while the photonics are patterned by partially etching the top thin film as shown in Fig. 2.5.

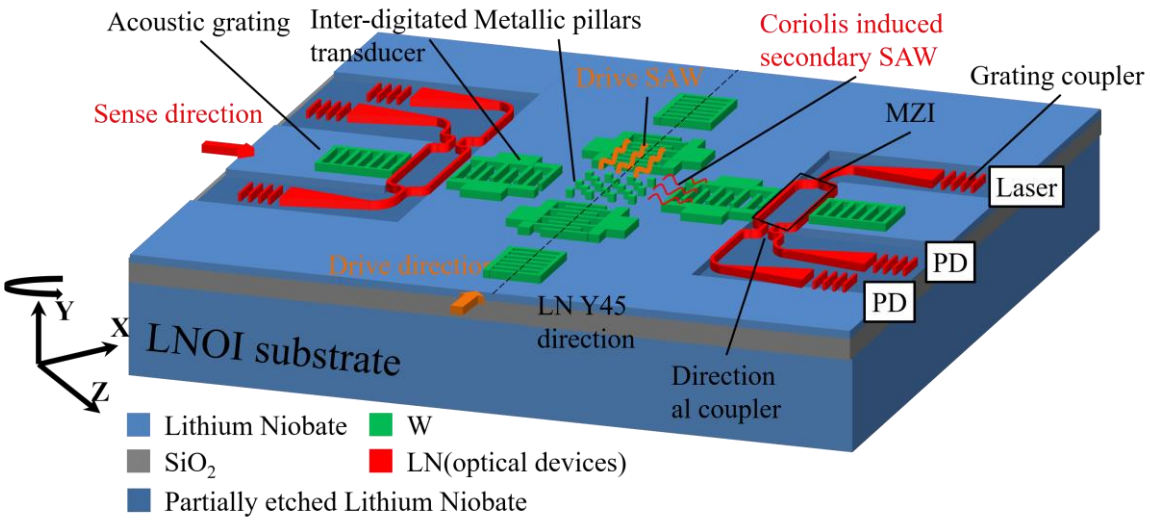

Figure 2.5: 3D sketch for the AOG showing the acoustic and optical components on LNOI substrate.

The strain accompanying the secondary wave is modeled as:

$$S = \frac{F_{cor}}{\rho v_o LH} \tag{2.4}$$

Where ρ the mass density of LN is, v_o is the SAW velocity, L is the interaction length and H is the SAW penetration depth. Due to the acousto-optic (AO) property in LN [27], the strain accompanying the secondary wave changes the optical refractive index as in (Eq. 2.4). Depending on the photonic readout used, Δn is translated to amplitude or phase modulation in the optical domain.

$$\Delta n = \frac{1}{2} n^3 p^{eff} S \tag{2.5}$$

2.2.2. Photonic Readout Systems

The photonic readout was implemented using two major photonic components: the MZI and the RT resonator. The devices were designed to operate at 1550 nm optical wavelength due to the availability of commercial laser and photodetectors at this wavelength. As shown in Fig. 2.6, the MZI was used where the wave modulates its arms differentially and generates differential phase difference at the output. The arms of the MZI are separated by $\left(n + \frac{1}{2}\right)\Lambda$ where n is an integer $n = 0, 1 \ldots$ .The alignment of the MZI relative to the secondary SAW wave is crucial to harvest the maximum strain. For our yaw (Z-axis) gyroscope, The MZI arms are placed at the maximum in plane strain, which is $\Lambda/4$ away from the max in plane displacement. Through this arrangement, the maximum phase difference is given by $\phi_{max} = 2Q_{sns}\frac{2\pi}{\lambda}\Delta n$.

The major advantage of the MZI over a RT is its wide optical bandwidth, for which optical wavelength tuning and tracking is not as strict. The scale factor (SF) of the AOG is defined as the change in the optical transmission due to phase change between the arms of the MZI. According to the derivation done in [24], the SF_{MZI} is given by (Eq. 2.6).

$$SF_{MZI} = \left|\frac{\partial T_{MZI}}{\partial \Omega}\right|_{\max} = \left|\frac{\partial T}{\partial \phi}\right|\left|\frac{\partial \phi}{\partial \Omega}\right| = G_{MZI}\,\frac{2\pi}{\lambda H}\sqrt{\frac{M_2}{\rho v_R}}\,m_P\sqrt{\frac{P_{in}Q_{drv}}{\pi f_o M_{res}}}\,Q_{sns} \tag{2.6}$$

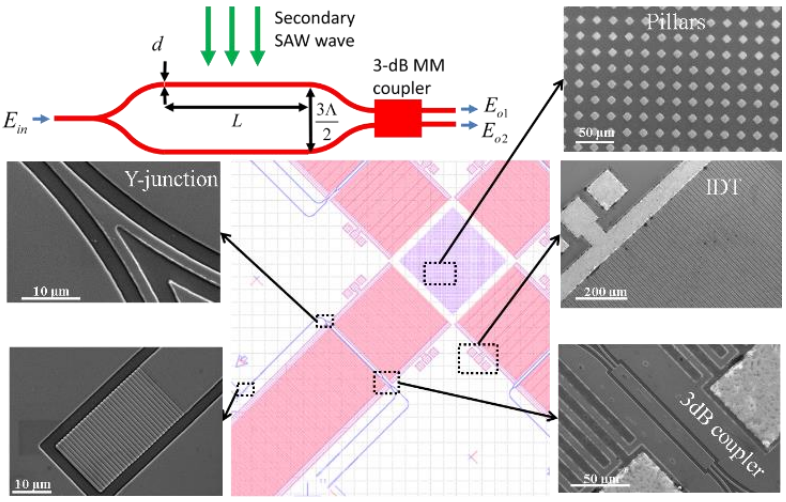

Figure 2.6: Layout view and SEM images showing various acoustic and photonic components of the AOG where the MZI is used.

Where $G_{MZI} = 2$ for a differential sensing MZI, $M_2 = \frac{n^6(p^{eff})^2}{\rho v_o^3}$ is the AO figure of merit of LN and it is a function of its material properties such material properties such as n (effective refractive index) and p^{eff} ,which is the acousto-optic coefficient.

The only drawback of the MZI is its low AO gain which has a direct impact on the sensitivity and noise performance. From (Eq. 2.6), is clear that the only parameters that could be optimized are those of the SAWG while the rest are either material constants or fixed by design. It could argued that decreasing λ can help in boosting the SF but this will soon be limited by lithography limitation in fabrication and the commercial availability of optical sources and detectors. To overcome the limitation of the MZI sensitivity, an optical RT is used as in Fig. 2.7, for which the acousto-optical gain is boosted due to the field enhancement in the optical resonator. This enhancement is effectively proportional to the finesse (F) of the optical resonator. As in [24], the gain of the RT was derived to be $G_{RT} = \frac{2}{5}F$ which has been demonstrated to be higher than G_{MZI} by almost two orders of magnitude.

Unlike the MZI, the RT resonator needs to be biased at the 3-dB point of the optical transmission for maximum sensitivity; thereby its operation is strongly affected by optical wavelength drift. In addition, the need for high F and low optical losses imposes additional design and fabrication challenges. In section 3.2, we show how some of those fabrication challenges were mitigated. In section 5.2, we demonstrate the testing systems of both MZI and RT and discuss the measurements and characterization results.

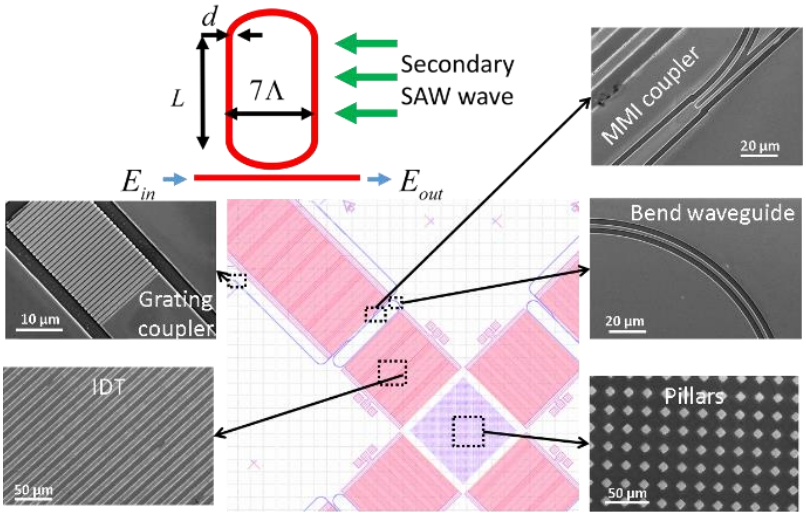

Figure 2.7: Layout view and SEM images showing various acoustic and photonic components of the AOG where MZI is used.

2.3. Acoustics

The optimization of the SAW components design is crucial in delivering high performance SAWG and AOG. In this section, we will demonstrate in details how to model, simulate and design various acoustic components and mitigate the challenges faced to achieve the target performance.

2.3.1. SAW in Piezoelectric Material

Various types of SAW waves were studied in literature such as Raleigh SAW [28], Leaky SAW [28] and shear horizontal-SAW (SH-SAW) [28]. In this thesis, we will focus only on Raleigh SAW and implement it in the SAWG design. The Raleigh SAW wave propagates

along the surface and decays exponentially into the bulk. The SAW consists of compressional and shear waves coupled together in a fixed ratio while there are no variations in the transverse direction. Due to the coupled nature of this wave, it is very hard to solve for them analytically, especially in piezoelectric materials. This type of SAW was first described by Lord Raleigh while the SAW wave solution in a piezoelectric material was first published in [29]. Due to the complicated nature of this wave, all the wave phenomena in this thesis are simulated using FEM COMSOL Multiphysics instead of being solved analytically.

In any SAW technology, the main design challenge consists in generating and controlling the wave itself. This cannot be done without understanding the parameters of the piezoelectric substrate and evaluating them. The major key parameters are the surface velocity, v_o, electromechanical coupling coefficient, K_t^2, transduction capacitance density, C_s , and surface parameters, c_x, c_y and c_z. The K_t^2 identifies how much electrical energy is coupled mechanically to the substrate. For efficient coupling, this value is required to be as high as possible. Concerning v_o it is important to have low v_o according to (Eq. 2.3.b). In a SAWG, we are more concerned about the relative velocity $\Delta v = |v_{drv} - v_{sns}|$ of the drive and sense resonators. The surface parameters define the actuation displacement due to surface potential and they play a very important role in designing SAW reflector gratings as shown in section 2.3.4. All the previous parameters vary from one piezoelectric material to another, so we need to choose the one that fits our designs and maximize our performance. There are various piezoelectric substrates and materials studied in literature [29] where the highest reported K_t^2 for Raleigh SAW was found to be in LN. For this reason, it was selected as the material for the implementation of the SAWG. All the previous parameters were extracted from COMSOL Eigen frequency simulations using piezoelectric Multiphysics, which couples structural mechanics and electrostatic physics.

As shown in Fig. 2.8.a, the test bench is basically an Eigen unit of one Λ with periodic boundary conditions (BPC) on both sides. Having a constant amplitude across the aperture, the wave was simulated only in 2D to reduce the number of mesh elements and simulation time. As shown in Fig. 2.8.b, a sweep of the wave propagation direction was first performed for Y-cut LN to extract its physical parameters.

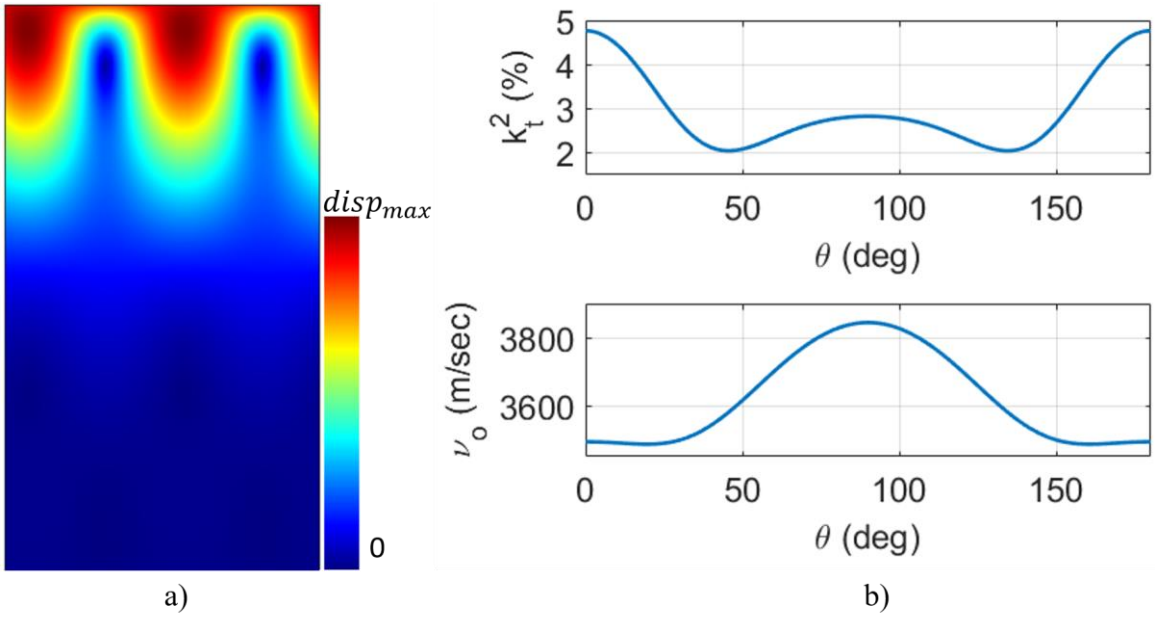

Figure 2.8: Extraction of material properties of LN where a) shows the SAW wave displacement of a 2D Eigen unit test bench built in COMSOL and b) shows some of the material parameters such as v_o and K_t^2 vs angle direction.

Previous SAW gyroscope designs targeted SAW propagation direction and LN wafer cuts that provide the highest K_t^2 such as propagating the SAW in the Z-direction for a Y128-cut LN wafer. However, for such a cut, material properties such as v_o are not the same in the two orthogonal in-plane directions X and Z due the trigonal crystalline structure of LN. In the previous SAWGs, the wavelengths were designed differently for X and Z directions to achieve frequency matching. However, fabrication variations affect both designs differently making frequency matching almost impossible. To solve this problem, we started looking for orthogonal crystal symmetry in LN where the dimensions of the acoustic wavelength could be kept the same so the effect of fabrication variations would cancel out.

To achieve that, we studied the properties of seven commercially available LN cuts as shown in Fig. 2.9. We found crystal symmetry in all the available five Y-cuts, Z-cut but not X-cut. In Y-cut wafers, the crystal symmetry mirrored around X axis at $\pm 45°$ relative to Z-axis while in Z-cut, the symmetry is repetitive every 120^o. It was found that Y-cut offers the highest K_t^2 , of all orthogonally symmetric cuts, making it the best candidate to be used in the design of the SAWG.

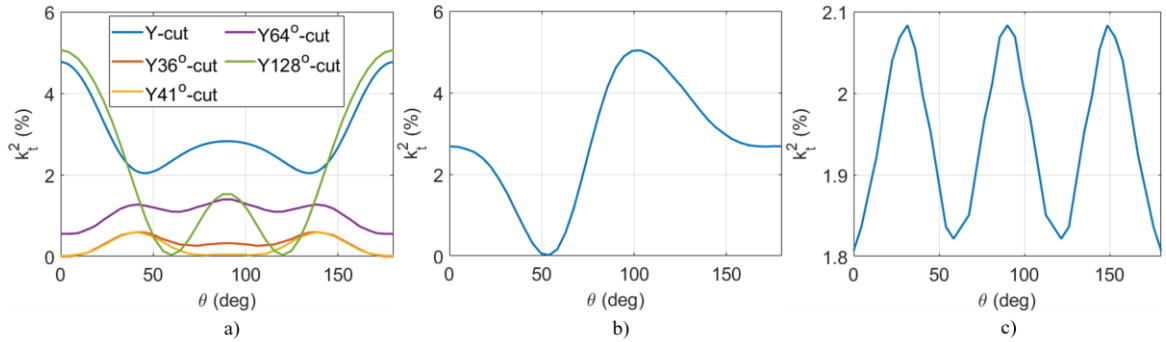

Figure 2.9: K_t^2 versus propagation direction of seven commercial LN cuts where a) show five Y-cuts, b) shows Z-cut while c) shows X-cut.

Since AOG operation depends on the acouto-optic phenomena, we need to select the material, cut and direction that gives us maximum acouto-optic coefficient p. It turns out that the optimization of the AOG p-coefficients lead to a Y-cut with 38 relative to Z-direction with a relatively flat change. So it turns out that the same cut for SAW orientation would work very well for the AOG.

Another challenge is that the AOG requires a cladding material to guide the optical signal in the photonic wave guide. Cladding was provided by air at the top of waveguide, whereas a material with low optical loss and refractive index smaller than that of LN was required below it. SiO_2 was found to be a good candidate since it has $n_{SiO_2} = 1.44$ and very low optical propagation loss [30]. Based on the previous considerations, LN over insulator (LNOI) platform was used by stacking LN thin film of $500\ nm$ above bulk Y-cut LN wafer with a SiO_2 film in between as shown in. The oxide thickness has a direct impact on

defining the optical wave confinement in the waveguide structures, which directly impacts the optical losses. The higher the SiO_2 film thickness, the lower is the optical loss. Unfortunately, this came at the expense of a huge reduction in K_t^2 due to the change in the vertical field caused by the introduction of SiO_2. Table 2.1 summarizes the values of K_t^2 for various SiO_2 thicknesses, t_{ox}, and SAW wavelengths, Λ. It was noticed that higher t_{ox} harms K_t^2 as expected. What is interesting is that the effect of t_{ox} lessen for higher Λ. This gives another motivation for Λ upscaling besides enhancing the sensitivity and reducing the ARW as shown in section 2.1.2. In the final designs, it was found that $t_{ox} = 1.5\ \mu m$ was enough to reach a negligible confinement optical loss [31].

Table 2.1: Summary of K_t^2 values for various SiO_2 thicknesses t_{ox} (row) and SAW wavelengths Λ (column).

	0	**1µm**	**1.5 µm**	**2µm**
30 μm	2.044%	0.3658%	0.216%	0.1492%
150 μm	2.044%	0.684%	0.4743%	0.3441%
100 μm	2.044%	1.125%	0.9068%	0.7476%

2.3.2. Interdigitated Transducer (IDT)

Interdigitated transducers (IDTs) were introduced for the first time by White and Volmer in the 1965 [32]. These structures consist of a sequence of vertical metallic electrodes (or fingers) connected to two bus bars. When an AC voltage is applied to the IDTs, the piezoelectric material underneath the IDTs expands and contracts periodically generating a mechanical wave. It is a reciprocal device that can also convert a mechanical wave in a piezoelectric substrate to a voltage. According to [33], an IDT can be used to excite different modes and harmonics. In this research, we will focus only on the 1st order mode of Rayleigh SAWs. The basic structure of an IDT is shown in Fig. 2.10.a. Other IDT structures such as that in Fig. 2.10.b and Figure Fig. 2.10.c were developed to minimize non idealities related to internal reflection and direction of propagation. From the figure

shown, the disadvantage of split IDT and single phase unidirectional IDT (SPUDT) is that they required higher resolution lithography process compared to single tape IDT.

In a SAWG, IDT directionality did not have any advantage due to the design symmetry so was not considered. The single IDT tap was used in the early versions of the SAWG when the electrodes where realized using thin Al films ($\leq 1\%\ \Lambda$). The IDT design was changed later to split IDTs for thick W electrodes to minimize the internal reflection in the IDT and avoid spurious mode generation [34].

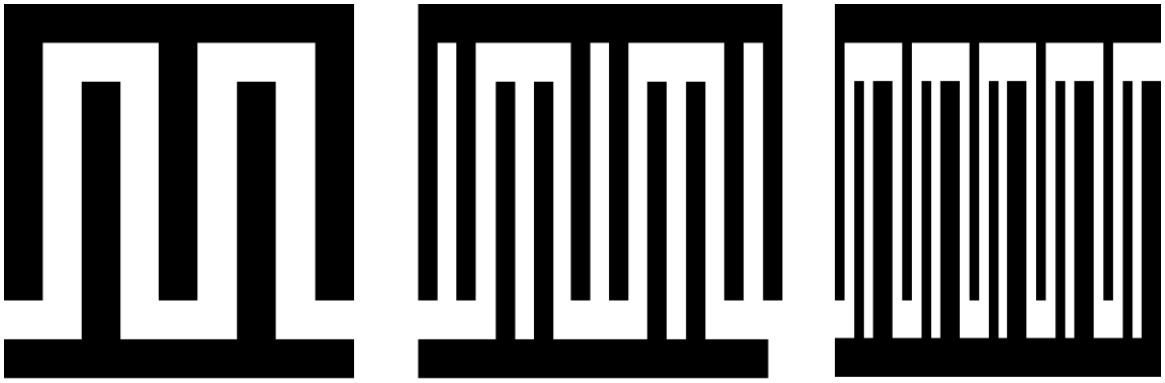

Figure 2.10: Different types of IDTs where a) is single tap IDT, b) is Split IDT while c) is single-phase unidirectional IDT (SPUIDT).

An equivalent electrical circuit of the IDT is crucial to realize electrical matching. This is the first step towards modeling of a SAW resonator. A simple approach to build this equivalent circuit (Fig. 2.11.a) is the so-called Delta function model. In this model each electrode can be treated as an independent source of surface waves and the response of the IDT can be approximated with a sinc (Fig. 2.11.b). Taking advantage of this model the equivalent admittance of the IDT is given by (Eq. 2.7).

$$Y_{IDT} = G_{IDT} + jB_{IDT} + j\omega C_T \tag{2.7a}$$

$$G_{IDT} = G_{IDTo}\left|\frac{sinX}{X}\right|^2, B_{IDT} = B_{IDTo}\frac{\sin(2X) - 2X}{X^2} \tag{2.7b}$$

$$C_T = c\frac{N_{IDT}}{2}C_s L_A, n_{single-tap} = 1, n_{split} = 1.4 \tag{2.7c}$$

Where C_T is the total capacitance with the substrate and G_{IDT} and B_{IDT} are respectively the conductance and the susceptance of the isolated IDT while X is function in frequency, $X = \pi \frac{N_{IDT}}{2} \frac{(\omega_o - \omega)}{\omega_o}$. At the resonance frequency, $B_{\_IDT} = 0$ and G_{IDT} is max given by Eq. 2.7.

$$G_{IDT}(\omega_o) = G_{IDTo} = \frac{2N_{IDT}^2 K_t^2 \nu_o C_s L_A}{\lambda} \tag{2.8}$$

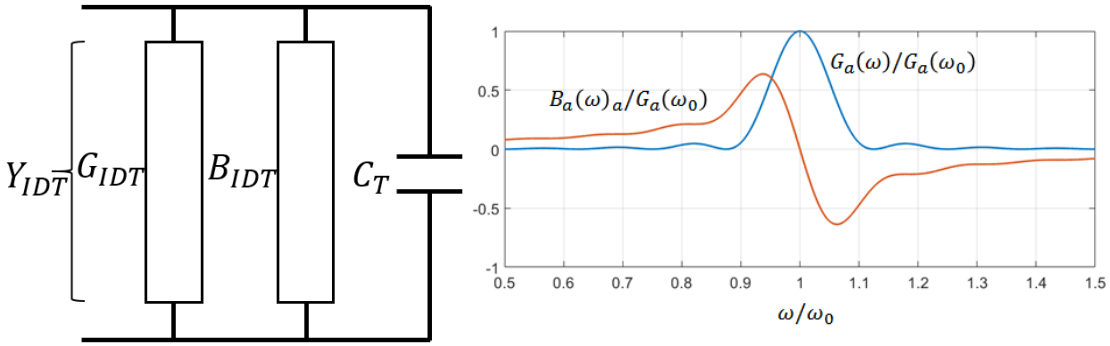

Figure 2.11: Modeling of the IDT frequency response where a) is the equivalent circuit model while b) is a plot of the model components vs frequency.

Considering SAWG operation, it is a single frequency narrow band device where we are interested in the response around the peak amplitude which leads to a simplified admittance expression, $Y_{IDT} = G_{IDTo} // \frac{1}{\omega_o c_T}$. For maximum power transfer, N_{IDT} and L_A are designed to achieve power matching condition and minimized radiation loss as discussed in sections 2.3.4 and 2.3.6.

2.3.3. Reflector Grating

Grating reflectors are fundamental elements of SAW resonators. These structures consist of an array of elements used to perturb the acoustic properties of the piezoelectric substrates resulting in impedance mismatch which is used to reflect a significant portion of any incoming wave. The periodicity of the arrays defines the phase difference between the reflected and transmitted waves and it is set to have all reflected waves constructively interfere. This results in total wave reflection if enough number of reflectors are used. The higher the acoustic mismatch the higher the reflected portion of the wave. The ratio of the

magnitude of the reflected to the incident wave is known as reflectivity (r). There are two major physical mechanisms by which reflectivity is attained: piezoelectric (or electrical) and mechanical [35]. There are two commonly used types of gratings, groove array (GA) and metal array (MA) with different electrical boundary conditions such as short circuit (SC), open circuit (OC) and Interdigitated (IDT) as shown in Fig. 2.12.

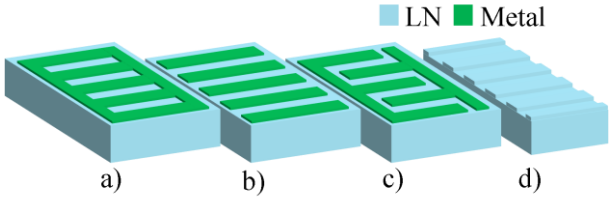

Figure 2.12: 3D sketch for MA and GA grating where a) MA SC, b) MA OC, c) MA IDT, d) GA.

The reflectivity per finger, *r*, of acoustic gratings is governed by:

$$r = j\left[r_E + r_M\right]\sin\left(\frac{\eta\pi f}{f_o}\right) \tag{2.9}$$

Where r_E and r_M are the electrical and mechanical reflectivity, η is the metallization ratio, f is the frequency range over which the grating operates, and f_o is the center frequency of the gratings. The electrical and mechanical reflection coefficients are given by:

$$r_E = P_z(\eta)\frac{K_t^2}{2}, r_M = F_z\frac{h}{\Lambda} \tag{2.10}$$

Where K_t^2 is the electromechanical coupling coefficient, P_z is the electric reflectivity coefficient at a given η ($P_z \sim -0.75$ at $\eta = 0.5$) [36], h is the thickness of the grating or depth of the groove, λ is the wavelength of the SAW, while F_z is the mechanical reflectivity coefficient given by:

$$F_z = \frac{-\pi K_t^2}{2C_s}\left[c_x^2\left(\alpha_x + \rho_r v_o^2\right) + c_y^2\rho_r v_o^2 + c_z^2\left(\alpha_z + \rho_r v_o^2\right)\right] \tag{2.11}$$

where c_x, c_y and c_z are the piezoelectric surface parameters, ρ_r, α_x and α_z are the mass density and mechanical constants of the material from which the grating is made. The total grating reflectivity (Γ) is given by Eq. 2.11 where N_{ref} is the total number of grating fingers.

$$\Gamma = \tanh\left(N_{ref}|r|\right) \tag{2.12}$$

To attain higher reflectivity, one solution is to increase the number of grating reflectors at the expense of the form factor of the whole reflector array. The second solution is to have a higher r. There is not much to do to increase r_E since it is limited by the K_t^2 of the piezolectric substate. On the contrary, several techniques could be employed to increase r_M by simply increasing h or F_z by using high ρ, c_x and c_z metals. In this section, we study and implement various techniques to increase r_M of reflector gratings oriented at ±45° on Y-cut LN. By exploiting MEMS processing techniques, we significantly increase the reflectivity of the reflector gratings.

The total grating reflectivity (Γ) has a direct impact on the acoustic radiation loss and the overall performance of a SAW resonator as discussed in the next section.

As discussed in section 2.3.1, the surface parameters of Y-cut LN ±45° were extracted using COMSOL 3D simulation of a unit cell with periodic boundary conditions in which SAWs were induced. Table 2.2 summarizes our findings. Unlike the real and imaginary coefficients of YZ LN, the coefficients of ±45° oriented devices were found to be complex, which complicates dealing with the phase of the reflected wave.

Table 2.2: Surface parameters for YZ and Y45 oriented SAWs.

Cut/Direction	c_x (Å/V)	c_y (Å/V)	c_z (Å/V)	C_s (pF/cm)	K_t^2 (%)	v_o (m/s)
LN YZ	0	1.8j	-1.2	4.6	4.6	3488
LN Y45	-0.16-0.85j	-2.09-2.19j	-1.78+1.29i	4.59	2.04	3576

We evaluated the use of different metal layers for the definition of the reflectors and the pillars. As shown in Table 2.3, we evaluated a set of metallic electrodes based on the values

of their mass density (desired to be large for the Coriolis mass m_p of the SAWG too), intrinsic losses due to thermoelastic damping (TED), and F_z at ±45°.

We have also considered the ease of fabrication of relatively thick films of these metals. Based on these considerations, W was selected for the making of the reflectors, IDT and pillars in this work.

Table 2.3: Summary of physical parameters of metals considered for use in the fabrication of SAW devices

	ρ (km/cm^3)	**v_o (m/sec)**	**α TED (dB/cm)** [37]	**$\|F_z\|$ Y45**	**Processing thick films**
Al	2.695	2.80	20.5	0.32	Easy
W	19.25	2.65	2	1.38	Easy
Au	19	1.12	167	1.06	Easy
Cu	8.96	3.52	42	0.25	Easy
Pt	21.45	1.57	< 0.5	0.75	Hard
Ag	19.49	1.48	250	1.07	Easy
Ti	4.506	3.2	0.5	0.50	Easy

The acoustic reflectivity of the gratings was characterized using a SAW delay-line (DL). The grating reflectors are inserted in between the two set of IDTs used to drive and sense the DL. The presence of the grating reflector in between the transmit and receive IDTs reflects a portion of the propagating wave and attenuates the intensity of the wave at the receive IDT. By comparing the received intensity with and without the reflector, we can extract Γ, use (Eq. 2.12) to evaluate r for a given N_{ref} and finally use (Eq. 2.10-2.11) to get the value of F_z.

The proposed characterization approach was simulated in COMSOL finite element methods (FEM) as shown in Fig. 2.13.

A test bench was created to investigate the different types of gratings under study. SAW DLs were simulated in COMSOL 2D for different reflector types with ten different variations in reflector structure (MA and/or GA) and electrical boundary conditions such

as short circuit (SC), open circuit (OC) and interdigitated (IDT), on the metal reflectors as shown in Fig. 2.14.

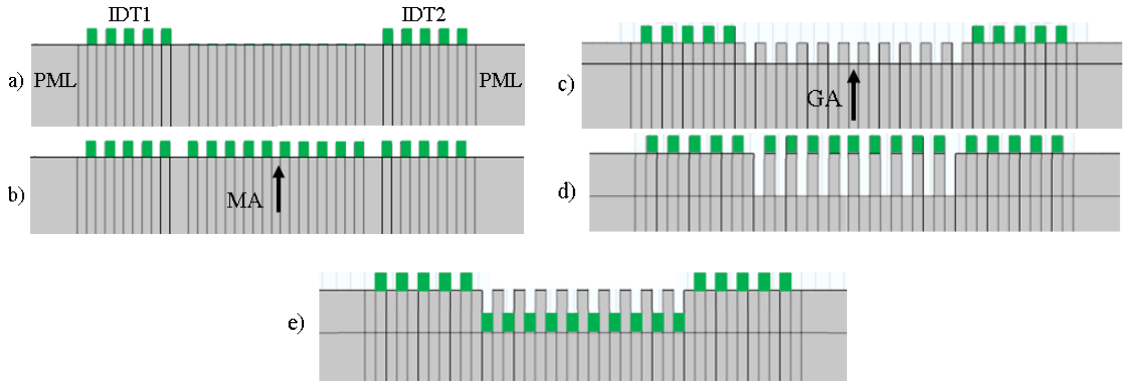

Figure 2.13: COMSOL 2D DL test bench for reflectors where a) is a DL without reflectors, b) with MA, c) with GA, d) with MA and GA interleaved (MA+GA1) and e) with MA and GA overlapped (MA+GA2). The electrical boundary conditions were applied on the grating electrodes virtually using the potential function in COMSOL.

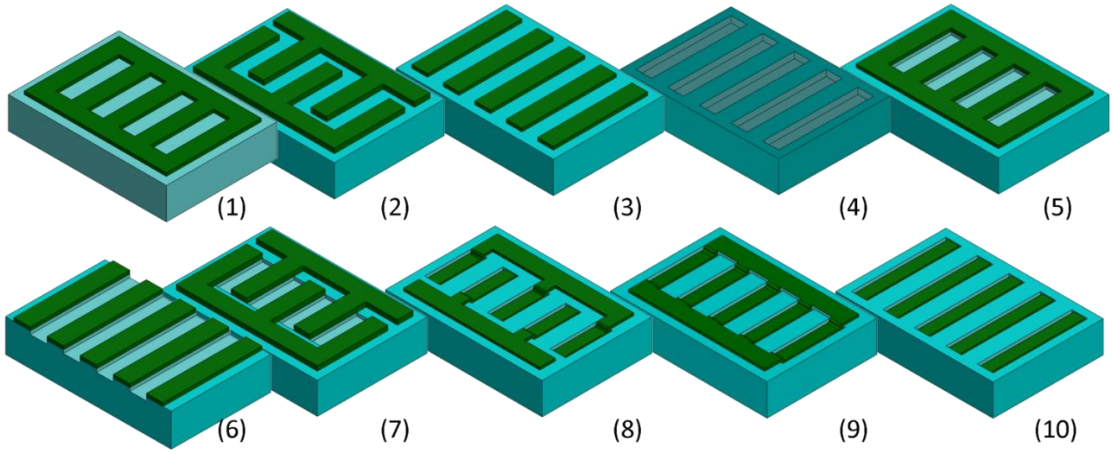

Figure 2.14: Ten variants of reflector gratings where 1) MA SC (Short circuit), 2) MA IDT (Interdigitated), 3) MA OC (Open Circuit), 4) GA, 5) MA+GA1 SC (Interleaved), 6) MA+GA1 OC (Interleaved), 7) MA+GA1 IDT (Interleaved), 8) MA+GA2 IDT (overlapped), 9) MA+GA2 SC (overlapped) and 10) MA+GA2 OC (overlapped).

The Z-cut LN stiffness, permittivity and piezoelectricity matrices [C], [ε] and [d] where rotated using the method in [38] explained in Appendix A to get the Y-cut LN ±45° matrices. The thickness and depth of MA and GA were limited to ≤ 2% of Λ to avoid bulk scattering according to [39]. The simulated values are $h = 0.01\lambda$, $\Lambda = 30$ μm and N = 120.

Given these parameters, the MA + GA interleaved (MA + GA1) OC showed the highest reflection coefficient.

Using the FEM simulations as a guide, DLs and resonators with various reflector grating types were designed as summarized in Table 2.4.

Table 2.4: SAW resonator and DL design parameters

Devices	**Resonator**					**DL**	
Parameters	N_{ref}	λ (μm)	L_c (λ)	L_A (λ)	N_{IDT}	N_{ref}	N_{IDT}
value	400	30	40	40	33	100	61

The characterization of the fabricated devices was performed using VNA Agilent N5230A where the devices were probed using 2 GGB GSG-150μm RF probes. The measured data were analyzed to extract |*r*| for the different reflector types and compared to simulations as shown in Fig. 2.15. The extracted |*r*| showed a close agreement to the simulation results for all configurations.

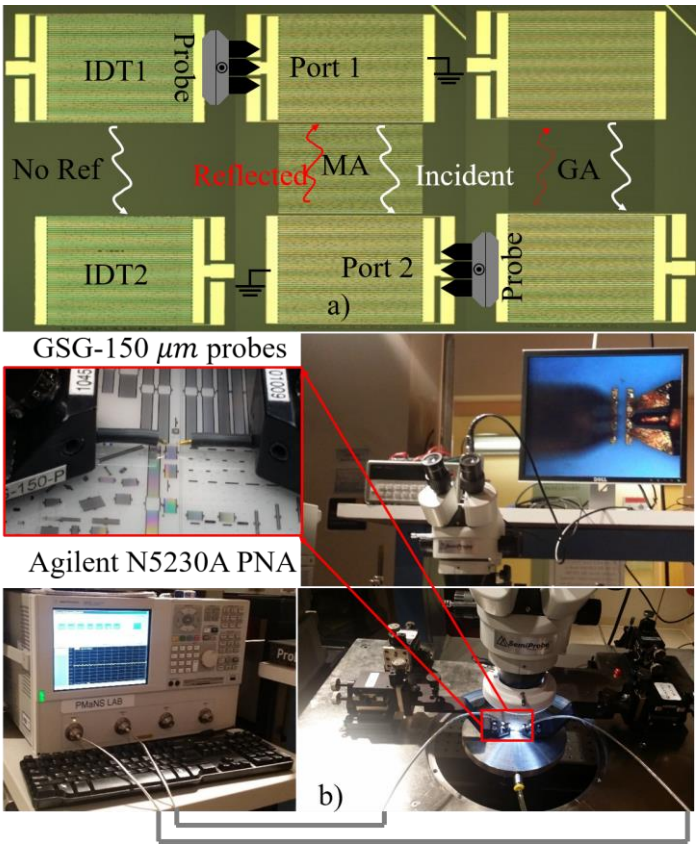

Figure 2.15: Testing of DLs where a) shows microscope images of fabricated DLs with different kinds of reflector arrays as indicated while b) shows the probing setup.

Based on this analysis we can conclude that the maximum reflectivity is achieved for MA+GA1 OC, $|r|_{\max} = 2.89\%$ at h = 581 nm as in Fig 2.16.

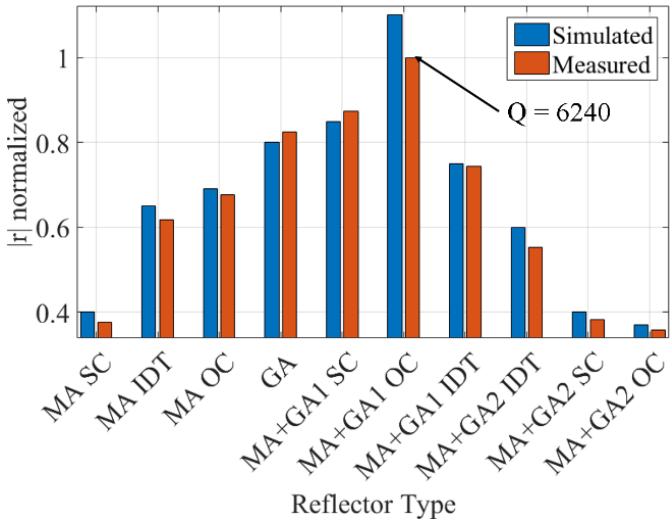

Figure 2.16: Comparison between simulation and measured |r| of different types of reflectors build on Y-cut LN along 45°.

2.3.4. Pillars and quadrature

Quadrature is one of the parasitic effects that highly affects the performance of any gyroscope. It does not only saturates the readout circuit and requires a wide output dynamic range, it also couples the drive loop noise to the output sense leading to higher ARW and bias instability. Fig. 2.17 shows a structure used to quantify quadrature signal coupling orthogonally from drive to sense. It is clear that the coupling is high with pillars since they scatter part of the wave orthogonally.

.Impedance mismatch is the reason behind both reflection and scattering for a pillar. A different method to realize the pillars is introduced in section 3.1.2. The pillars are realized from the LN by groove etching the substrate. Built from the same material, impedance mismatch is only due to the groove which has small dimension and low reflectivity according to Eq. 2.9. Primary testing results of SAW resonators with grooved pillars showed a reduction showed reduction in quadrature signal by ~ 15 dB compared to

conventional metal pillars. The only drawback is the reduction in the mass of the pillars by the ratio of densities ρ_{LN}/ρ_W which leads to reduction in Coriolis signal and sensitivity.

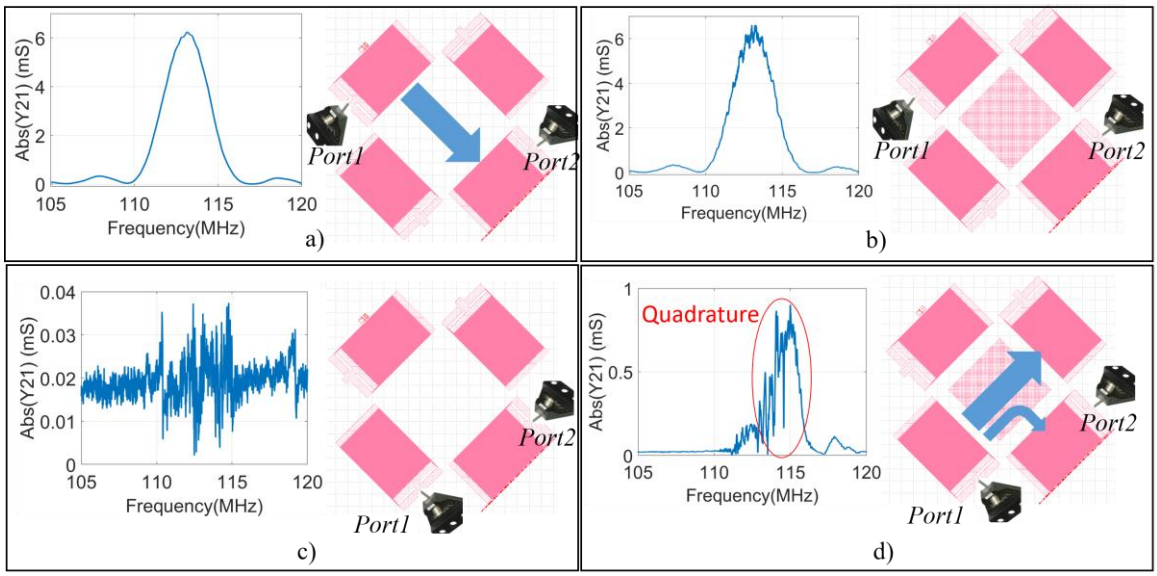

Figure 2.17: Wave scattering and quadrature signal due to pillars where a) shows the transmission without any ripples, b) shows a negligible orthogonal coupling limited by VNA noise level, c) shows transmission with some ripples due to back scattering while d) shows a considerable orthogonal coupling due to wave scattering by pillars.

2.3.5. 2-port SAW Resonator

SAW resonators have been widely used in various sensing and filtering applications [40]. The principle of operation and level of complexity widely varies according to the required specifications. All SAW resonators somehow use the same resonance concept based on Fabry–Pérot [41]. The first condition is that that oscillation builds up if the excess phase of a round trip in a loop system is $\phi = 2n\pi$ where n is an integer $n = 0, 1$ .... The second condition states that in a sustained oscillatory system, the energy lost by the system is equally compensated from an external energy source keeping oscillation balanced. Considering the two previous conditions, properly spaced reflector gratings can achieve the phase condition while an IDT between the reflectors can generate acoustic waves and be supplied with a power equal to the energy loss in the resonant system. The previous definition represents the basic 1-port SAW resonator first introduced in [42]. To facilitate

SAWG drive and control the use of two separate IDTs is preferred. In addition, we are not only interested in exciting a resonance but also in coupling the mechanical vibrations to pillars placed on the surface of the acoustic cavity. Due to the previous consideration, a cavity filled with pillars in a checkerboard configuration was built between the two IDTs forming a 2-port SAW resonator as shown in Fig. 2.18.

Several techniques such as Mason equivalent model [43], perturbation model [], P-matrix model and coupling of modes (COM) model [44] have been used to study the response of SAW devices. All the previous methods have the ability to capture acoustic response in the frequency spectrum. The main difference between them are the complexity, computation time and accuracy. The perturbation model is a physics-based model that describes acoustic responses in 1D or 2D using closed form expressions.

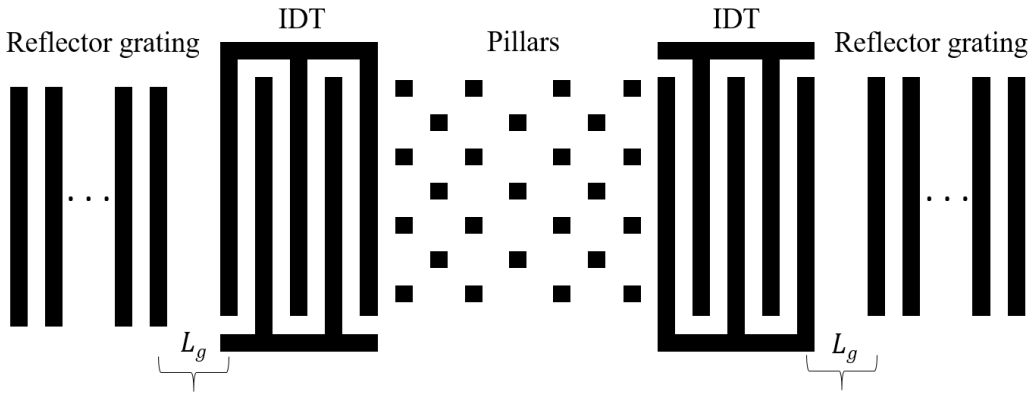

Figure 2.18: Cartoon of 2-port resonator used in a SAWG showing its various constitutive components.

Due to the simplifying assumptions made in the derivations, it has the least accuracy among the previously mentioned methods in capturing the wide spectrum behavior and non-idealities. On the other side, it provides closed form equations with acceptable accuracy around resonance and almost negligible computational requirements. Since the SAWG is operated in a frequency matched mode around resonance, we choose perturbation modeling of the IDT and grating reflectors acoustic components. However, the modeling of the acoustic behavior of the pillars represents a complex 3D problem that is hardly treated using

closed form expressions. Instead, the pillars where considered as non-resonating mass elements neglecting its effect on the resonator.

Since we are interested in only the frequency response around resonance, the BVD model [45] was more than enough to model the 2-port SAW resonator as shown in Fig. 2.19.

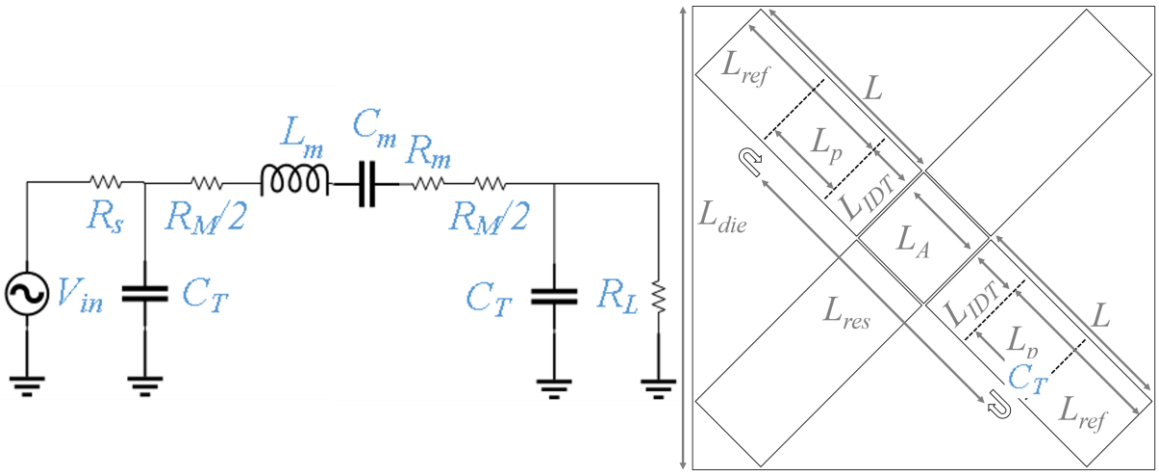

Figure 2.19: BVD model and floor plan of the 2-port resonator used in a SAWG.

The values of the equivalent parameters are given in (Eq. 2.13 to 2.16). Those equations were used to design the SAWG resonators within the constraints imposed by the required form factor of the AOG and the placement of the photonic devices.

$$f_o = \frac{1}{2\pi}\frac{1}{\sqrt{L_m C_m}}, Q_{ref} = \frac{\pi}{1-\Gamma}\frac{L_A + 2L_{IDT} + 2L_p}{\Lambda} \tag{2.13}$$

$$L_p = \frac{\lambda}{4|r|}, N_p = 2\left(\frac{L_A}{\Lambda}\right)^2, \left(N_{IDT} + N_{ref}\right) = \frac{2L}{\Lambda}, L_g = \left(\frac{3}{8} or \frac{5}{8} + \frac{n}{2}\right)\Lambda \tag{2.14}$$

$$L_m = \frac{1}{4G_{IDT}f_o}\frac{2L}{\Lambda}, C_m = \frac{1}{4\pi^2 f_o^2 L_m}, R_m = \frac{1}{G_{IDT}N_{IDT}^2}\frac{1-\Gamma_{eff}}{1+\Gamma_{eff}} \tag{2.15}$$

$$R_M = \frac{4}{3}\frac{\rho_M L_A}{\eta p t_M N_{IDT}}, W_{p-max} = \frac{\Lambda}{4} \tag{2.16}$$

Where Q_{ref} is quality factor due to reflectivity, $L_m, C_m \; and \; R_m$ are the motional inductance, capacitance and resistance of the 2-port SAW resonator. L_p is the effective penetration depth of SAW in the acoustic grating, $N_p, N_{IDT} \; and \; N_{ref}$ are the number of

pillars, IDT and reflector fingers. L_A is the aperture length, L is half length of the SAW resonator, $L_g$is the separation between the center of the last IDT finger to the center of the first reflector finger, n is an integer where $n = 0,1, ..., f_o$ is the SAW resonance frequency, Γ_{eff} is the effective reflector grating reflectivity, ρ_M and t_M are the mass density and thickness of the metal film, η is the metallization ratio, $p = \frac{\Lambda}{2}$ is the pitch. Using this model, the resonator is designed for high quality factor by setting N_{ref} to achieve the target reflectivity quality factor, maximum power coupling by setting N_{IDT} to achieve 50 ohm matching condition. Those design considerations have direct impact on the sensitivity guided as discussed in the parametric study in section 2.1.2.

2.3.6. Quality Factor

The quality factor is one of the important parameters that has a direct impact on the performance of the SAWG. The quality factor affects the sensitivity of the SAWG and the ARW as shown previously in section 2.1.2. In addition, it plays an important role in the stability of the drive loop, phase noise and the stability of the zero rate output (ZRO) as explained in section 5.2. From the definition of the quality factor, it is proportional to the ratio of energy stored in the system to the energy dissipated per cycle. Since the goal is to maximize the quality factor, the maximization of energy was performed by the maximization of the mechanical resonant volume of the system. Unfortunately, the previous is limited by the physical dimensions of the system. On the other hand, we can minimize the energy dissipated per cycle by reducing the loss mechanisms in the SAWG. In this section we study many loss mechanisms, explain the techniques to mitigate them and report the most important experimental results we attained. The quality factor is described by (Eq. 2.17 to 2.18), which include the most dominant loss mechanisms in SAW.

$$Q_{total} = \left(\frac{1}{Q_{ref}} + \frac{1}{Q_{propagation}}\right)^{-1} \quad (2.17)$$

$$Q_{propagation} = \left(\frac{1}{Q_{BS}} + \frac{1}{Q_{diff}} + \frac{1}{Q_{bulk}} + \frac{1}{Q_R} + \frac{1}{Q_{loading}} + \frac{1}{Q_{TED}} + \frac{1}{Q_{phonon}}\right)^{-1} \quad (2.18)$$

where each Q with subscript represents the Q due to a different loss mechanism: Q_{ref} is due to reflector loss, Q_{BS} is due to beam steering, Q_{diff} is due to wave diffraction loss, Q_{bulk} is due to wave scaterring into the bulk, $Q_{loading}$ is due to viscous air loading, Q_R is due to metal film finite resistance, Q_{TED} is due to the TED in the metal film while Q_{phonon} is due to phonon-phonon viscous damping. The loss mechanisms are ordered in what we expect to be most to least dominant.

Reflector loss is governed by the reflectivity of the reflector gratings (represented in Fig. 2.20). The loss was minimized using high number of gratings and enhancing the reflectivity per finger as explained in section 2.3.4.

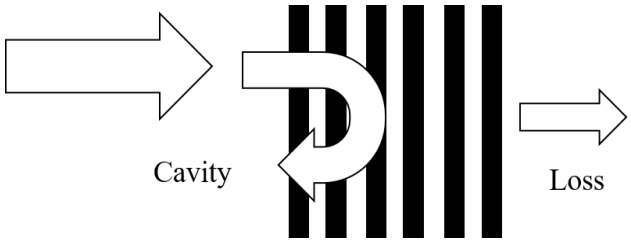

Figure 2.20: Cartoon representation of reflector loss.

Despite the noteworthy progress made by improving the reflectivity of the acoustic grating and minimization of reflector loss, the acoustic loss is now limited by propagation loss. We extracted the propagation loss from DL measurements similar to the ones shown in section 2.3.4 but with different delays. The propagation loss, α, is approximately ~ 1.37 dB/cm as shown in Fig. 2.21. It was found from theoretical analysis that beam steering and diffraction phenomena start to dominate.

Diffraction takes place when the SAW resonator acts as an acoustic lens. In this case, the SAW diverges or converges and generates destructively interference. To minimize this type

of loss, methods similar to those employed in optics are considered. One of those methods is increasing L_A relative to Λ. The study done in [46] provides an estimate of the quality factor limitation due to diffraction, which is given in (Eq. 2.19).

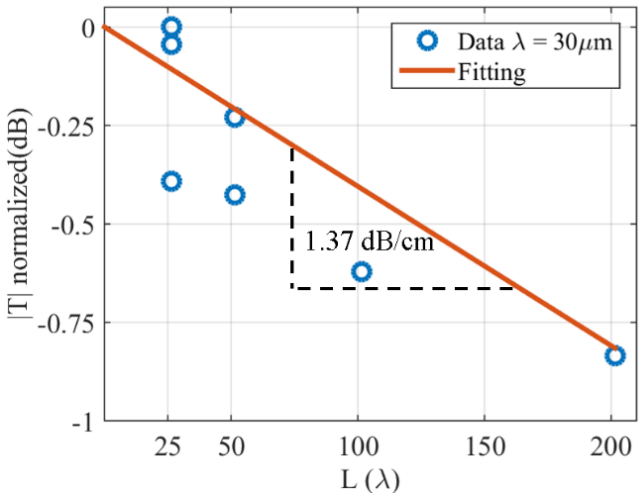

Figure 2.21: DL transmission for different delays used to evaluate propagations loss in Y-cut LN along 45°.

Considering this formula, the diffraction loss was minimized by designing wide aperture resonators. Aperture width of $L_A = 80\lambda$ was used resulting in $Q_{diff} = 26{,}800$ well beyond the Q recorded for most SAWG resonators.

$$Q_{diff} = \pi \frac{5}{|1+\gamma|}\left(\frac{L_A}{\Lambda}\right)^2, \gamma_{Y45^\circ} = 0.19 \tag{2.19}$$

The phenomenon of beam steering takes place when the direction of the group velocity, v_g , also known as the direction of the Poynting vector , P, is different from the direction of the phase velocity as shown in Fig. 2.22.a. This takes place in piezoelectric materials in certain cuts and directions due to the anisotropy of the material. From [47], the steering angle is defined as:

$$\phi_{BS} = \frac{1}{v}\frac{\partial v}{\partial \theta} \tag{2.20}$$

Where ϕ_{BS} is the beam steering angle while θ and v are the angle and phase velocity along a certain direction relative to Z-direction. Four methods were used to extract the value of

the beam steering angle for the particular device configuration used in a SAWG. In the theoretical method, phase velocity vs, θ data was extracted from COMSOL simulations for Y-cut as shown in Fig. 2.22.b where (Eq. 2.20) was used to calculate the steering angle for Y-cut ±45^{o} direction.

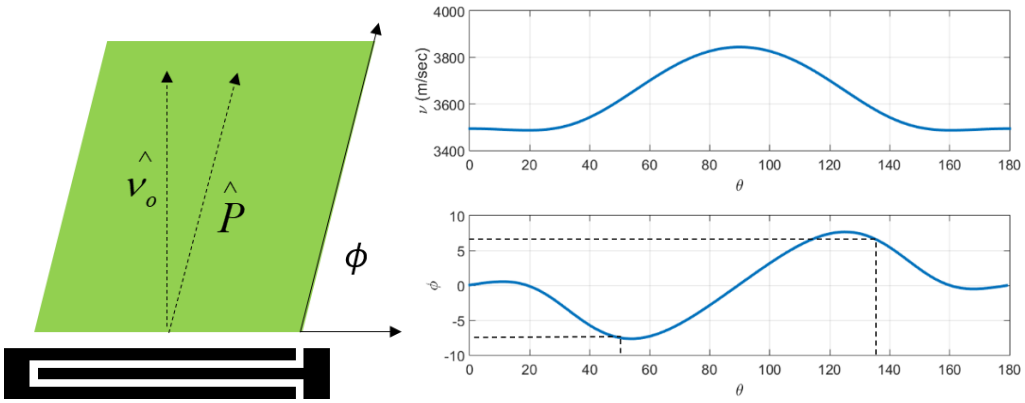

Figure 2.22: Beam steering study where a) is a cartoon showing beam steering and wave vectors while b) is a graph of v vs θ used to calculate the beam steering angle.

A full 3D FEM model was also built in COMOSL multiphysics to describe the steering phenomenon on a propagating acoustic wave (Fig. 2.23). As shown in Fig. 2.23.a, an IDT with a direction of propagation along $\pm 45°$ direction is surrounded by perfectly matched layers (PMLs) to avoid any back reflections and resonances where the wave propagation was observed on one side. Fig. 2.23.b shows the steering behavior of the wave from which the beam steering angle was extracted.

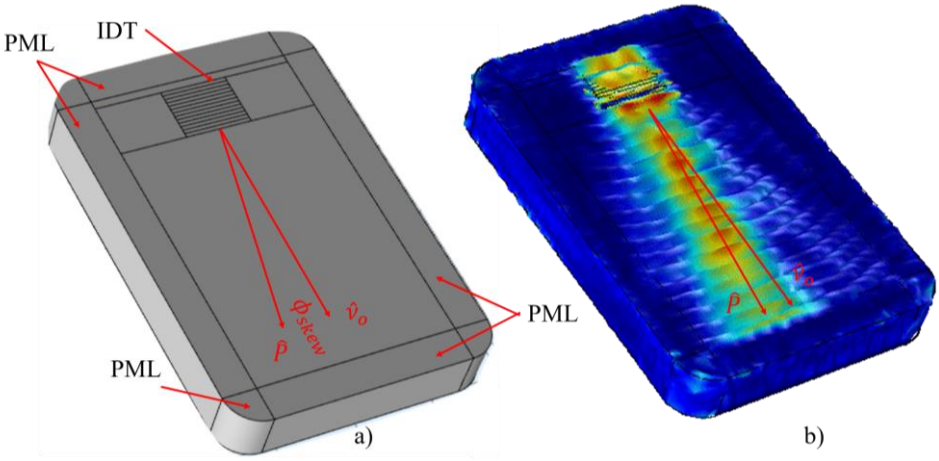

Figure 2.23: 3D FEM COMSOL simulation showing both beam steering in Y-cut LN ±45o where a) explains the setup's components while b) shows the simulation.

Digital holographic measurements (DHM) with Lyncée Tec instrument were also used to experimentally extract the steering angle. A signal was applied to an IDT using the output signal from Lyncée Tec stroboscope unit to excite the SAW wave. The wave is then captured using a synchronized camera where the amplitude of the SAW wave is plotted as shown in Fig. 2.24. The beam steering angle was extracted by using simple geometrical considerations that would allow us to derive the directions of P and vo as shown in Fig. 2.25. Based on these considerations, a set of equations (Eq. 2.21) was derived to extract steering and divergence angle.

$$L_s = L_A \frac{\sin\theta_2}{\sin(\theta_1 - \theta_2)}, L_L = L_A \frac{\sin\theta_1}{\sin(\theta_1 - \theta_2)} \tag{2.21.a}$$

$$L_m = \sqrt{L_s^2 + L_A^2/4 + L_s L_A cos\theta_1} \tag{2.21.b}$$

$$\phi_{BS} = 180 - \cos^{-1}\left(-\frac{L_s^2 - L_A^2/4 - L_m^2}{L_A L_m}\right) \tag{2.21.c}$$

$$\theta_{div} = 90 - \tan^{-1}\left(\frac{2L_m \cos\phi_{skew}}{L_A}\right) \tag{2.21.d}$$

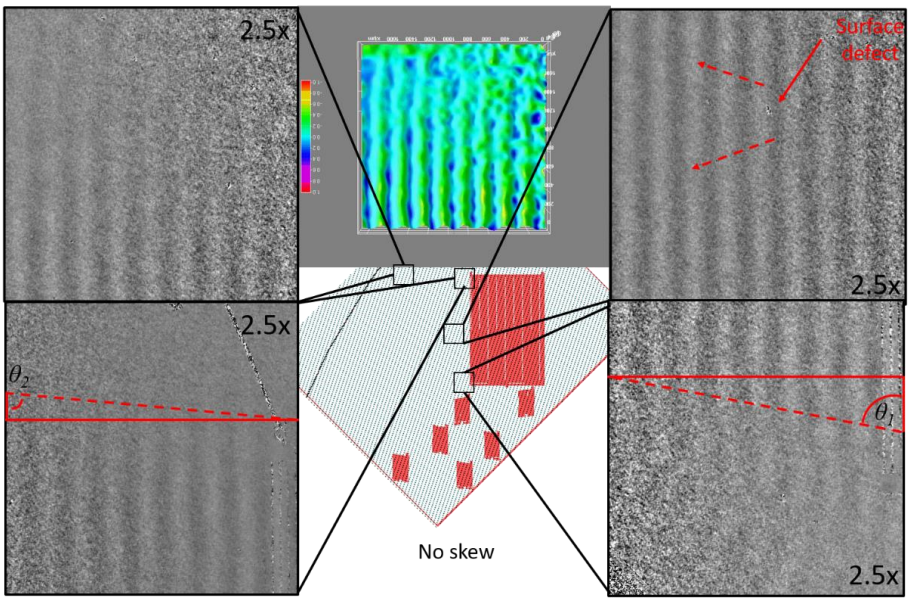

Figure 2.24: DHM measurements of SAW IDT to capture beam steering and divergence.

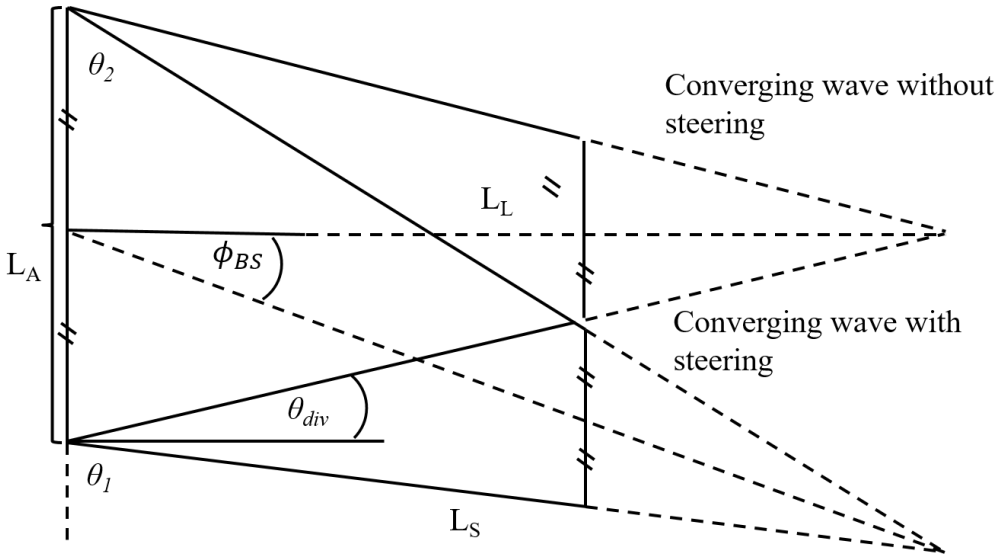

Figure 2.25: Geometrical representation of wave steering and divergence used to derive steering and divergence relation.

After verifying beam steering using three different methods, SAW resonators of various skew angles where fabricated as shown in Fig. 2.26. The basic concept of skew was introduced in [48]. The main purpose of the skew design is to shape the cavity and the mirrors in such way that the acoustic wave can be trapped in the cavity. The electrodes of both reflectors and IDT get displaced with a displacement $d_i = x_i sin\phi_{BS}$ where $x_i$is the location of the i^{th} electrode.

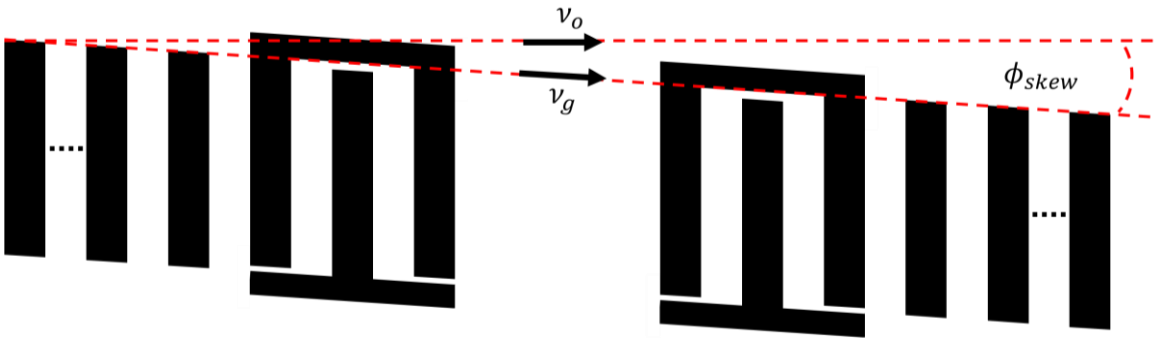

Figure 2.26: schematic showing the skew angle corrected for beam steering implemented in a two port SAW resonator.

In those designs, ϕ_{skew} was swept between $\pm\phi_o$ with a step size of $\Delta\phi = \phi_o/2$ where ϕ_o is the theoretically calculated value of ϕ_{BS}. The experimental results of Fig. 2.27 and Fig. 2.28, show that as the ϕ_{skew} gets closer to ϕ_{BS}, the spurious responses caused by

multipaths in the cavity due to wave skew decrease and become totally suppressed. The skew angle was verified along both -45° and +45° directions by simply processing and testing two wafers one rotated with respect to the other by 90°. In addition, the measurements verified that the quality factor get enhanced by correcting for the beam steering as shown in Fig. 2.27.c. The resonators showing the highest quality factor are those designed with $\phi_{skew} = \phi_{BS}$. However, the quality factor of these designs did not exceed ~ 3000.

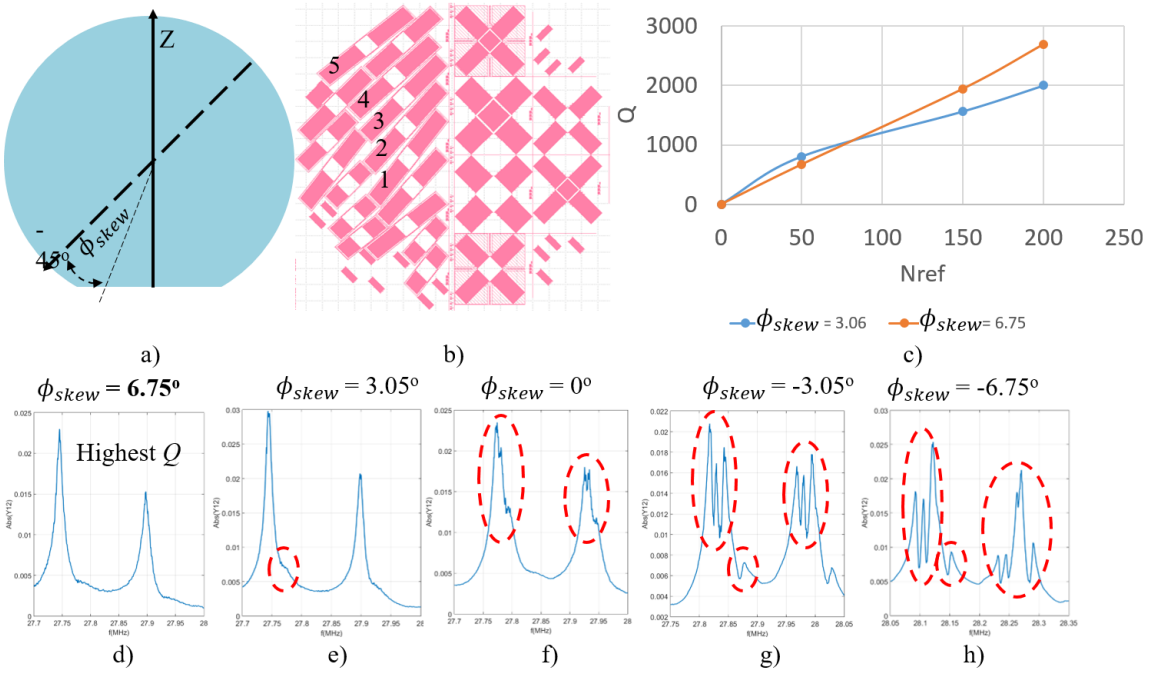

Figure 2.27: Study of skewed resonators to determine ϕ_{BS} and verify the ability of skewing in correcting for BS along -45° direction where a) shows the wave direction orientation on the wafer, b) is the layout of the mask used oriented to get -45° propagation, c) is the study of the quality factor vs the number of reflectors for different ϕ_{skew} while d) to f) show the frequency response of resonators for various ϕ_{skew}.

It was found that according to the study in [48], the wave is likely to be affected by bulk scattering loss. This type of loss is intrinsic to surface acoustic waves due to acoustic impedance mismatch between the metalized piezoelectric surface or groove and free surface. The impedance mismatch leads to energy conversion from Rayleigh SAW mode to primary (P) or shear transverse (SV) bulk modes [48]. The bulk scattering varies with η,

h and metal type of the electrode and ρ_r. In addition, the shape of the electrodes or the grooves significantly affects the bulk scattering.

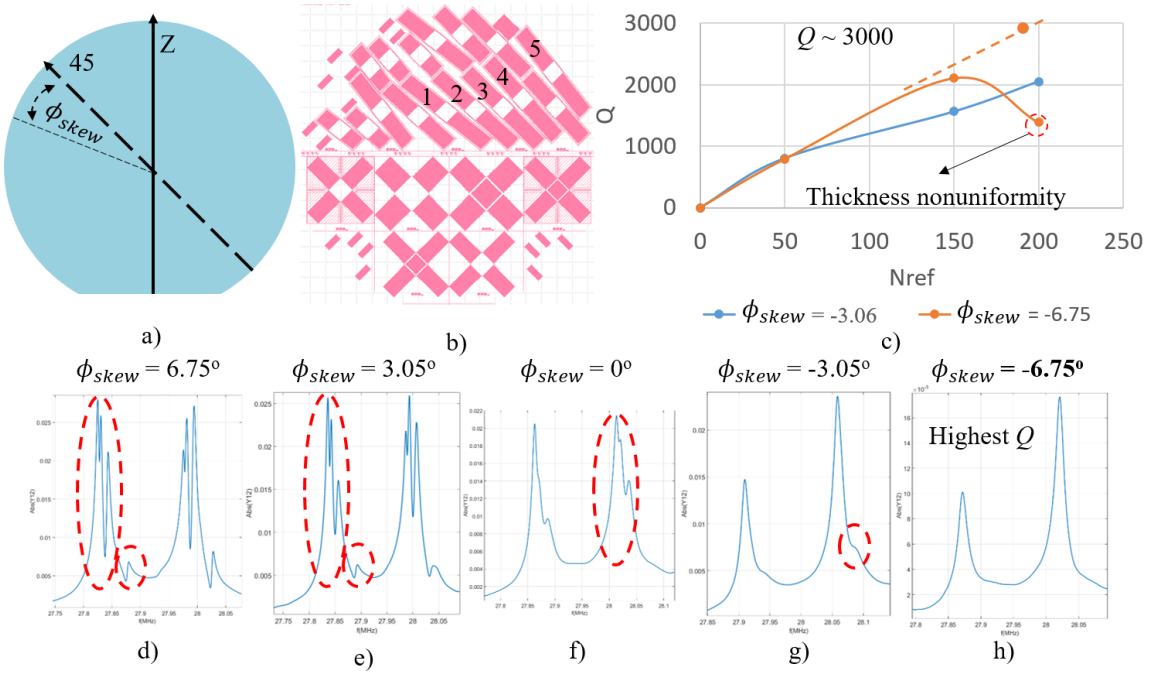

Figure 2.28: Study of skewed resonators to determine ϕ_{BS} and verify the ability of skewing in correcting for BS along +45° direction where a) shows the wave direction orientation on the wafer, b) is the layout of the mask used oriented to get +45° propagation, c) is the study of the quality factor vs the number of reflectors for different ϕ_{skew} (resonators at the edge suffered from film thickness variations and degraded quality factor) while d) to f) show the frequency response of resonators for various ϕ_{skew}.

Compared to ideal rectangular shaped, trapezoidal electrodes or grooves with titled sidewalls show less bulk scattering due to the gradual acoustic transition in acoustic impedance. Considering W metal used for electrodes in AOG, its high density and reflectivity are the source of high acoustic impedance mismatch and lead to high bulk scattering loss. Using the model derived for grooves in [49], the model was modified to estimate the bulk scattering loss for Tungsten metal electrodes. For rectangular electrodes with thickness $h = 2\%\ \lambda$ and metallization ratio $\eta = 50\%$, $Q_{bulk} \sim 3600$, which is close to the experimentally recorded Qs for the fabricated resonators.

Bulk scattering mitigation was implemented using two major techniques, tapered MA/GA height and quasi-static resonator periodicity (QARP) design. Both techniques rely on the same concept of altering the resonance condition of the SP and SV bulk modes and minimizing the coupling of energy from the main SAW mode to the bulk mode.

The MA/GA method requires the definition of tapered thicknesses across the resonators width. For example, a shield was used to modify the flow of the ions in an ion mill to get tapered grooves [50]. The QARP is based on modulating the in-plane dimensions of the resonator by changing the pitch of the IDT, $p_{IDT} = \Lambda_{IDT}/2$ in the resonator cavity while keeping the IDT-resonator gap $L_g = p = \Lambda/2$ to maintain the SAW wave periodicity [51]. Considering the challenges required to attain tapered electrode thicknesses, the QARP method was adopted instead. In this simulation, the SAW resonator with modulated p_{IDT} was simulated as shown in Fig. 2.29 using Eigen frequency analysis.

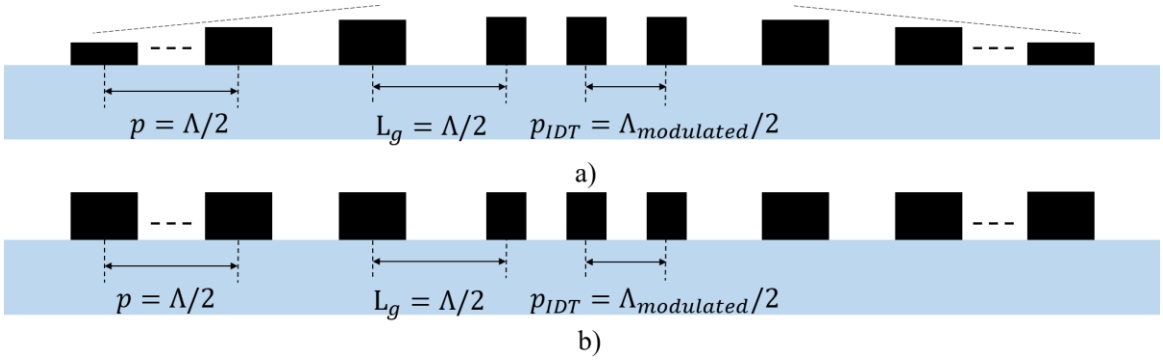

Figure 2.29: Techniques applied to reduce bulk scattering loss where a) used tapered structure while b) used QARP.

In this simulation perfectly matched layers (PML) layers were used to capture the scattering due to bulk waves. To study bulk loss only in simulation, high number of reflectors where used to minimize reflection loss while 2D simulation was used where beam steering and diffraction losses are not captured. The quality factor was extracted from the real and imaginary terms of the Eigen frequency where $Q_{bulk} = \frac{f_{o_{real}}}{f_{o_{imag}}}$. The bulk losses reduction in QARP designs was captured from simulation by sweeping the modulated pitch and

recording the quality factor. The simulated designs were used as a design guide for the fabrication of QARP SAW resonators.

The resonators where designed at $\Lambda = 150$ and modulated Λ_{IDT} from $137.5\,\mu m$ to $150\,\mu m$, step size $\Delta\Lambda = 7.5\,\mu m$, $N_{ref} = 250$, $\phi_{skew} = \phi_{BS}$ and $L_A = 80\Lambda$ making beam steering and diffraction losses negligible. The 16 resonators where fabricated on Y-cut bulk LN 4' wafer using W metal electrodes. After characterization, the extracted quality factor of the measured resonator exhibited a trend similar to that shown by COMSOL simulations (see Fig. 2.30) but the absolute value of the quality factor is lower by approximately a factor of 2. After careful investigations, it was found that the uniformity of the deposited metal highly affected the resonator measurements. The film thickness variations was extracted from profilometer measurements of the wafer as shown in Fig. 2.30.a.

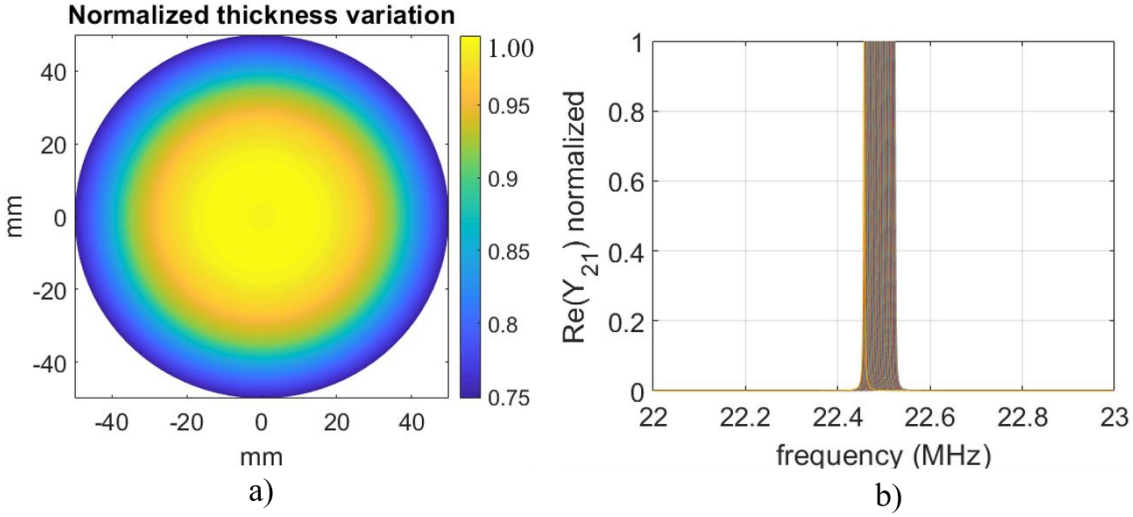

Figure 2.30: Study of the effect of metal film thickness variations across the aperture of a SAW resonator on the Q where a) is a contour plot of measured Tungsten metal film thickness on a 4' Y-cut LN wafer while b) is a graph of measured data and theoretical model of a SAW resonator frequency response showing the model's ability to capture film thickness variations effects.

Thickness variations across the resonator aperture caused variable mass loading. The phase velocity of each infinitesimal unit of the SAW resonator was varied. This lead to

broadening in the resonance peak of the SAW frequency response creating something similar to staggered frequency response. The quality factor extracted from this response using 3-dB bandwidth method $Q = \frac{f_o}{BW_{3dB}}$ is misleading and does not reflect the intrinsic device Q.

To verify this postulate, n^{th} order BVD model was simulated using MATLAB where $n = \frac{L_A}{\Lambda}$. The resonance frequency of each section of the n^{th} order BVD model was varied according to the theoretically expected mass loading.

The frequency response in Fig. 2.31 showed a great matching with the actual measurements. In addition, the model was used to estimate the film uniformity requirement to achieve the theoretically expected quality factor extracted from COMSOL simulations.

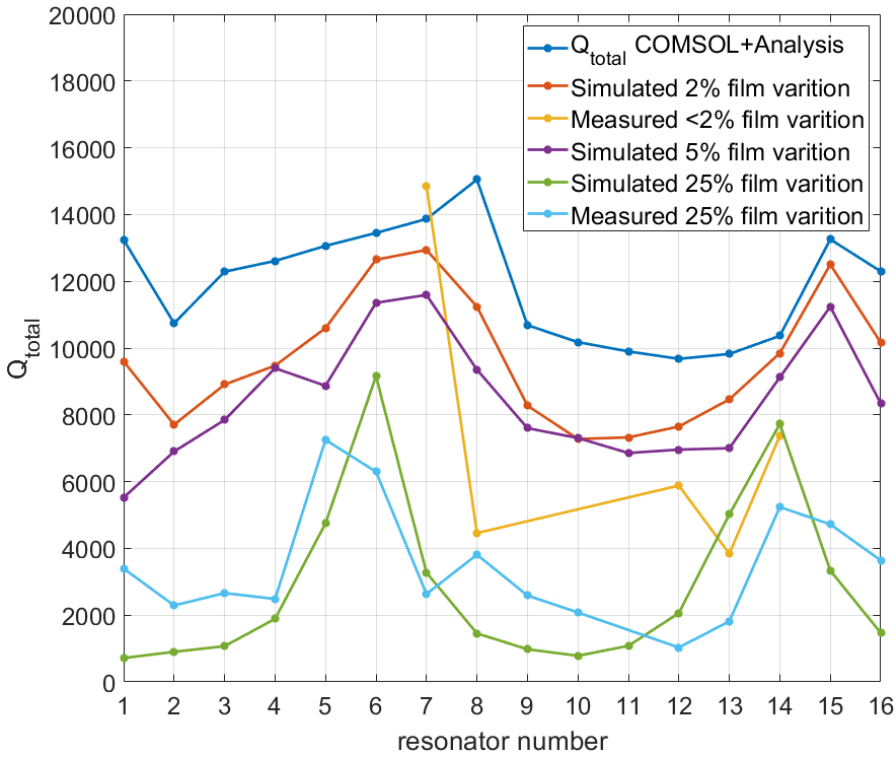

Figure 2.31: Simulation and measurements of QARP resonators showing the ability of modulated pitch to minimize bulk loss and the effect of metal uniformity on the apparent Q.

It was found that we need to enhance the film thickness uniformity by decreasing variations center to edge from 25-30% to < 5%. This required the usage of a new deposition system where the wafer is rotating on a stage relative to the W target while depositing to achieve

high uniformity. Using this tool (discussed in details in section 3.1.2), we were able to deposit films with thickness variations < 2% enabling us to measure high quality factors$Q_{total} = 14{,}000$.

Table 2.5 summarizes the types of losses and the values of the Q we characterized, simulated or deduced from measurements for different designs and fabrication tape-outs. The total Q is now limited by resistive loss due to the finite resistance of the film making the resistance of the electrode's fingers comparable to the resonator motional resistance. The resistance of the electrodes and the quality factor due to electrode resistivity are calculated using (Eq. 2.22) where Q_o is the quality factor due to all the loss mechanisms except film resistivity.

$$Q_R = \frac{Q_o}{1 + \frac{R_m}{R_M}} \tag{2.22}$$

One of the solutions considered is minimizing the resistivity of the sputtered film by controlling the sputtering parameters which is explained in detail in section 3.1.2. Increasing the film thickness reduces the resistance but it was not considered due to its effect on bulk scattering and the SAW operation so the thickness was kept at $h_o = 2\%\Lambda$. Losses due to viscous air loading and phonon scattering were also evaluated. The relations in [51] were used to estimate their values which are very far from being the dominant factors. The TED was considered in selecting the electrode metal as discussed in section 2.3.4 where the estimated quality factor $Q = \frac{\pi}{\alpha_W \Lambda}$, α_W is the TED coefficient of Tungsten. The calculated Q_{TED} is not dominant especially at low resonance frequencies and high Λ. This work shows how increase in Q were attained by increasing grating reflectivity, introducing skew designs and QARP design.

Table 2.5: The progress achieved in enhancing the Q of SAW resonators along Y-cut LN $\pm 45^o$ directions in 4 consecutive resonator designs and fabrication tape-outs.

	Tape-out 1	**Tape-out 2**	**Tape-out 3**	**Tape-out 4**
$\Lambda\ (\mu m)$	30	30	120	150
$L_A\ (\mu m)$	40	80	40	80
Metal	Al	W	W	W
$t_M(\mu m)$	0.45	0.6	2.5	3.2
ϕ_{skew}	NA	NA	ϕ_{BS}	ϕ_{BS}
Q_{ref}	5,000	10,000	10,000	375,000
Q_{Diff}	21,250	85,000	21,250	85,000
Q_{BS}	1550	2710	718,000	718,000
Q_{bulk}	-	-	-	15,000
Q_R	912,000	76,000	152,000	76,000
$Q_{loading}$	143,750	143,750	148,890	151,590
Q_{phonon}	267,44	267,44	1,1475,000	1,487,000
Q_{TED}	6,594	65,790	1,160,000	1,879,300
Q_{total}	1000	2000	3000	14000

CHAPTER 3: Microfabrication

In this chapter, the process steps that were developed to synthesize the SAW resonators and the SAWG were discussed. Then, the process modifications to incorporate the photonic components and realize the AOG were pointed out.

The fabrication process for the making of the very first SAWG was based on a standard SAW process [15]. As most SAW technologies, Al electrodes were used. The only difference is that the pillars were realized on a second layer using gold (Au) because of its large mass density. The large mass density helps in getting a high Coriolis mass in a small form factor. The first version of our SAWG adopted the same methods of fabrication but used a different LN crystal cut (Y-cut LN instead of Y-128 LN) and imposed the wave propagation direction to be $\pm 45°$ to ensure symmetry between drive and sense resonators.

It is obvious that the SAWG fabrication process is much simpler than any of the manufacturing methods used to make any MVG since it does not require any release process and uses only two masks. However, other challenges were encountered which required some substantial modifications of the fabrication techniques, process flow and electrode materials.

Although the $\pm 45°$ design guaranteed inherent frequency matching, it is quite challenging to do rotation angle alignment of the wafer especially for the 1st mask where there are no alignment features on the wafer. A second major challenge related to alignment is the effect of poor registration between the 1st layer for the definition of the Al electrodes and the 2nd mask for the synthesis of the pillars. A misalignment prevents the pillars form vibrating at the peak of the SAW vibration. It also leads to pillar vibration in an orthogonal direction, which adds a parasitic gyro axis and affects the cross-axis sensitivity. In addition, rotation angle misalignment in the 2nd layer can lead to SAW scattering, which increases the quadrature signal and induces scattering loss which affects the Q of the SAW resonators.

The electrode material property is another important design aspects that was discussed in the previous section. The acoustic behavior of Au is quite different from that of Al due to the huge difference in mass density and Lame' constants leading to a huge difference in acoustic impedance between the electrodes' regions (Al reflectors + IDTs) and the pillars' region (Au). This difference leads to significant bulk scattering as discussed in section 2.3.6. In addition, Au has one of the highest TED coefficients for metals making it not a suitable choice for high Q. For comparison $TED_{Au} = 167\ dB/cm$ is several time the$TED_W = 0.5\ dB/cm$ of tungsten at 1 GHz. Although we are operating at low frequency where TED is not the dominant factor, a low Q TED still has an impact on the overall Q of the system.

In the following sections, we discuss the modifications we did to the lithography alignment process to guarantee frequency matching and minimize rotation angle misalignment in a SAWG. We also demonstrate the modified process flow to mitigate all the previously discussed challenges and describe the deposition techniques for the use of tungsten (W) instead of Al. In section 3.2, we show the fabrication of the first AOG prototype and discuss briefly the modifications done to reduce the optical losses due to fabrication imperfections. We also discuss in detail the challenges that were faced to integrate both the acoustic and photonics processes in a single compatible flow for the AOG. In addition, we presents the efforts to integrate a laser source and detector for the photonic read-out in order to get an integrated standalone solution in section 3.3.

The verification of the previous points was done through the fabrication of several version of gyroscopes. For the SAWG, three versions where fabricated. The 1st prototype was fabricated using the conventional process. The second version (modified version) was fabricated using the modified self-aligned process introduced in section 3.1.2. In the third version, the same self-aligned process was used in addition to the application of the

developed frequency matching technique introduced in section 3.1.1. Concerning the AOG, two versions only where fabricated, one using the conventional process and the other using the self-aligned one.

3.1. Acoustic Process

The fabrication process flow for the making of the SAWG is depicted in Fig. 3.1. A Y-cut Lithium Niobate single sided polished 4'' wafer is used. The first fabrication step is the lift-off of evaporated Al thin film (Fig. 3.1.a), which was selected to be within 300 to 600 nm thick ($h = 1 - 2\%\,\Lambda$) and used to define the IDT and reflector electrodes. The Al was sputtered using magnetron sputtering CVC system at Ar pressure of 5 mT, power of 250 W and Ar flow of 50 sccm from a 12-inch target resulting in a deposition rate of ~ 20 nm/min. After this step, a Au layer lift-off was performed (Fig. 3.1.b) for patterning of the pillars.

Figure 3.1: Fabrication process flow for making the SAWG. a) Al lift-off step used to define the electrodes.

Au was sputtered using 6J magnetron sputtering system at Ar pressure of 10 mT, power of 50 W and Ar flow of 40 sccm from a 6-inch target resulting in a deposition rate of ~ 5 nm/min. Au was also used for coating the Al pads to enable wire bonding for testing purposes. In both lithography steps, positive photoresist (AZ 4210) was used to define the electrodes and pillars. MA6 was used for exposure for 160 seconds using i-line wavelength at 5 mW/cm^2. AZ developer was used and diluted 2:1 relative to DI water. The photoresist thickness (~ 3.5 µm) was selected to simultaneously facilitate a clean lift off (without sharp

sidewall edges) and the definition of the small feature size of the pillars ($W_p = \Lambda/4 =$ 7.5 μm) and shorten the sonication time.

3.3.1. Frequency Matching

As presented in section 2.3.2, frequency matching was crucial in boosting the sensitivity of the SAWG. Although the crystal symmetry solved tolerance problems, the angular alignment before the exposure step imposes a great challenge. Taking into consideration that there are no features on the wafer, the wafer placement and alignment was done visually. Using this technique, we were able to measure frequency mismatches of 24 kHz to 40 kHz for $\Lambda = 30\ \mu m$ devices (0.21 % to 0.35 % percent of f_o) as shown in Fig. 3.2. This corresponds to about $0.1°$ to $0.2°$ of rotation angle misalignment, which was extracted from Fig. 3.3 using $\Delta\theta = \frac{1}{\Lambda}\frac{\partial v}{\partial \theta}$.

To decrease the frequency mismatch an alignment method was developed as shown in Fig. 3.4. In this method, outer dimensions of the wafer, the bottom notch specifically, were used to align the mask to the wafer. Features matching the wafer dimensions where included in the mask design to be used during this alignment process.

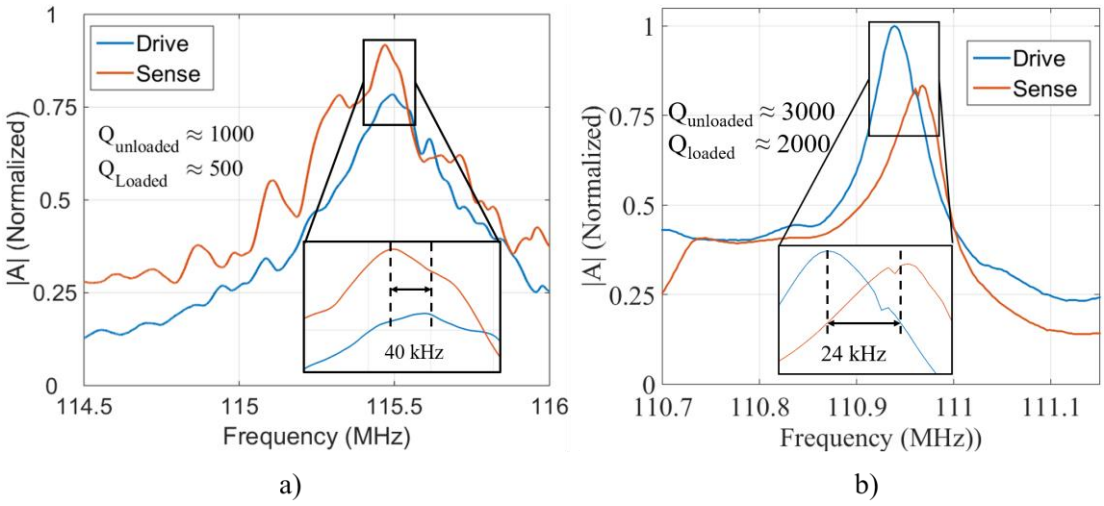

Figure 3.2: Loaded frequency response for the drive and sense cavities where a) is for the 1st SAWG prototype while b) is for the 2nd version.

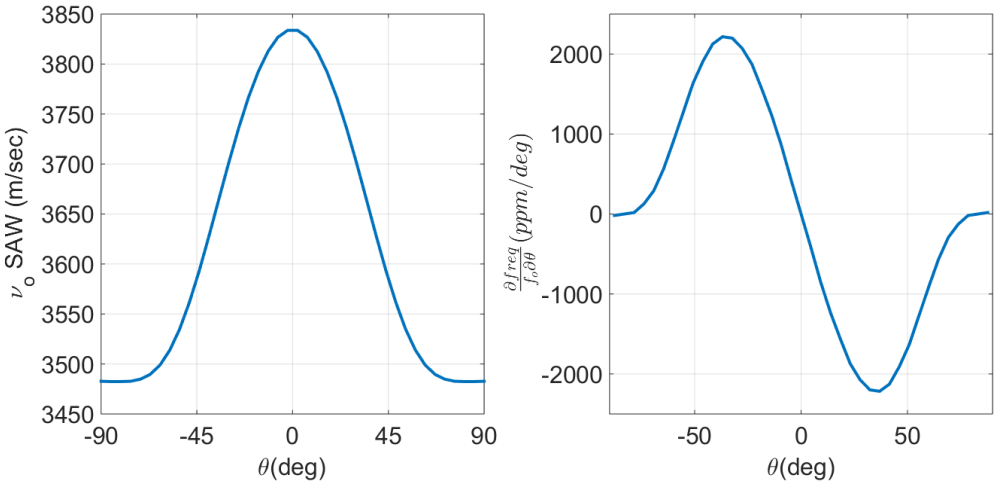

Figure 3.3: Theoretical method to estimate the rotation angle misalignment error where a) is the SAW velocity in Y-cut LN while b) is the normalized frequency mismatch per rotation angle.

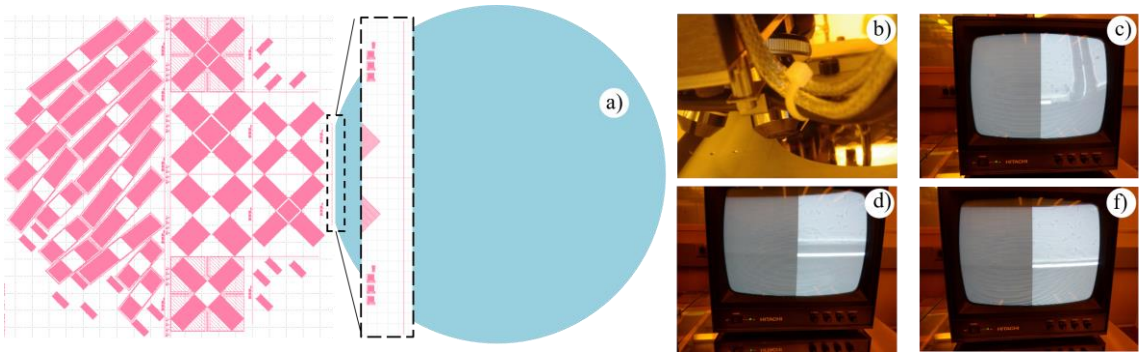

Figure 3.4: Alignment steps used to align the 1st mask (layer zero) to the notch of a 4 inch wafer where a) shows the structures used for alignment while b) to f) show the actual alignment process on MA6 mask aligner. In b), the microscope was set at the edge of the mask where the alignment feature was aligned to the edge of the wafer as in c). In d), the microscope was moved to the other side as far as possible where the wafer was aligned to the feature on the other side by correcting the rotation angle as in f). Accurate alignment was achieved by going from c) to f) in several cycles.

Using this process the frequency mismatch decreased to what is equivalent to 0.03° of rotation angle misalignment. Using this method, the frequency mismatch is now limited by the error in cut angle which is 0.02° according to the wafer's datasheet [52] and is $<$ 100 ppm of mismatch relative to f_o as shown in Fig. 3.5.

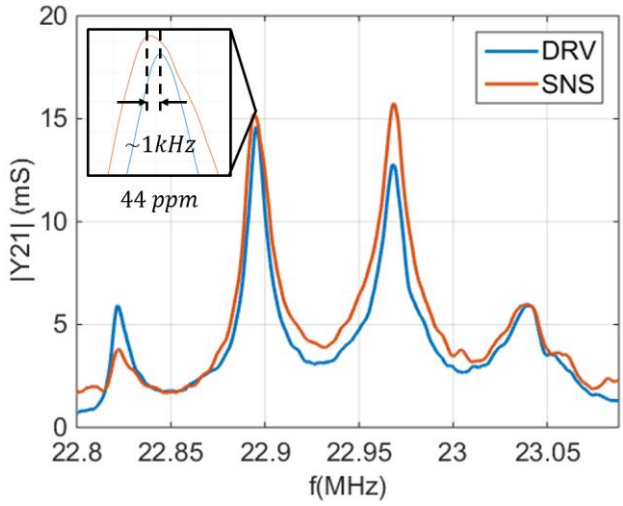

Figure 3.5: Drive and frequency response of the 3rd version of SAWG showing a very close matching with mismatching (Δf≈1kHz) which is equivalent to 44 ppm relative to f_o.

3.3.2. Quadrature minimization

As mentioned in section 2.3.5, conventional metal pillars were replaced by pillars built from LN in order to minimize quadrature. In this section, the process to realize those pillars is introduced. The pillars were built by groove etching the LN substrate as shown in Fig. 3.6.

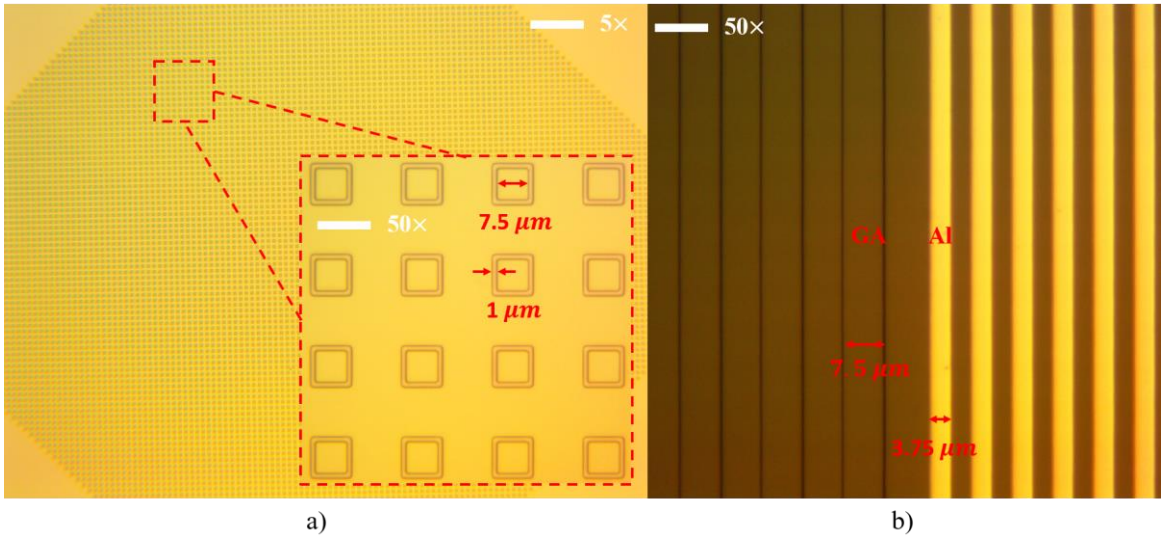

Figure 3.6: Microscope images of the process developed to minimize orthogonally reflected wave where a) shows the pillars while b) shows the reflectors realized by GA and metal electrodes using Al.

To minimize the impedance mismatch due to the grooves, the groove dimensions were set to the minimum dimensions possible which is the lithography resolution ($\sim 1\mu m$). For a $\Lambda = 30\ \mu m$ device, a $1\ \mu m$ of photoresist was used using AZ4110. Three SAW resonators where tested with and without the groove pillars where the groove pillars showed $> 15\ dB$ reduction in quadrature signal compared to conventional metal pillar. The trade-off is that the mass of the pillar is reduced by the ratio of densities ρ_{LN}/ρ_W which leads to reduction in Coriolis signal and sensitivity. This can be mitigated by the development of multi etch process or deep etch process similar to DRIE.

3.3.3. Self-alignment

Different from the process discussed in section 3.1, we developed a different process that allows for the pillars, the IDTs and the reflectors to be defined through the same mask. As shown in Fig. 3.7, the first process step defines the GA. The GA are etched using ion milling. 600 nm ($h = 2\%\ \Lambda$) grooves were etched in the LN substrate at a rate of 15 nm/min. The second step is defining the W electrodes for the IDTs and the reflectors and ultimately the pillar in the SAWG implementation. At the beginning of the process development, W features were defined using lift-off process. Some challenges were met due to side-wall effects in addition to the impracticality of lift-off for thicker films of $3\mu m$ for $\Lambda = 150\mu m$. Due to the previous, etching process using dark field mask was developed instead. W is deposited using Physical Vapor Deposition (PVD) magnetron sputtering at 50 W, whereas the Ar parameters were set at 6.68 mT and 30 sccm to achieve low stress (< 70 Mpa) and low resistivity ($\rho_{W-film} \leq 3\rho_{W-bulk}$). Using this process, we were able to perform the reflector grating study discussed in section 2.3.4. In addition, the definition of the pillars, electrodes and reflectors on the same mask minimized cross axis sensitivity and wave scattering due to pillar misalignment. With mask tolerances of 50 nm, the cross axes sensitivity went down from 10% to 1% compared to the multilayer alignment process with

misalignment error of $\geq 0.5\,\mu m$ for a $\Lambda = 30\mu m$. This value is drastically decreased by using longer wavelengths. For example, if $\Lambda = 150\,\mu m$ considering the SAW wave as a sinusoidal, mask tolerance of 50 nm results in $< 6\,ppm$ cross axes sensitivity. This developed process was used in the reflector study discussed in section 2.3.4. Eventually, the SAWGs where fabricated using W layer only in order to accelerate the fabrication process and prototyping where the reduction in reflectivity was compensated by increasingN_{ref}.

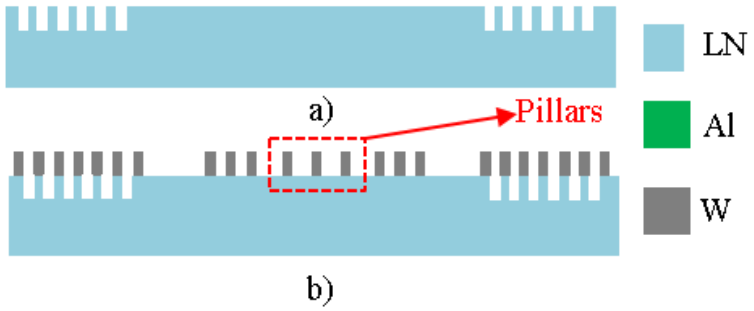

Figure 3.7: Fabrication process flow for the DL and resonators studied herein where a) is the processing step of GA while b) is the processing step of the metal film. The same identical process is used for the making of the SAW.

Some challenges were faced during the optical alignment of the second mask due to the low contrast between the etched groove and the surface of the wafer resulting in misalignment of $\geq 0.5\,\mu m$. This leads to a phase mismatch between the MA reflector and the GA reflector leading to reflectivity reduction. To overcome this challenge, a self-aligned groove process was proposed. The idea relies on results and conclusions in section 2.3.4 where the MA+GA interleaved reflector grating achieves the highest reflectivity and lowest radiation loss. As shown in Fig. 3.8, all the SAWG components even the grooves are defined in a single lithography step using the electrodes mask which ensures absolute alignment between MA and GA. The second mask was used to protect the cavity during the ion milling step. Although the second mask still requires alignment, it has wide

tolerances ($\Lambda/8$, 3.75 μm for $\Lambda = 30\ \mu m$) which could be easily aligned using a mask aligner leading to no misalignment effect on the SAWG.

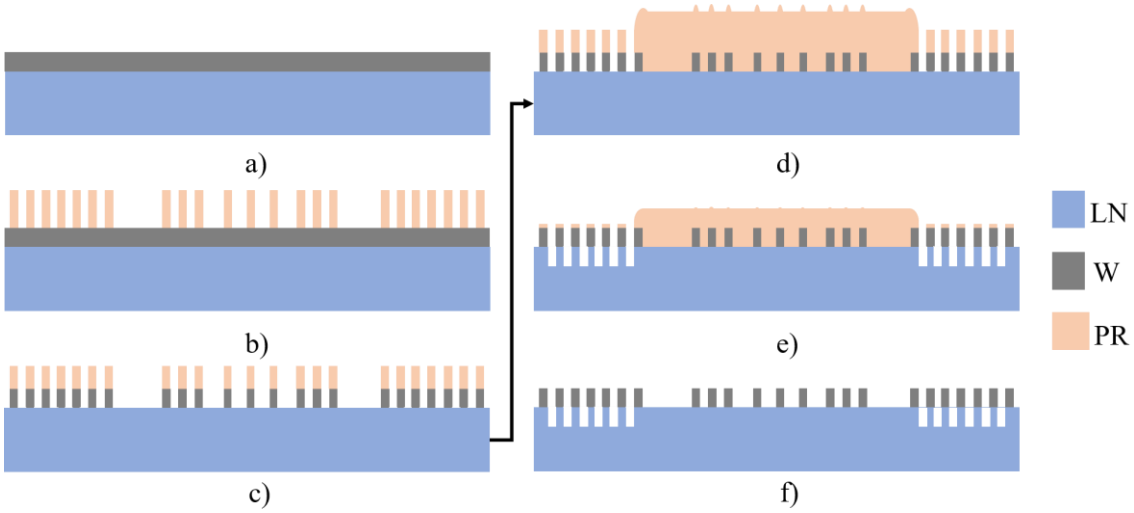

Figure 3.8: Modified self-aligned process for both pillars and GA grating reflectors where a) is the W deposition step, b) is the 1st self-aligned lithography step, c) is W etching step, d) is the cavity protection lithography step, e) is the GA ion milling step and finally f) is the PR strip.

3.3.4. Metal Deposition

One of the challenging process steps for the SAWG is the metal electrode deposition. The metal used is required not only to provide high electrical conductivity to minimize ohmic losses but also have large mass density for synthesizing the Coriolis mass, high reflectivity for reflector gratings and low TED to achieve high Q. Unfortunately, deposited metal films have worse mechanical and electrical properties compared to that of the bulk metal. Due to the previous considerations, various metals were deposited to study their performance and behavior. The density of the deposited film was characterized using A&D Precision Weighing Balance HR100AZ where no significant difference was found compared to bulk density. However, a significant difference in film resistivity was noticed.

The resistivity of different metal films was studied using a serpentine resistor as show in Fig. 3.9. The extracted values of resistivity are summarized in table 3.1. Although the resistivity of bulk Pt is the highest in the materials studied, it shows better film resistivity

than that of W. However, Pt is a noble metal which cannot be chemically etched neither by chlorine nor fluorine based gases. Al shows the lowest resistivity but it has a very low density compared to W. Evaporated metal can give the lowest resistivity but at the expense of deposition rate and film thickness limitation. W metal was eventually selected since it is easy to be processed beside its high density. The only drawback is the resistivity of the W film which was minimized by the optimization of the deposition parameters.

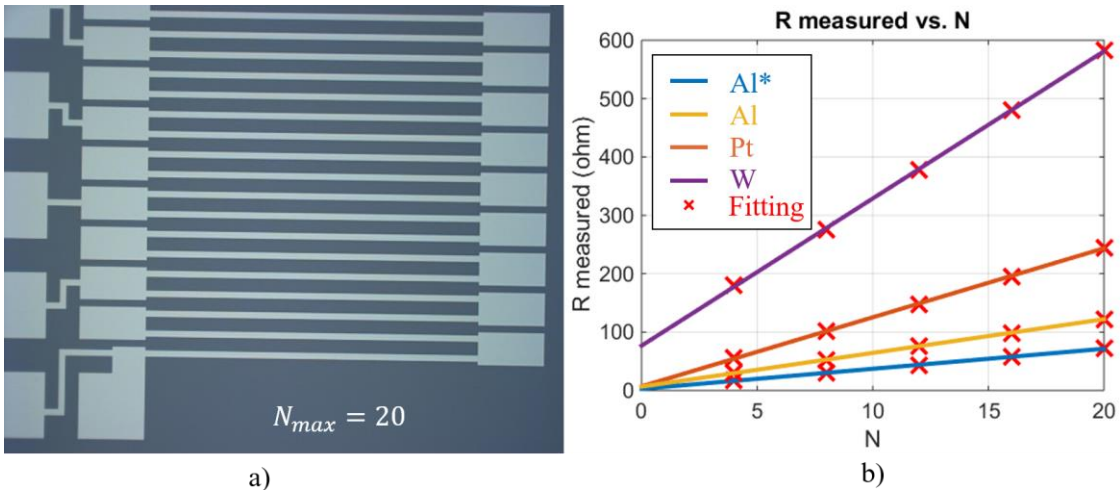

Figure 3.9: measurement of resistivity of deposited film using serpentine resistor structure.

Table 3.1: Summary of bulk and film resistivity of studied metals. *: evaporated film.

Metal	**Bulk resistivity ($\Omega m \times 10^{-9}$)**	**Film resistivity ($\Omega m \times 10^{-9}$)**	**Film resistivity ($bulk\ normalized$)**
W	56	317	6.10
Al	26.5	43.8	1.55
Al*	26.5	73.7	2.61
Pt	106	151	1.44

Another challenge was the stress in the deposited film which can cause cracking or delamination of the deposited film. For the previous reasons, a series of deposition runs were performed to study the properties of deposited films. We focus on W due to its advantages mentioned in section 2.3.4.

As shown in figure 3.10.a, the stress changes from tensile to compressive with the increase in Ar plasma gas pressure for a fixed power where the power changes the slope of the relation. The power stress relation saturates at neutral stress for high pressure but at the expense of very high resistivity as in Fig. 3.10.c. The resistivity is directly proportional to pressure where the power has negligible effect on resistivity at low pressures as in Fig. 3.10.d. In addition, the deposition rate is a linear function of power with negligible effect from the pressure as in Fig. 3.10.e. As shown in Fig 3.10.f, high power low pressure depositions was linearly fitted where the neutral stress is expected to be achieved at 630 W with minimum resistivity of $< 3\rho_{bulk}$.

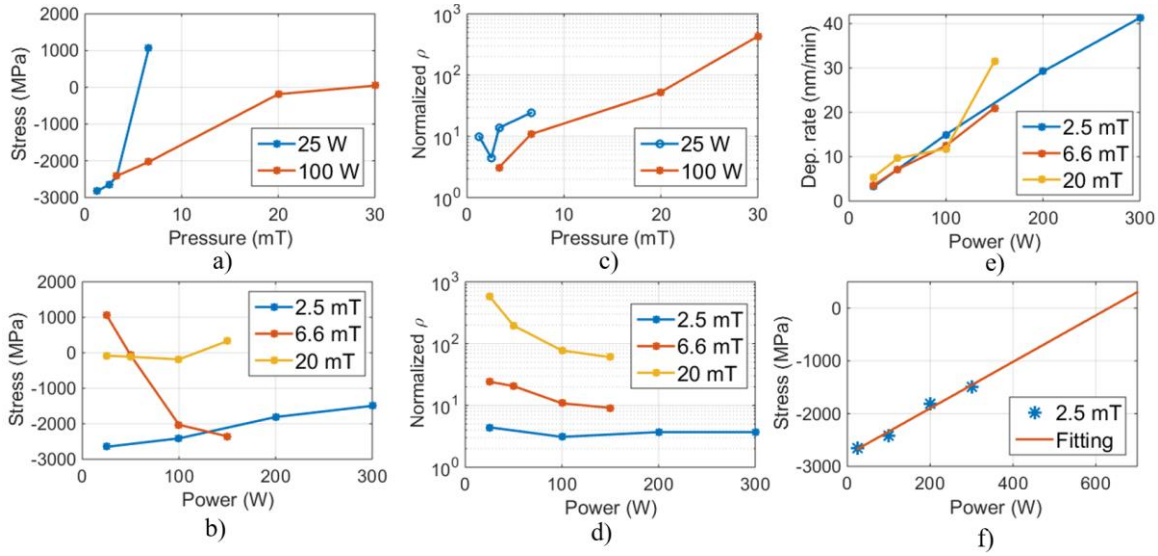

Figure 3.10: Study of the properties of deposited W films using 5T deposition system where a) and c) study the stress and resistivity vs pressure at 25W and 100W of deposition power while b) and d) study the stress and resistivity vs power at 2.5, 6.6 and 20 mT of Ar pressure. e) Shows the linear dependence of the deposition rate on power at 2.5, 6.6 and 20 mT of Ar pressure while f) study a special case at low pressure to estimate the neutral stress point.

Unfortunately, this power is two times higher than the maximum power rating set for the tool. Instead, an optimum point was found at a pressure of 6.6 mT and 50 W where the stress is crossing neutral axes and the resistivity is acceptable.

Implementing the lessons learned from the previous study, a more advanced tool, Kurt Lesker PVD system, was used to deposit W films. This tool was able to provide not only

films with optimized resistivity of $\rho_{film} < 3\rho_{bulk}$ and stress of $< 100\ MPa$, but can also achieve good film uniformity of $< 2\%$ which had a direct impact on the frequency response of SAW and Q as discussed in section 2.3.6. The characterization of the deposition parameters for this tool are shown in Fig. 3.11.a and b. The power was 50 W while the pressure 4.9 mT. Although the slope at this pressure seems steep at this point, the tool has a controller that maintains the pressure value to the third decimal point. The resulting film thickness distribution measurements are also shown in Fig. 3.11.c. The film thickness was measured using KLA Tencor P-15 Profilometer on a 4 inch wafer with grating features.

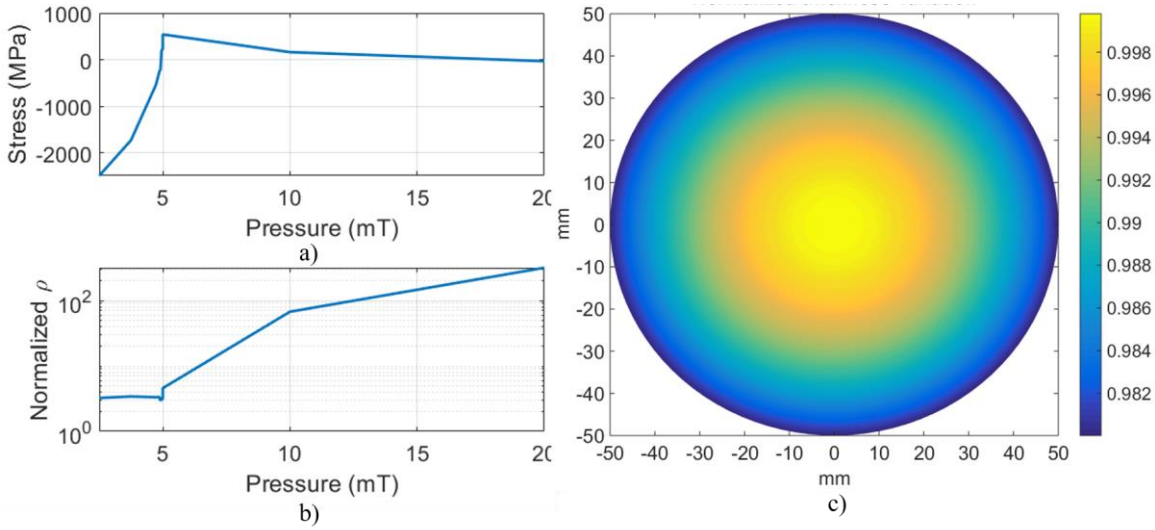

Figure 3.11: Study of the properties of deposited W films using Kurt Lesker PVD system where a) and b) show the stress and normalized ρ vs Ar gas pressure while c) shows the contour plot of thickness variations.

3.2. Photonic Process

This section describes the integration of the photonic components with the SAWG.

A key challenge is ensuring the steps for the etching of the photonics components (described in [53]) is compatible with the fabrication of the SAWG, i.e. the deposition and etching of the W electrode layer. It was found that the RCA step used to clean the photonic waveguides after the LN etch attacks the W layer. To address this problem, we reversed the order of the fabrication process and defined the photonic components before the SAWG.

The SAWG was defined last where a blanket tungsten metal was deposited and then etched. In some cases, the deposited film did not have strong adhesion force with the LN surface which lead to film delamination. This issue was mitigated by using a thin film of titanium (~ 10 nm) adhesion layer. Another issue was encountered this time due to the reversed process order. The etch of W+Ti lead to residuals on top of the surface of the LN as shown in Fig. 3.12.

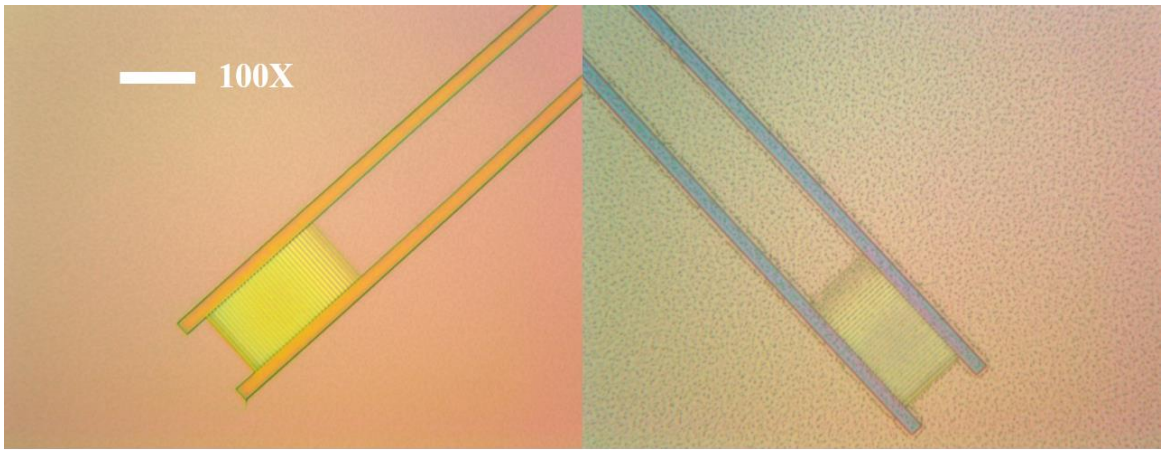

a) b)

Figure 3.12: Microscope images of photonic grating built on LNOI showing the effect of residue redisposition. Images show the gratings a) before and b) after W etching.

Although the film did not have a considerable effect on the SAW performance, it exhibited a serious impact on the photonic losses of the waveguides. To solve this issue, a lift-off process was developed. Unlike the lift-off used in the 1st SAWG process, this process was done using negative photoresist as shown in Fig. 3.13. Due to the nature of the resist, its sidewalls after exposure have a negative slope which eliminates the sidewall coverage issue generally associated with performing lift-off via sputtering, relaxes the resist to metal thickness requirements and shortens the sonication time. In this process, NR9-3000PY resist was used, which was spun at 1000 rpm resulting in a coated film of ~ 5 μm. The resist was post baked for 20 min at 95 $°C$, exposed for 30 sec using i-line 5 mW/cm^2 MA6 mask aligner then post baked for another 20 min at the same temperature. The film was developed for 15 sec where the resulted resolution is ~ 3 μm with a negative sidewall angle of 43°.

After film deposition, the lift off was done by sonicating the sample in acetone for 1 hr. This process helped in isolating contamination from the photonic waveguides since they are covered by the photoresist during deposition. In addition, the resulted tilted sidewall of electrodes and pillars is expected to provides a gradual acoustic impedance mismatch between the electrodes/pillars and substrate and has the potential of minimizing the bulk scattering loss as pointed out in section 2.3.6.

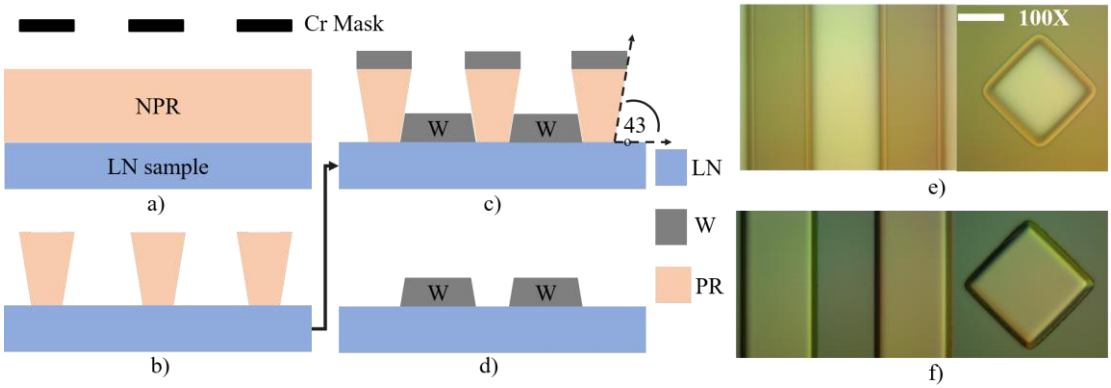

Figure 3.13: Negative PR process used to avoid optical waveguide contamination and bulk loss where a) to d) show the process starting from exposure, development, W depositions and NPR strip while e) and f) are microscope images showing the features realized in NPR and the electrodes and pillars after lift-off.

3.3. Assembly and Packaging

For a gyroscope required to sustain high G-shock $> 50\ kG$, not only the gyroscope design is what defines its performance but also the package and die attachment. Three different packages where used (shown in Fig. 3.14) for the three SAWG variants discussed in this thesis. For two of them, ceramic packages were used due to their hardness and durability. The package number was selected based on the cavity size required to fit the SAWG die. The 1st SAWG prototype had a die size of $7.8 \times 7.8\ mm$ and fitted in Dip-28 package while the 2nd generation had a die size of $16 \times 16\ mm$and was mounted first in a PGA package ,then replaced with LCC84 to minimize parasitic. The latest version of the SAWG had a larger die size of $40 \times 40\ mm$ due to Λ scaling from $30\ \mu m$ to $150\ \mu m$. To the best of our

knowledge, there are no commercial ceramic packages with such a wide cavity. Hence, red a custom packaging technique was needed The die was mounted on a PCB (chip on board, CoB) where a 3D printed structure was used to support the PCB and minimize bending and stress effects on the die.

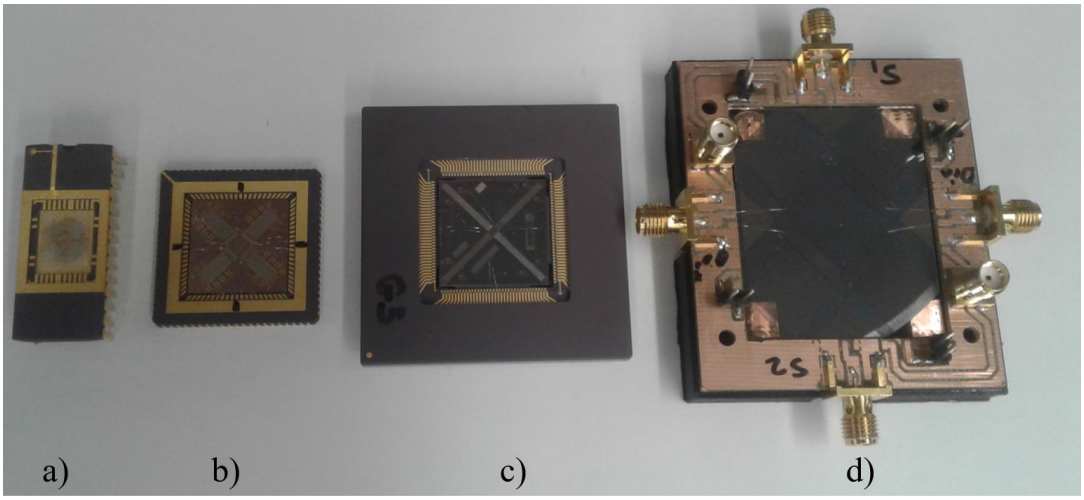

Figure 3.14: Various packages used for SAWG/AOG packaging where a) is Dip-28, b) is LCC84, c) is PGA 280 while d) is a custom CoB and 3D printed package.

Several methods of die attachment were tested. A basic method was tried where the die was attached using carbon tape at the 4 edges. This was not only an easy method for packaging the SAWG, it also did not apply high stress on the die due to the tape's elasticity and helped in acting as pedestals to thermally isolate the die from the package. This was really helpful in minimizing thermal leakage into the substrate and increase the ovenization efficiency as discussed in section 4.3. The drawback is the robustness of this method and questionable survivability during shock testing. To avoid this drawbacks, silver epoxy was used. Although the durability and survivability were better than when carbon tape was used, another problem was observed. The die attach induces stress on the die after being cured and shifted the SAW frequency by ~1%. Theoretically, it should not be a problem for an inherently matched SAWG with a controlled ovenization system, but practically, the asymmetry in the die attach induces asymmetric stresses, which lead to frequency mismatch. Although several attempts were made to symmetrically distribute the epoxy and

contain it around the edges, none was successful in eliminating the mismatch. From literature, eutectic bonding seems to be the perfect solution for the previously discussed problem [54]. However, it requires an additional fabrication process in addition to a bonding machine. For the purpose of our testing, the carbon tape was used in combination with a low hardness and low thermal conductivity glue [55]. With that, conductivity, durability and stress problems were solved.

A possible problem with this approach is the reduction of sensitivity and decrease in mechanical response time due to the flexibility of the tape and glue. This problem was not encountered due to the high Ω and small oscillation bandwidth used during characterization. To connect the die to the pins of the packages, wirebonds were used. The wire-bonding was made of 1 mil Al wire using westbond 7476D wedge bonder. A circuit model was developed to simulate the effect of the parasitics on the SAWG frequency response and coupling, which was found to be negligible.

In the first demonstrations of the AOG, an external tunable laser was used as a light source and external photo-detectors were used to convert the optical read-out to a measurable voltage. The light was getting in and out the photonic devices using a vertical groove array (VGA) connected to a fiber bundle, which coupled the light to optical grating. It required a significant time and skill to align the VGA to the optical grating to achieve maximum coupling. In addition, such setup imposed significant limitations on the testing and installation of the AOG in the field. Minor variations in the alignment due to vibrations induced during rate table testing can affect the gyro scale factor (SF). Due to the previously described challenges, a process was developed to integrate a vertical cavity surface emitting laser (VCSEL) as the optical source and a photodiode (PD) as the optical detector on chip. Flip chip bonding was the method used to 3D integrate these components on the LN chip (see figure 3.15).

The dies are bonded using gold eutectic bonding where the substrate is heated to 200 °C and a pressure of ~ 300 μN is applied using M9A device bonder. Having no bottom contacts, the VCSEL bonding process was done manually. For high shock survivability, the dies are glued using infrared transparent glue which doesn't alter the optical coupling at the operating optical wavelength. Furthermore, an extra step was added to the PD integration process to form electrical contacts to it. The top surface and a nearby pad were shorted using conductive silver epoxy. This extra step minimizes the damage caused to the surface of the PD during wirebonding and increases the overall yield of the bonding process.

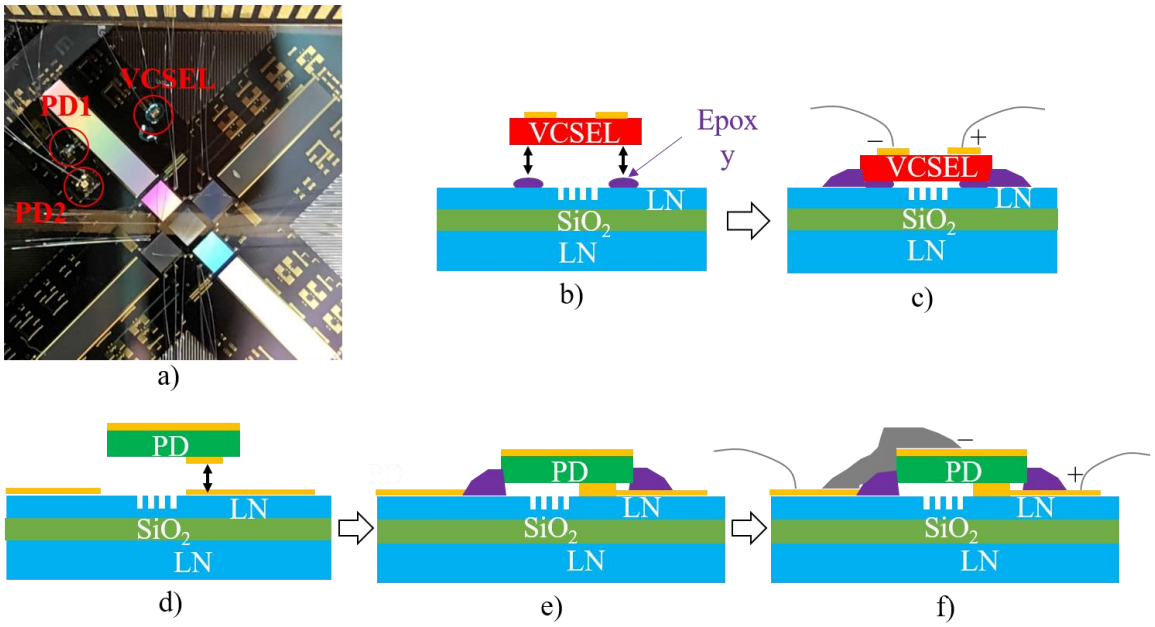

Figure 3.15: Diagrams showing a microscope image of integrated VCSEL and PDs in a) and the integration process flow for VCSEL and PD: b) VCSEL bonding and gluing c) wirebonding, d) PD bonding, e) PD gluing and f) PD top pad contact formation and wirebonding.

CHAPTER 4: Gyro Control System

In gyroscopes, feedback control theory is usually employed to optimize the response of the system and improve its overall performance. For highly accurate sensing, the control infrastructure can become complex and a number of control loops are running in parallel. Therefore, low noise and high stability are natural, guiding principles to develop gyroscope control systems. Understanding the system's dependence on gyroscope noise behavior has a number of rewards, such as being able to establish relevant requirements for the feedback sensing element or, conversely, analyzing the system-level response to noise in a particular gyroscope.

Due to the previous considerations, practical implementations of drive loop, open-loop sensing and thermal loop are presented in this chapter. It will first be explained how to perform a basic gyroscope drive-mode control by means of a phase-locked loop (PLL) and automatic gain control (AGC). All the control loops were implemented in UHFLI lock-in amplifier [56].

The UHFLI comprises eight dual-phase demodulators with two input/output channels, 4 auxiliary outputs and two auxiliary inputs, two PLLs, and two PIDs.s In order to understand how the UHFLI is used for gyroscope applications, it is helpful to explain the internal structure of the instrument. The most essential component of every lock-in amplifier is the demodulator, which performs a very narrow-band filtering of the signal of interest around a determined frequency. The result of the demodulation is a precise measurement of the amplitude and the phase of the signal even when the signal is seemingly covered by noise.

4.1. Drive Control Loop

For the drive-mode control, the oscillation of the vibratory gyroscope is maintained at resonance by means of a PLL. Furthermore, the mechanical amplitude is kept constant

using a PID controller. Otherwise temperature drift may degrade the performance of the gyroscope. The drive loop setup is described in Fig. 4.1. The drive-mode of the gyroscope is connected to input and output of the UHFLI.

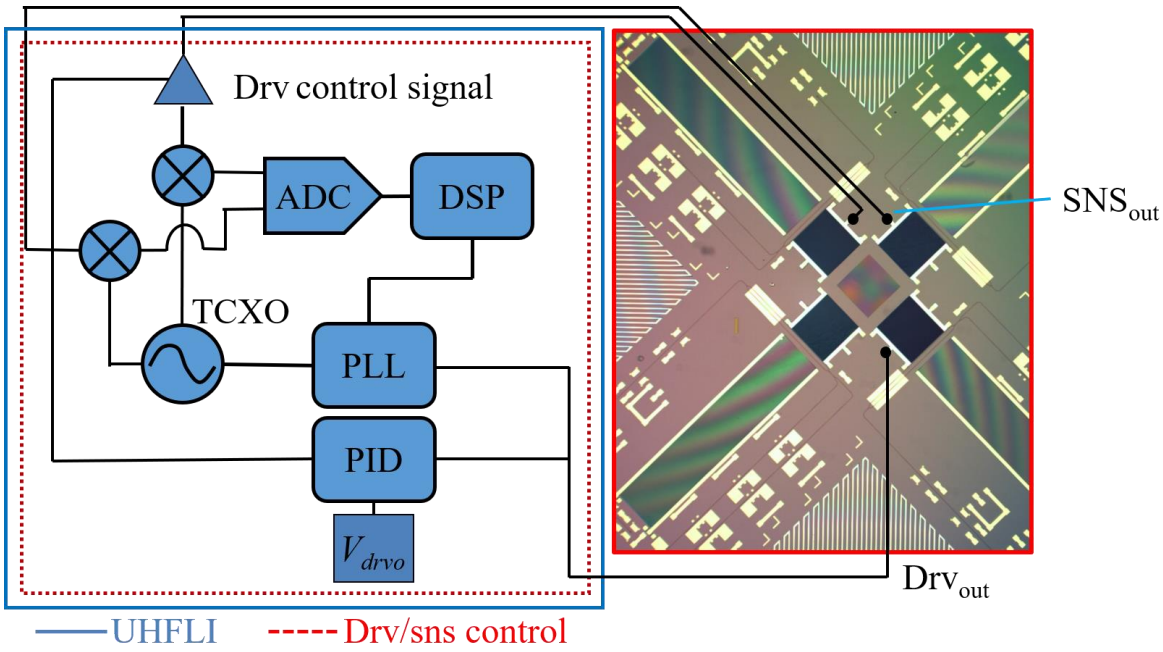

Figure 4.1: Open loop sensing control system of SAWG showing the drive control loop and the sense read-out.

The PLL locks to the resonance frequency of the drive mode. For the excitation of the drive-mode, the 1st modulator in the UHFLI is used. The phase of the modulator is set to maximize the amplitude of oscillations, which occurs at the resonance frequency, f_o. Considering a second order mechanical system, the theoretical phase at f_o is 90^o relative to the excitation force. Practically, parastics and coupling can deviate the value of the phase at resonance. To determine the exact phase at resonance, a frequency sweep was done first in the UHFLI where all components are connected. By setting oscillator 1 to be controlled by the PLL, the control loop is now closed. The operation of the PLL loop is either verified by the lock check in the UHFLI or by plotting PLL phase error and extracting its STD. The phase error STD reflects the phase noise, which is highly affected by the quality factor of the SAW resonators. Our measurements showed that optimized PLL parameters and Q enhanced from ~ 1000 to 14000 can decrease the phase error STD from 17 $mdeg$

to 0.68 $mdeg$. In addition, an AGC loop keeps the excitation amplitude constant. The AGC uses a PID controller to compare and regulate the drive mode oscillation amplitude to a given set point. Demodulator 2 in the UHFLI serves as an input to the PID controller. The AGC loop operation was verified applying oscillatory input rotation and monitoring the drive signal. PID parameters are then tuned until oscillatory signals due to input rotation are decreased below the noise floor.

4.2. Sense Readout

In this section, we explain the techniques used to sense the output of the SAWG and AOG. We demonstrate how the control system parameters of the UHFLI affect the final performance of the gyroscope.

4.2.1. SAWG

In the simplest gyroscope instrumentation, the gyroscope drive-mode control is applied as described in the previous section, while the sense-mode is implemented in open loop. This scheme is one of the basic operation principles and is widely used.

In our setup, Demodulator 3 is connected to the gyroscope sense-mode output. Demodulator 3 uses Oscillator 1, which is controlled by the PLL. The demodulator phase shift is adjusted to ensure the Q-component (90° quadrature component) of Demodulator 3 is the Coriolis output proportional to the angular rate, while the 90º component is the quadrature error. Theoretically, the phase of the sensing voltage is given in table 4.1 for our inherently matched SAWG. Practically, the phase could vary from -90 degree to 90 degrees depending on the frequency mismatch but mostly due to the parasitics. The phase is typically set by trial and error by sweeping the demodulation phase while input rotation is applied to the gyroscope until the quadrature component is not sensitive to rotation.

Table 4.1: Summary of the relations that dictates the values signal phases

Signal	Expression	Phase (degree)
Drive voltage (V_d)	$V_d = v_d \cos(\omega_o t)$	0
Surface potential (ϕ)	$\phi = jK_t^2 V_d$	90
Drive displacement (u_d)	$u_d = c_x \phi$	90
Coriolis force (F_{cor})	$F_{cor} = -2m\Omega i_d$	0
Sense displacement (u_s)	$u_s = -j\frac{Q}{\omega_o} F_{cor}$	-90
Sense voltage (V_s)	$V_s = -j\frac{u_s}{c_x K_t^2}$	-180
Quadrature voltage (V_{quad})	$V_{quad} = -j\frac{u_d}{c_x K_t^2}$	-90

4.2.2. AOG

The AOG used the same drive control system as the SAWG. For the photonic readout, two systems were used as shown in Fig. 4.2. The first is a single ended system where avalanche photodiode (APD) is used to convert the optical output into an output voltage as shown in Fig. 4.2.a. The erbium doped fiber amplifier (EDFA) was used to amplify the optical signal, which has a direct impact in reducing input referred noise from the read-out electronics in the UHFLI. The main drawback is that the signal is susceptible to common mode signal variations, which jeopardize the stability of the gyroscope.

The other system shown in Fig. 4.2.b is a differential system. It uses a balanced photodetector (BPD) for differential sensing, which has the ability to reduce common mode fluctuations. The drawback is that it does not provide enough signal gain. The detailed results of both systems are discussed in section 5.2. Due to the complexity of the relations to track the transient phase change of the AOG signal from displacement to strain and finally to phase and voltage, the trial and error method suggested in the previous section was used.

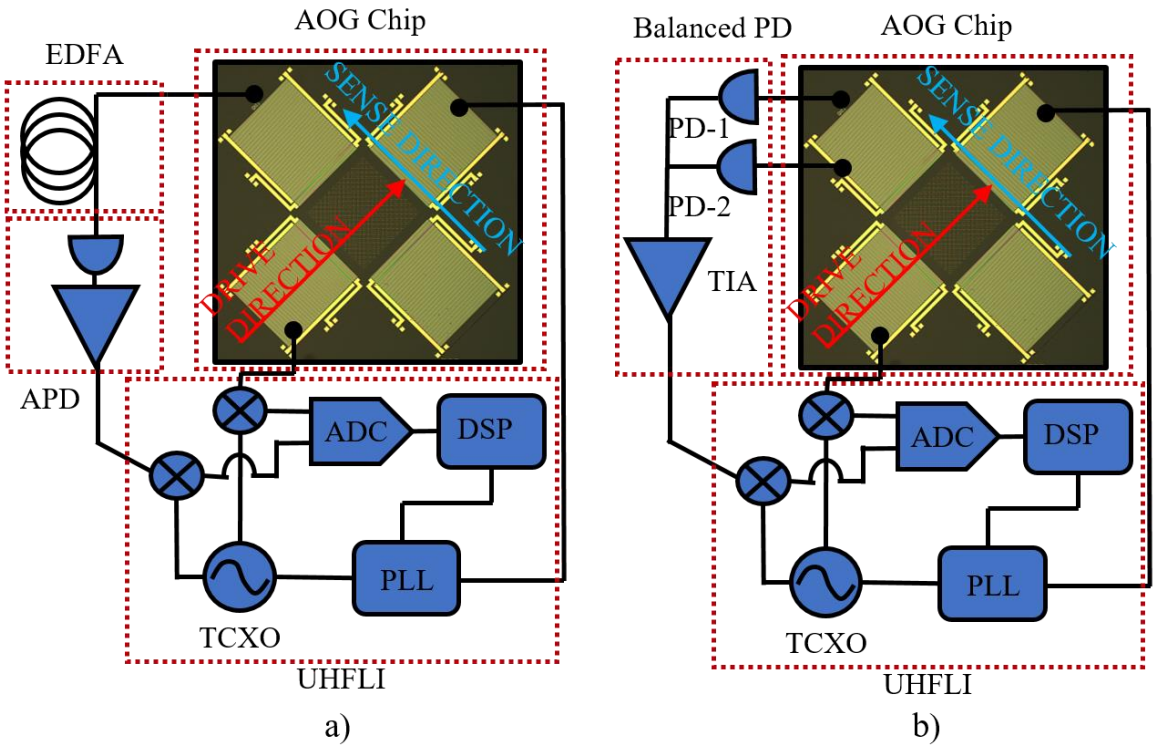

Figure 4.2: Optical read-out systems used for AOG where a) is a single ended system while b) is a differential system.

4.3. Thermal Control Loop

In this section, we present a complete set of analytical, simulation and experimental results of a monolithically integrated LNOI-based ovenization system. Moreover, we demonstrate the effect of frequency stabilization on the long-term stability of SAWG. The study was implemented by monolithically integrating tungsten serpentine heaters symmetrically placed around the SAWG as shown in Fig. 4.3.

The heaters were fabricated using Tungsten (W) due to its process compatibility with the SAW electrode mask and low electro-migration. The electrical energy dissipated in the heater is converted to thermal energy, which is used to elevate the temperature of the chip for ovenization. In the analytical model, the electrical power (P_e) was assumed to be converted to thermal power (P_T) in the heater neglecting any dissipation in the external

interconnects.

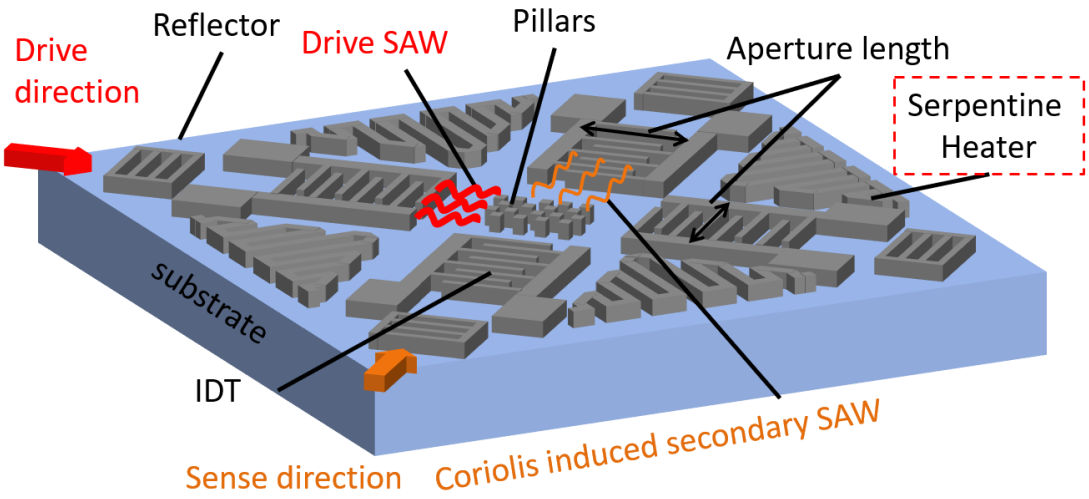

Figure 4.3: 3D sketch of the SAWG showing all the acoustic components and the integrated heaters all implemented on the same metal layer using Tungsten metal. The substrate is an LNOI wafer.

The model shown in Fig. 4.4.a was used to identify the thermal power flow in the substrate and the amount of power leaking into the package through the die attach where R_{T1} to R_{T4} are the vertical and lateral thermal resistances of LNOI substrate and die attach, respectively. This treatment was helpful in identifying that a glue thickness of ~ 50 µm, was sufficient to attain a reasonable power efficiency of 1 mW/K. The thermal capacity calculations of the system was neglected since the thermal time constant of the system was expected to be well below the drift time response of the gyroscope.

A serpentine resistive heater was designed according to the shape shown in Fig. 4.4.b selected to fit the heater in the empty areas on the die. Based on the target temperature difference from the ambient (ΔT) and the W film (of thickness t), the in-plane dimensions of the heater were designed using (Eq. 4.1 and 4.2) where ρ is the density, η is the metallization ratio of the heater, W_L and W_s are the width and spacing of the heater wire, L_h is the serpentine length while n is the number of windings.

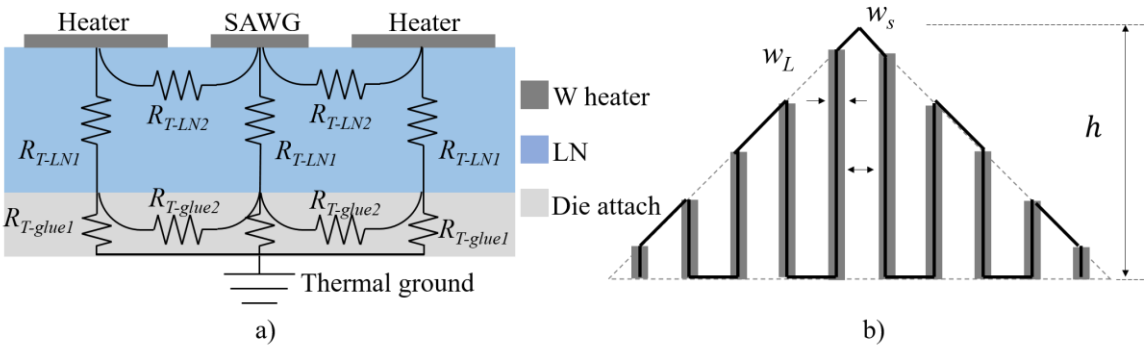

Figure 4.4: Schematic of the die cross section showing the thermal circuit model built to calculate the thermal efficiency and die attach thickness. A drawing represents the geometrical shape of the heater showing the in-plane dimension.

$$P_T = R_{T-total}\Delta T, R = \rho\frac{L_h}{tw_L} \tag{4.1}$$

$$L_h = \left[\left(\frac{n-2}{4}\left(1-\sqrt{2}\right)+\sqrt{2}\right)\eta + \left(\frac{n^2}{8}+\frac{n}{2}\left(\eta+\frac{1}{2}\right)\right)\right]w_L \tag{4.2}$$

To verify the analytical model, Multiphysics FEM simulations where performed by coupling electrical and conduction heat transfer as shown in Fig. 4.5.a. The simulations showed an agreement in the estimation of serpentine resistance which was ~ 1kΩ and close agreement for the thermal efficiency (~0.8 mW/K) as in Figure 4.5.b.

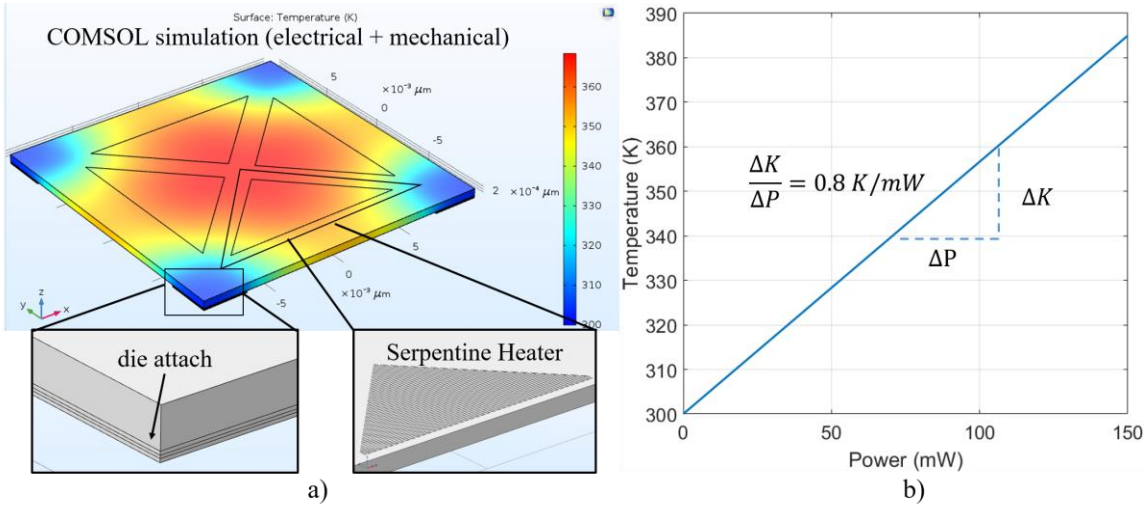

Figure 4.5: FEM simulation of the ovenized chip using COMSOL Multiphysics (coupled electrical and conduction heat transfer) where a) shows the simulated structure and a thermal map while b) shows the simulated temperature to power relation.

Using QFI Infrared (IR) scope as in Fig. 4.6.a, the operation of the heater was verified and the rise and fall times necessary for the control loop design were evaluated. The sample was mounted on a stage to reach a reference temperature of 45 ^{o}C to avoid background thermal noise. After achieving steady state temperature, the liquid nitrogen cooled IR camera was used to capture frames of thermal changes on the sample as shown in Fig. 4.6.b while turning the heater on and off to calculate thermal rise and fall time constants. The rise ($\tau_{heating}$) and fall ($\tau_{cooling}$) time constants of the heater were measured to be ~ 0.5 sec and no thermal hysteresis was noticed as in Fig. 4.6.c.

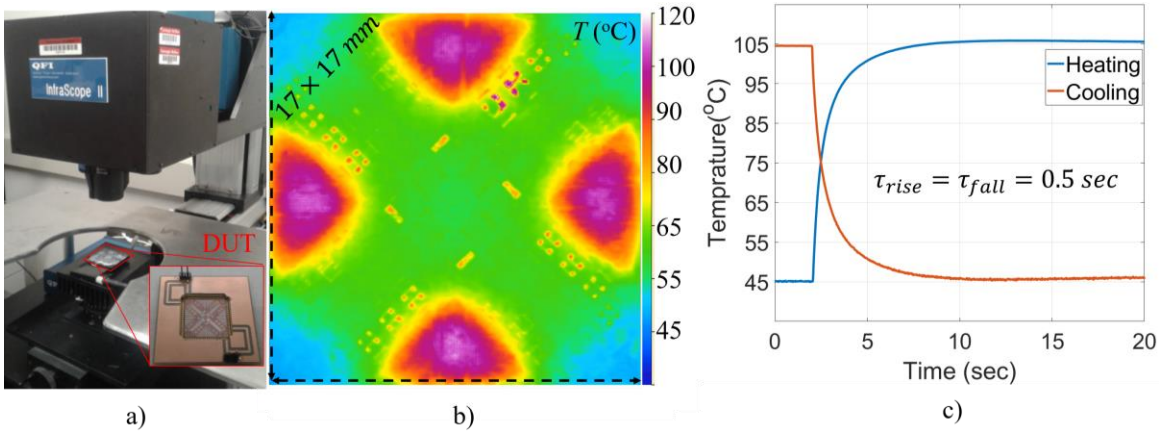

Figure 4.6: QFI infra scope used to measure the (b) temperature distribution across the die and (c) calculate the $\tau_{cooling}$ and $\tau_{heating}$.

In the test setup shown in Fig. 4.7, the heater was operated at 10 degrees above the ambient with a 90 mW power consumption. This was enough to operate the device above the ambient temperature. The power efficiency was calculated to be less than 8x what was expected from FEM simulation due to the convection heat transfer and uncontrolled die attach thickness and coverage. The first channel of the UHFLI was used to drive the SAWG while the second channel was used for the sense output. The thermal driving signal was implemented using the Aux output. Attenuators were used to avoid the desensitization of the lock-in dynamic range (100 dB) while a DC blocker and a LP filter were used to filter any self-mixing or higher order harmonics due to drive amplifier harmonics.

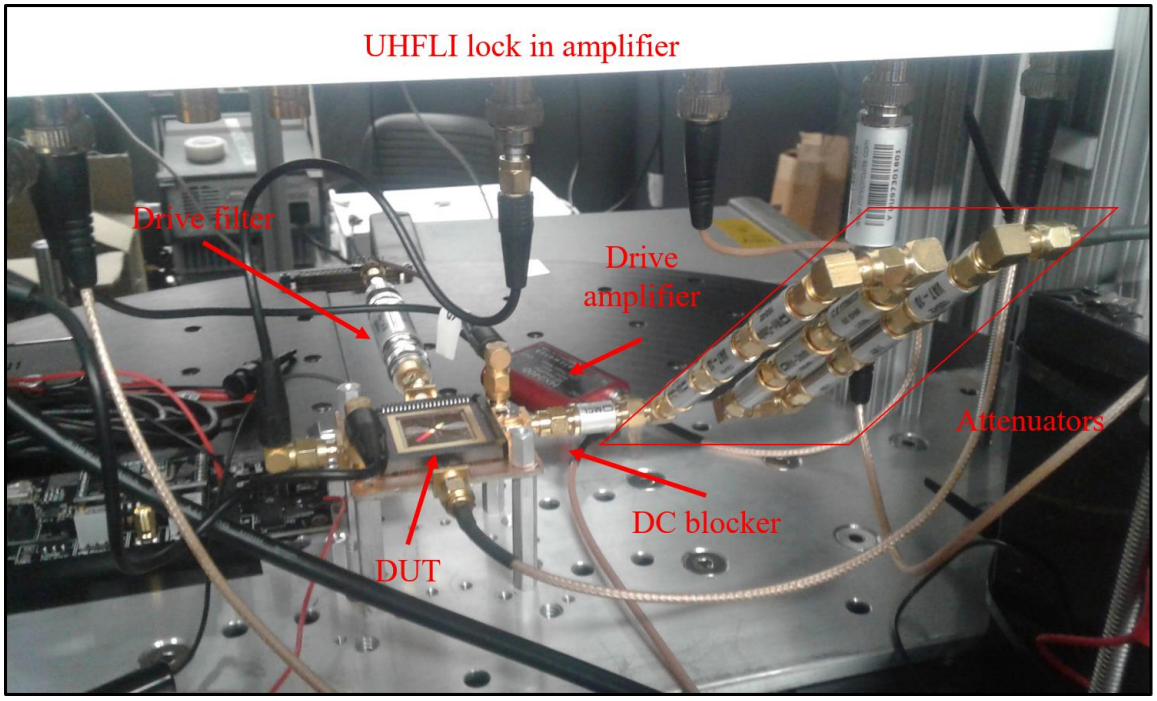

Figure 4.7 Testing setup of the ovenized SAWG showing the DUT, connections and all the components used.

Fig. 4.8 depicts the block diagram of the whole control system, which was implemented using UHFLI lock-in amplifier. The block diagram consists of two main control loops, the thermal and drive control loops. The temperature of the chip was kept constant by controlling the current flowing in the heater using the thermal control loop.

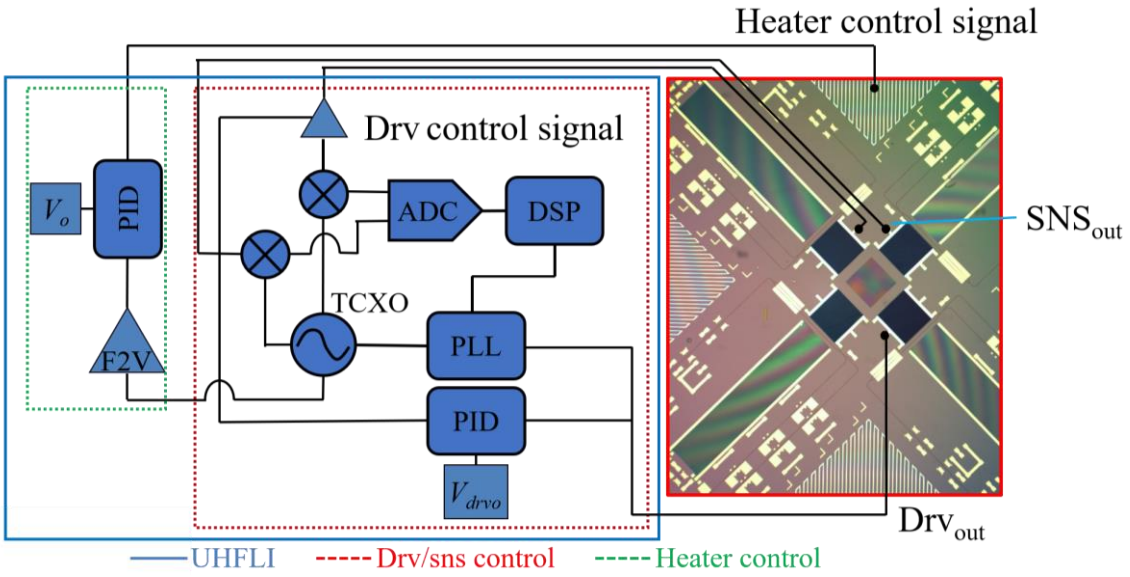

Figure 4.8: System block diagram of the ovenized SAWG showing the equivalent blocks in UHFLI lock-in used to synthesize the control system.

The loop minimizes the change in frequency using a PI controller modeled for a first order thermal system where the value of the frequency is given by the drive control loop, which is ~ 112 MHz (resonance frequency of the SAW drive). The PLL in the drive control loop tracks the phase at the peak of the SAW resonance adjusting the oscillation frequency of the VCO to maintain a constant phase.

To design the heater control loop and set the values of the PI controller, a transfer function (TF) of the heater system is needed and a block diagram is used to model the heater loop as shown in Fig. 4.9.a. Based on the analogy between electrical and thermal domain shown in table 4.2, the equivalent circuit for the thermal systems was derived as shown in Fig. 4.9.b.

Table 4.2: Summary of the analogy between electrical and thermal domains.

	Electrical	**Thermal**
Potential	V	T
Current	I	q
Resistance	$R = \frac{\rho L}{A}$	Conduction $R = \frac{k_{eq} L}{A}$
Capacitance	$I = C\frac{\partial V}{\partial t}$ Parallel plate $C = \frac{\epsilon A}{d}$	$q = C\frac{\partial T}{\partial t}$ Slab $C = c_p A$
ODE	$CV' + RV = I_{in}$	$CT' + RT = q_{in}$
TF t domain	$V = V_f\left(1 - e^{-t/(RC)}\right)$	$T = T_f\left(1 - e^{-t/(RC)}\right)$
TF s domain	$TF(s) = \frac{K}{(RC)s + 1}$	$TF(s) = \frac{K}{(RC)s + 1}$

The PI parameters where designed using the modeling equation of a PI controller given by (Eq. 4.3 and 4.5) where K, K_p and K_I are the gain, proportional and integral parameters of the PI controller, τ and τ_{loop} are the open and closed loop time constants, ω_n and ξ are the natural frequency and damping factor of the control loop while K_{f2V} is the $f2V$ gain.

Starting from the initial calculations the parameters were then tuned using Ziegler-Nichols method readily available in the UHFLI [57]. The loop parameters are summarized in table 4.3.

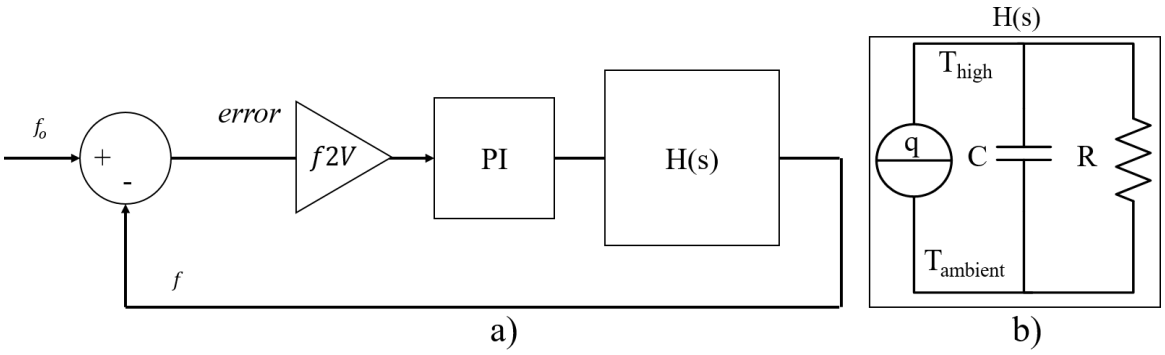

Figure 4.9: Heater control system representation where a) is the control system block diagram where $f2v$ is a frequency to voltage block, PI is the proportional integral controller while H(s) is the sensor's thermal transfer function while b) is the equivalent circuit model of the heater.

$$G(s) = \frac{1}{\tau}\frac{K\left(K_p s + K_I\right)}{s^2 + \frac{1 + KK_p}{\tau}s + \frac{K_I K}{\tau}} \tag{4.3}$$

$$\omega_n = \sqrt{\frac{KK_I}{\tau}}, \xi = \frac{1 + KK_p}{2\sqrt{KK_I}\tau} \tag{4.4}$$

$$\tau_{loop}\omega_n = \frac{1}{\sqrt{1-\xi^2}}\left[\pi - \tan^{-1}\left(\frac{\sqrt{1-\xi^2}}{\xi}\right)\right] \tag{4.5}$$

Table 4.3: Summary of the parameters used to design the PI controller in the thermal control loop.

Parameter	value	Parameter	value
K	1	K_{f2V} (kHz/volt)	6.4
K_P	0.46	K_I (1/sec)	87
τ (sec)	~0.5	τ_{loop} (sec)	0.12

The control system was able to minimize the temperature variations to within ±10 μK while maintaining variations in the resonance frequency of the SAW resonator to below ±0.2 ppm as in Fig. 4.10. The variations are now limited by the $1/f$ noise mainly due to quadrature coupling of noise from drive to sense. In section 5.1.1, we demonstrated how the stability

of the frequency of the SAW will have a direct impact on the SAWG stability and drift minimization.

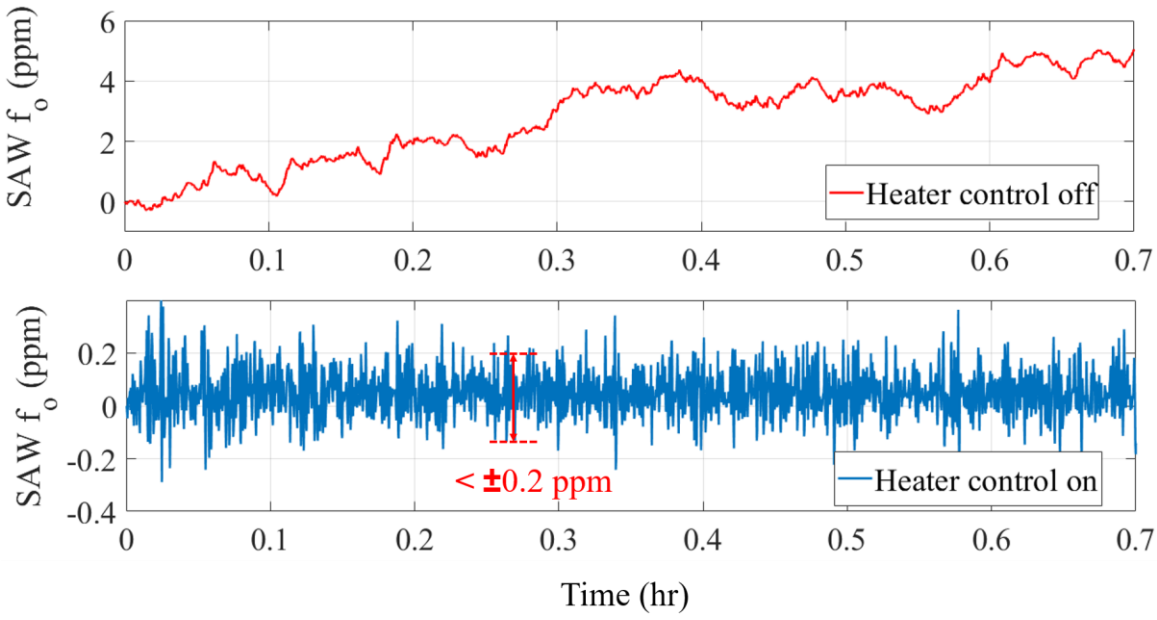

Figure 4.10: SAW resonance frequency versus time with (top) heater control off and (bottom) heater control on.

4.4. Integrated AOG

Using the integration method discussed in section 3.3, VCSEL and PDs were integrated on the AOG die. The PCB shown in Fig 4.11.a was designed to provide the biasing and connections for the VCSEL and PDs.

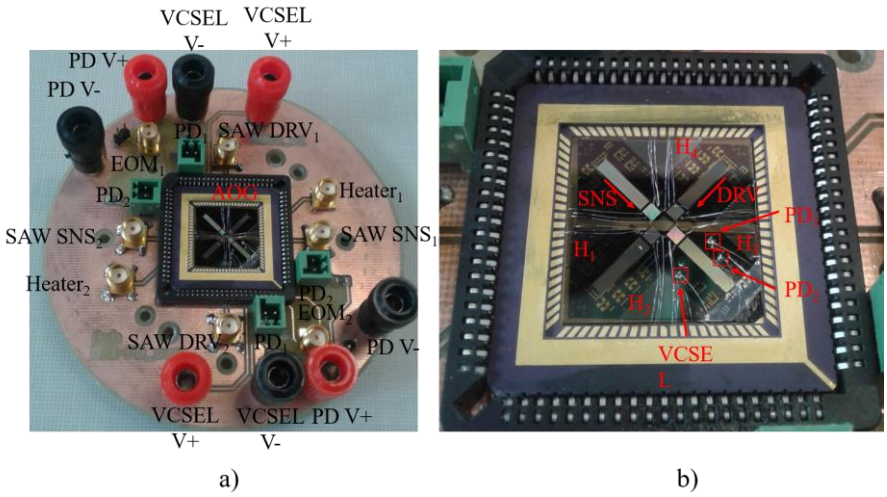

Figure 4.11: a) PCB of the integrated AOG showing the various component used while b) is the integrated AOG die showing the integrated VCSEL and PD.

The control system block diagram was modified with respect that of the discrete AOG (section 4.2.2) as shown in Fig. 4.12. The TIA is used to amplify the current of the PD and convert it to an output voltage. The circuit was designed to allow differential sensing.

To verify the functionality of the integrated devices (both laser and PD), an electro optic modulator (EOM) was first tested. The EOM was excited by the integrated laser. A modulation signal was applied to the EOM. The resulting output optical signal was detected by the integrated PD. The modulation gain of the EOM was monitored the setup and the measurement results of this experiment are shown in Fig. 4.13. These results demonstrated successful 3D integration of the laser and PD.

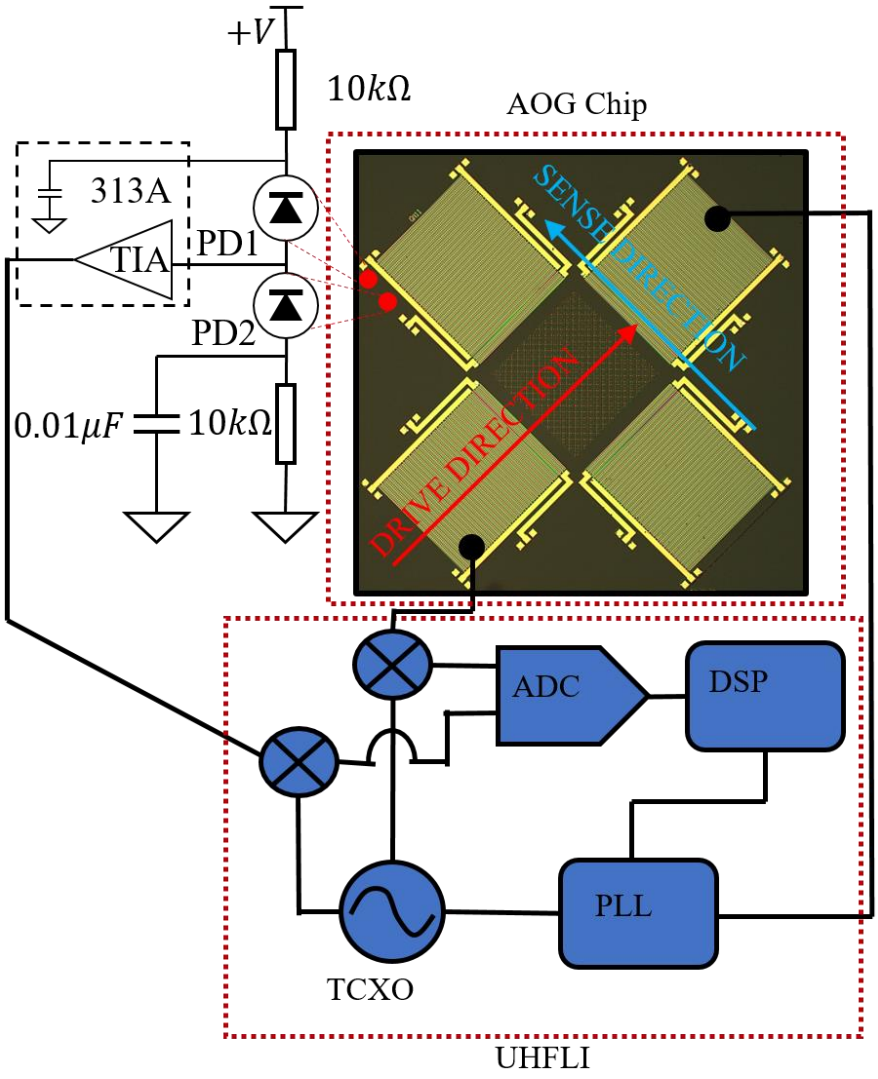

Figure 4.12: Open loop sensing control system of integrated AOG showing the drive control loop and the sense read-out.

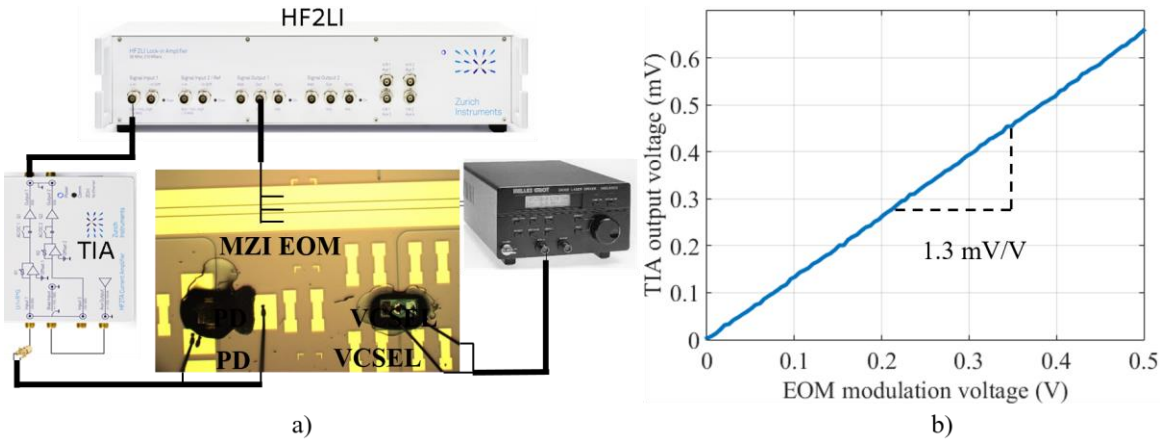

a) b)

Figure 4.13: Experimental setup for verifying successful integration of VCSEL and PD with LNOI photonic components. a) Test setup used to measure EOM response b) EOM test results confirming the expected EOM modulation gain and allowed the extract of optical IL due to VCSEL and PD integration (< 1 dB compared to VGA alignment for the same sample).

CHAPTER 5: Gyro Testing and Characterization

In this chapter, the characterization of SAWG and AOG is described. The test setups used to measure the SAWG and the AOG are described. The output data is analyzed to extract the sensitivity, noise performance and stability of the gyroscopes. Finally, the shock testing of the SAWG is presented. In this chapter, we present the characterization results of different versions of SAWG and AOG where the specifications of each are summarized in tables. 5.1 and 5.2.

Table 5.1: Specifications of the tested SAWGs

	1st SAWG		**Modified SAWG**
Fabrication process	**conventional**	**conventional**	**Self-aligned**
Read-out	Acoustic	Acoustic	Acoustic
Λ (μm)	30	30	30
Pillar thickness (nm)	144	280	600
L_A (Λ)	40	100	40
Dimensions (mm)	7.8x7.8	7.8x7.8	16x16

Table 5.2: Specifications of the tested AOGs

	1st AOG	**Modified AOG**	
Fabrication process	**conventional**	**Self-aligned**	**Self-aligned**
Read-out	MZI	MZI	RT
Λ (μm)	30	30	30
Pillar thickness (nm)	600	600	600
L_A (Λ)	40	40	80
Dimensions (mm)	20x20	16x16	16x16

5.1. Test setup

The test setup of a gyroscope comes with demanding requirements on its mechanical stability. Gyroscope's electrical connections are required to be functional under mechanical rotations and high centrifugal forces with high immunity to mechanical oscillations and

vibrations. In this section, we show our effort in building the testing Setup for SAWG and AOG testing. We discuss the challenges we faced and how to mitigate motivating test setup modification from discrete to integrated.

5.1.1. Discrete Setup

The schematic of the 1st setup built for SAWG / AOG measurements is shown in Fig. 5.1. The drive and sense signals of the SAWG (mounted on the rate table) are connected to the UHFLI, which is mounted on top of the elevated bread board. For the AOG, the difference from the SAWG is that the AOG sample is mounted on the rate table together with the optical positioners and connected to the measurement instruments. An optical carrier generated by a benchtop tunable laser (SANTEC TSL-510) is coupled into the optical grating via a vertical groove array (VGA). Polarization controller is used after the Laser to make sure that we excited the TE polarization for which the grating couplers were optimized. The same VGA is also used to couple out the modulated gyroscope signal through another set of fibers in the array.

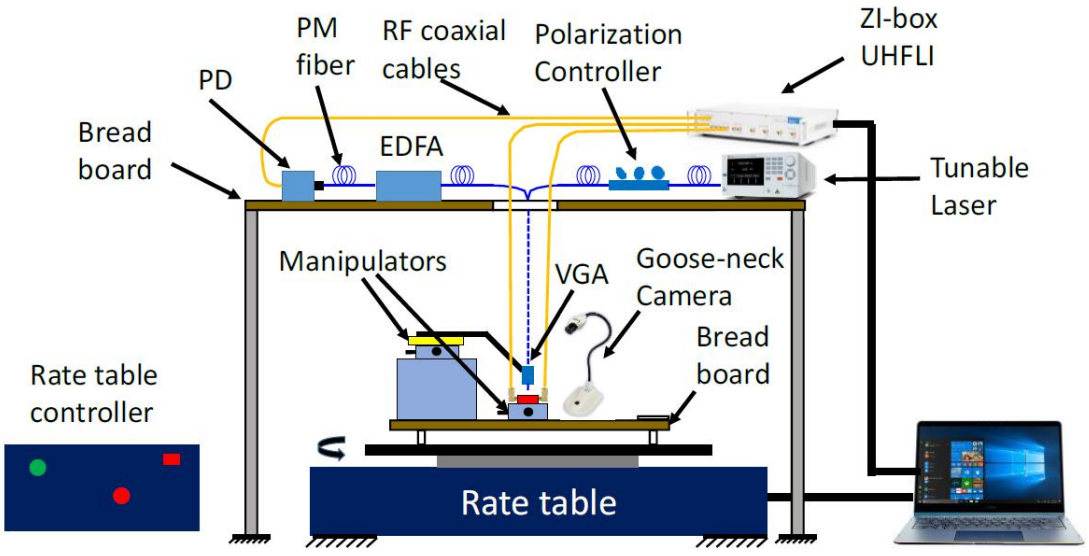

Figure 5.1: Schematic of the SAWG / AOG measurement setup. The optical setup with the positioners and manipulators are mounted on top of the rate table.

The optical alignment is optimized by adjusting a six degree of freedom manipulator and sweeping the laser wavelength. The same input rotation rates used for the SAWG are applied to the AOG. Fig. 5.2 shows the picture of the actual setup for the AOG testing. The dangling fibers restrict the max rotation angle of the rotation stage to avoid any induced stresses or potential for fiber damage. Even with limited rotation angle, the continuous oscillation of the rate table caused the VGA alignment to drift over time, which affected the characterized gyroscope stability. This drove the need for the development of an integrated AOG where the optical source and detectors are on the chip to eliminate all the fibers. It also motivated the development of an integrated test setup.

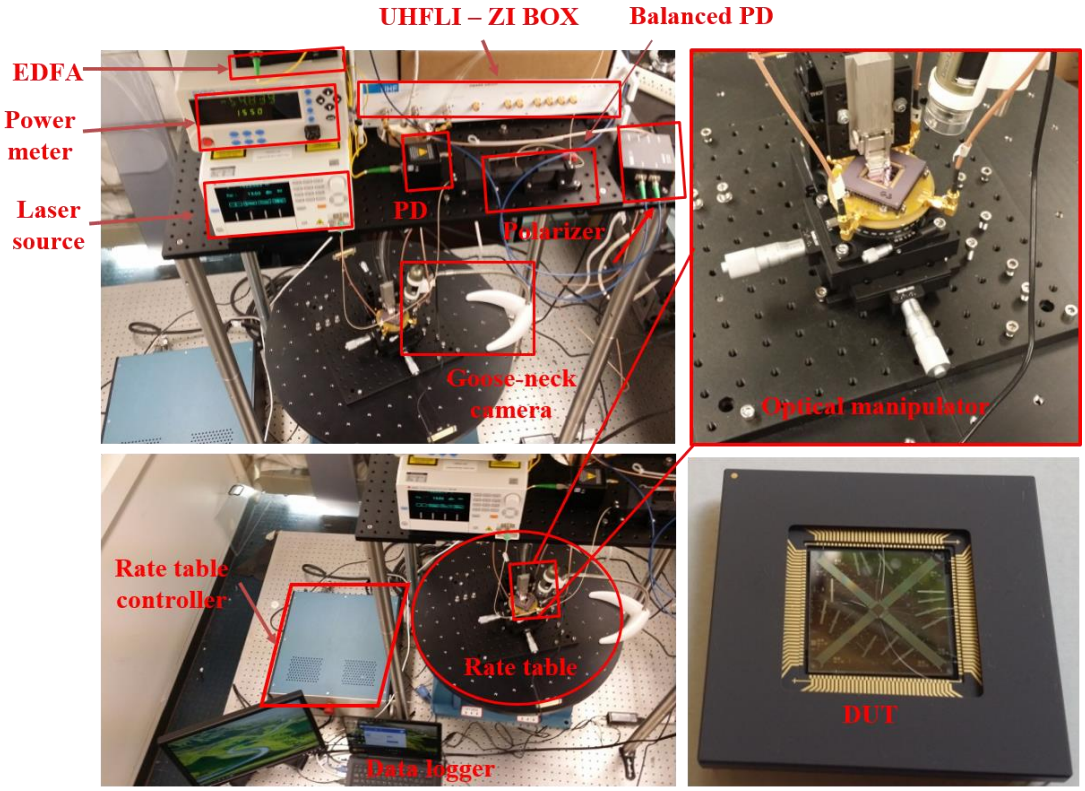

Figure 5.2: Discrete AOG setup showing all the components used for AOG testing.

5.1.2. Integrated Setup

Fig. 5.3 shows the integrated setup where all the testing components required for SAWG and AOG are mounted on the rate table. The UHFLI is fixed inside a frame designed to withstand high centrifugal forces where the screws are selected to hold under high shear

forces. The details of the mechanical deigns and solid modeling are presented in Appendix C. The setup is connected externally only to a power plug using a slip ring allowing both high rotation angle oscillations and full rotations. The setup was tested at the maximum rotation rate of the rate table 2000 $°/sec$ in full rotation for long durations where all the components were intact. With this setup, stress affecting the RF shielded cables connecting the drive signal and the sense signal of the SAWG are eliminated. In addition, all bulky components needed for integrated AOG testing such as the VCSEL driver and TIA where replaced with light weight components such as Thorlabs VSCEL driver and 313A TIA [58].

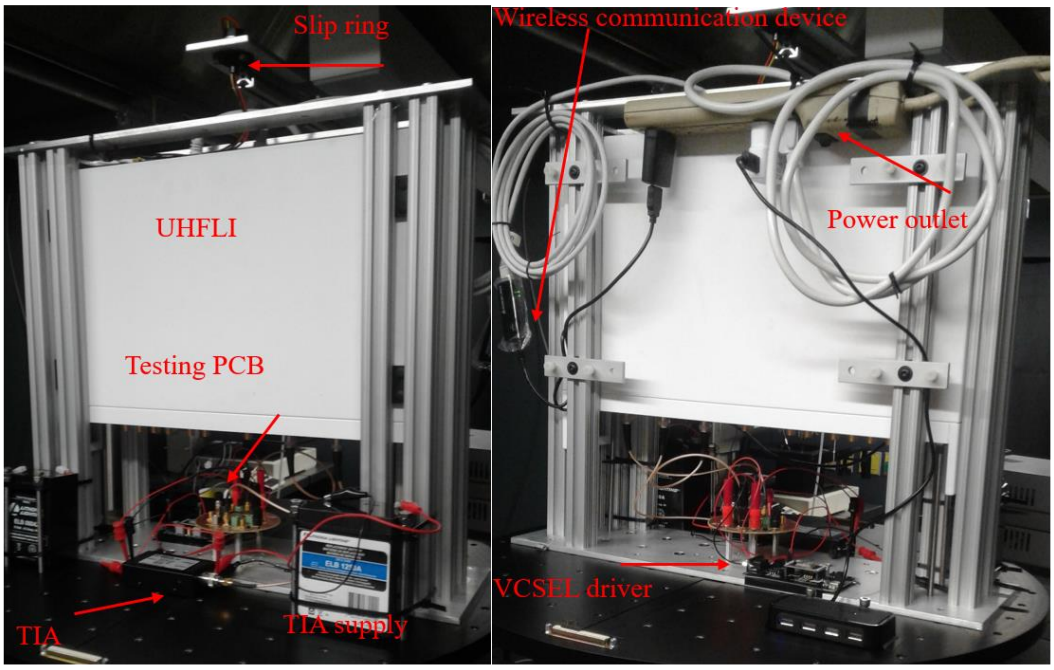

Figure 5.3: Integrated setup showing the various components used in the characterization of the SAWG and integrated AOG without the need for external connections for signals or sources.

5.2. Gyroscope Sensitivity and Stability

In this section, we show how the theoretical analysis presented in section 2.1.2 shows a close agreement to the measured values and the proposed trends to enhance the performance of the SAWG and the AOG. The first step of testing a gyroscope involves extracting the relation between the input rotation rate ($°/sec$) and the sensing system's

output voltage (V). This value is commonly referred to as scale factor (SF). For both SAWG and AOG, the SF is represented in $V/°/sec$ since the final gyro signal given to the UHFLI front-end is voltage. The SF alone is not representative of a gyroscope performance. Its value is meaningful only when compared to the noise level. The signal to noise ratio (SNR) is a better figure of merit to evaluate gyroscope performance. The higher the SNR, the better the gyroscope.

Gyroscope noise behavior is described in [59]. The four common sources of noise are: ARW, which represents the white noise in the frequency domain; bias instability, which represents the $1/f$ or flicker noise; rate random walk (RRW) and drift which represent $1/f^2$ noise; and rate ramp drift which represents $1/f^3$ noise. One of the standard methods to study noise in gyroscopes is using Allan deviation (ADEV) log-log plot as shown in Fig. 5.4, which represents the output signal variability after referring to the input at various integration times. If the noise sources are statistically independent, then the computed Allan variance is a sum of the squares of each error as given in (Eq. 5.1) where σ_{ARW}^2, $\sigma_b^2(\tau)$, $\sigma_{RRW}^2(\tau)$, $\sigma_d^2(\tau)$ are the noise power for ARW, bias instability, RRW, and rate ramp drift.

$$\sigma_{total}^2(\tau) = \sigma_{ARW}^2(\tau) + \sigma_b^2(\tau) + \sigma_{RRW}^2(\tau) + \sigma_d^2(\tau) \quad (5.1)$$

To characterize the noise of a gyroscope, the zero rate output (ZRO) of the gyroscope, which is the output signal of the gyro at no input rotation rate, is recorded. The ADEV of the ZRO is then computed and normalized to the SF to derive meaningful gyroscope noise parameters. The ARW asymptote has a $slope = -1/2$ where the ARW is the y-axis value of the asymptote at $\tau = 1$. The bias instability asymptote is parallel to the x-axis where the bias instability is extracted from the asymptote intersection with the y-axis divided by 0.664 [59]. The RRW asymptote has a $slope = 1/2$ where the RRW is the y-axis value of the asymptote at $\tau = 3$.

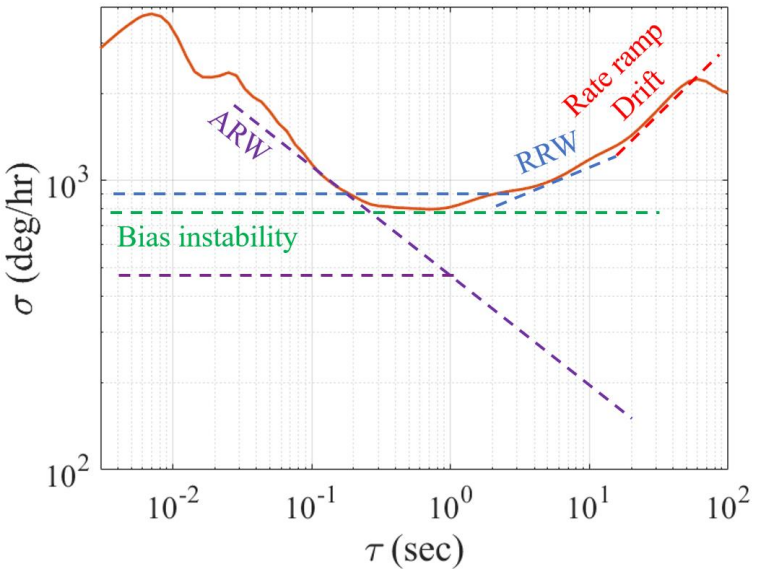

Figure 5.4: Example of ADEV plot showing the asymptotes corresponding to different noise types.

5.2.1. SAWG Testing

The first version of the SAWG was used to verify the propor55.2tionality of SF to the pillar mass, m_p ,and the resulting performance enhancement. The design parameters of the gyroscopes are summarized in table 5.3.

Table 5.3: Summary of the main design parameters for the investigated gyroscopes, SAWGA and SAWGB.

Parameter	SAWG A	SAWG B	unit
Λ	30	30	μm
L_A	44	100	In Λ
N_{pair} IDT	23	13	
Mass thickness (t_m)	140	282	nm
Resonance frequency	116.31	115.17	MHz
Input impedance	66	89	Ω
Power	9.8	9.2	mW
Quality factor	~1000	~1000	

The devices were fabricated using the conventional SAWG process explained in section 3.1. The total mass of the pillars, m_p, was increased by changing the number of pillars and

the thickness of the pillars. To change the number of pillars, two versions of SAWG where built, SAWGA and SAWGB (shown in Fig. 5.5), where $L_{A_B} = 2L_{A_A}$ and $\frac{N_{p_B}}{N_{p_A}} = \left(\frac{L_{A_B}}{L_{A_A}}\right)^2$.

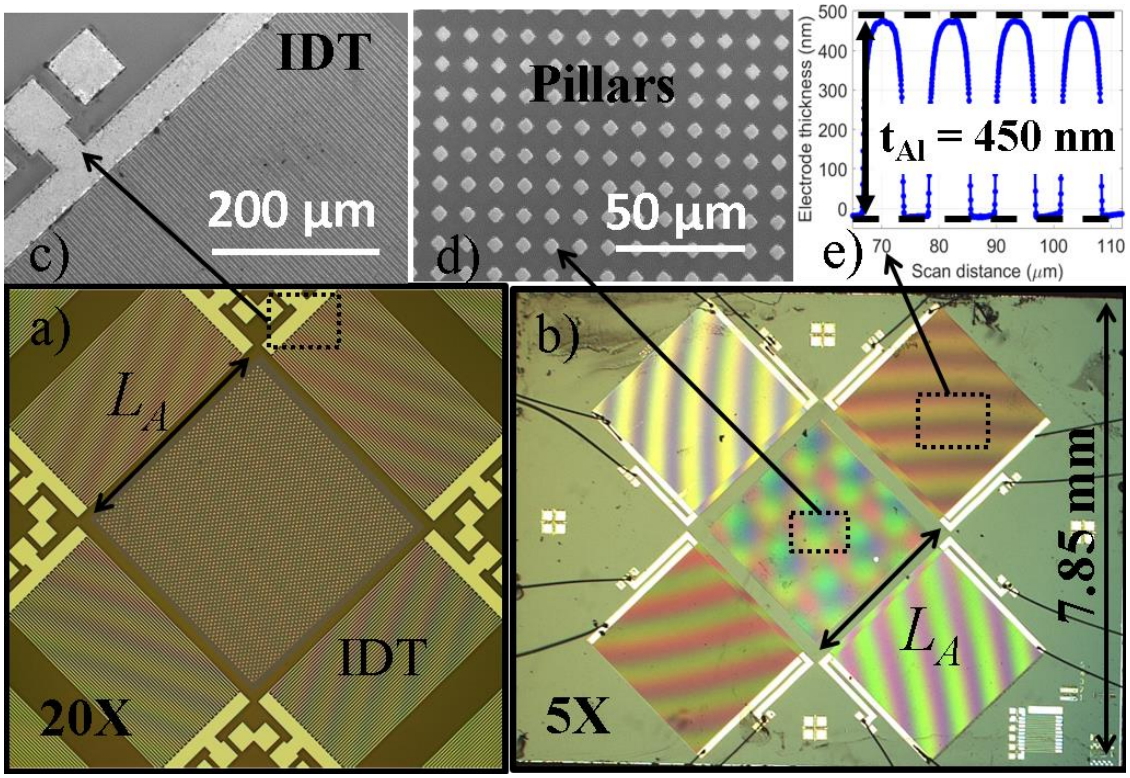

Figure 5.5: Microscope images of the SAWGs with zoomed-in SEMs of the various components forming it: a) and b) are the fabricated SAWGs with different cavity type (A and B), c) SEM of routing electrodes and IDT, d) SEM of the gold pillars and e) a profilometer scan of the electrode and reflector film thickness.

The gyro output vs rotation rate shown in Fig 5.6. was measured for both SAWG A and B using the discrete test setup described in section 5.1.1. By applying a 2Hz mechanical oscillation using the rate table and sweeping the amplitude from 0.5 to 8 degrees, the gyroscope was subjected to a yaw rotation rate Ω_z ranging from 6 to 100 $°/sec$. The SF was extracted by linear fitting of the measured data where $SF = slope$. The SF shows some nonlinearity, which is likely due to the vibrations induced by the RG316 DS 24-inch flexible RF SMA cables used in the discrete setup. For noise measurements, the ZRO of the two SAWGs was recorded for 4 hours. The ADEV plot shown in Fig. 5.6 was calculated from the ZRO of SAWGs A and B.

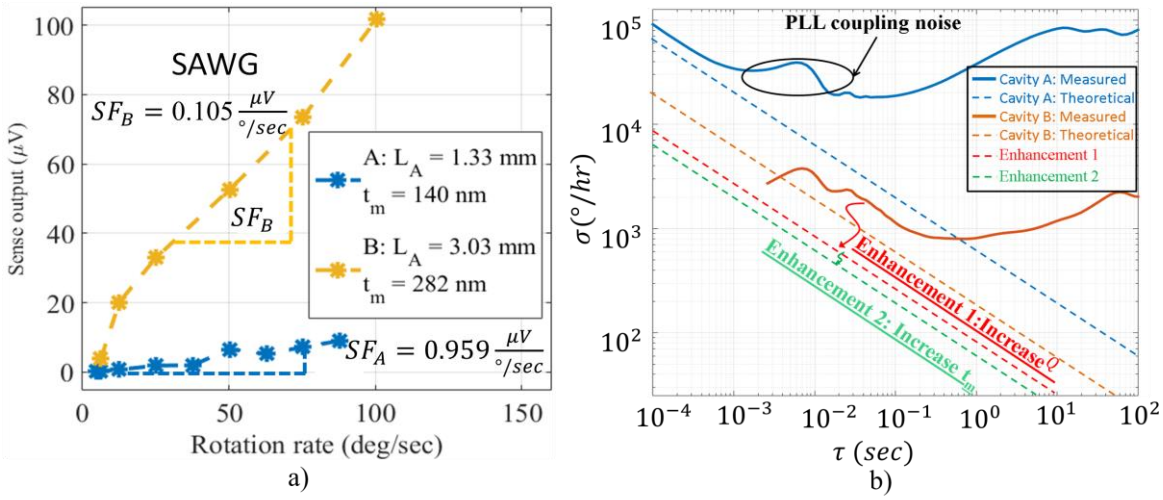

Figure 5.6: Measurements of the 1st SAWG prototype with two cavity size variants where a) show the measurements used to extract the SF while b) shows the ADEV curve for ZRO of the two SAWGs.

The measured values of SF and ARW are summarized in table 5.4. These measurements are the first to quantify the SAWG performance. The ratio between the SFs of SAWGs A and B agrees with the theoretically expected ratio due to scaling of the Coriolis mass by changing the pillar thickness and the number of pillars. It is obvious that an increase in sensitivity by increasing the Coriolis mass reduced the ARW and bias instability of Cavity B. The ARW extracted from the measured data is slightly larger than the theoretically expected value due to the noise added by the UHFLI instrument that was used to take the measurements. Due to the higher quadrature signal in SAWG B, the UHFLI input amplifier had to be set to a different range value compared to SAWG A, which resulted in additional noise from the measurement instrument. This setting of the UHFLI for SAWG B explains why the difference between the measured and theoretically predicted ARW for SAWG B is higher than that measured for SAWG A. This study also shows how further enhancements in the noise performance are possible through improvements in Q and by increasing the metal thickness, t_m.

Table 5.4: Summary of the theoretically calculated and measured performances of the investigated gyroscopes.

Parameter	SAWG A	SAWG B	unit
SF	0.105	0.959	$\mu V/°/sec$
ARW (theoretical)	10.51	3.35	$°/\sqrt{hr}$
ARW (measured)	14.85	5.95	$°/\sqrt{hr}$

A second version of the SAWG was fabricated using the self-aligned process discussed in section 3.1.2. The advancements in this process enabled us to increase the quality factor by 3 × and the pillar thickness by 4 ×. In addition, the high power handling of W enabled us to verify the power dependence relations of the SAWG.

For this sample, the SF nonlinearity was studied as shown in Fig. 5.7 by measuring the sample using both the discrete and integrated test setups described in section 5.1. In the measurements of the integrated setup, each input rotation rate was measured 5 times. The mean and the standard deviation (STD) error were calculated and plotted. The STD is not only due to the gyro or front-end noise but also includes the rate-table noise, which is operated at low accuracy mode to get higher rate-table oscillation bandwidth.

From the measurements in Fig. 5.7.a it is clear that the effect of the cables dominated the nonlinearity in the discrete setup. These nonlinearities are almost completely eliminated by the integrated setup. The SF was extracted for each setup, with the integrated setup exhibiting a lower SF by only 12%. This analysis verifies that the SF values extracted from the discrete setup in the previous demonstrations are reliable to be used in ZRO normalization and initial noise calculations. In addition, the scale factor nonlinearity (SFNL) calculations were performed as shown in Fig. 5.7.b using (Eq. 5.2) which is derived based on differential nonlinearity. Although the SFNL seems high (more than 1%), the setup noise (σ_{setup}) to fitting error ($e_{fit} = |V_{out-measured} - V_{out-fit|}$) ratio shows that σ_{setup} is dominant for almost input rotation rates except the last two points. In practical

implementation to eliminate the effect of nonlinearity, a real time linearization model is implemented either by fitting or lookup table

$$\text{SFNL}=\frac{1}{N}\frac{\sum_{i=1}^{N}\left|\frac{dV_i}{d\Omega_i}-SF_{fit}\right|}{SF_{fit}} \tag{5.2}$$

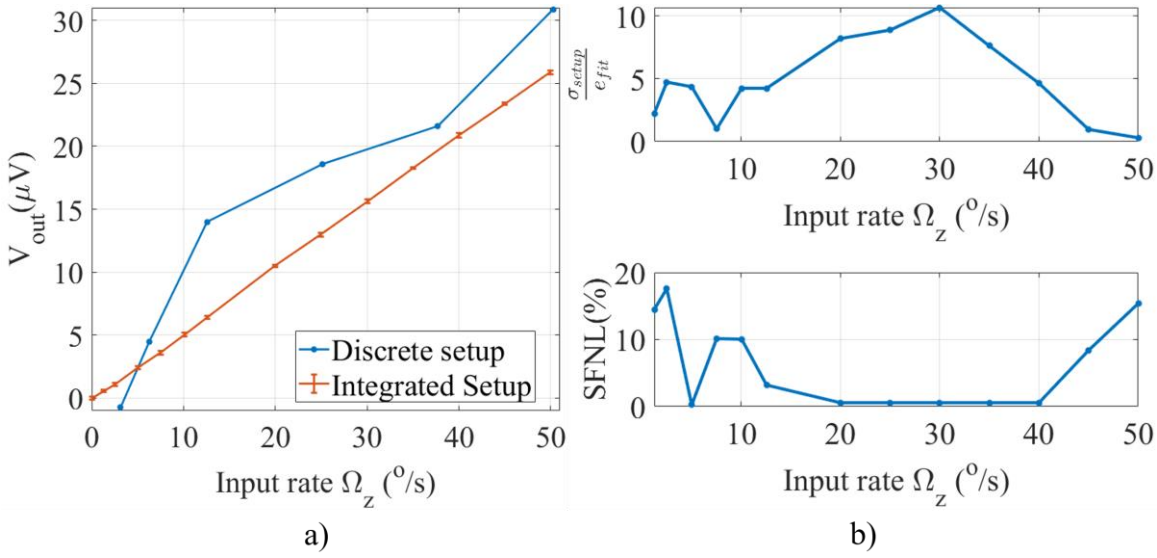

Figure 5.7: Study of SFNL of SAWG using the discrete and integrated testing setups where a) shows the SAWG output voltage vs rotation rate while b) shows the integrated setup NL measurements such noise to NL error ratio and SFNL in percentage.

The ADEV plot shown in Figure 5.8 demonstrates the reduction in ARW and bias instability while the measured values are presented in table 5.5.

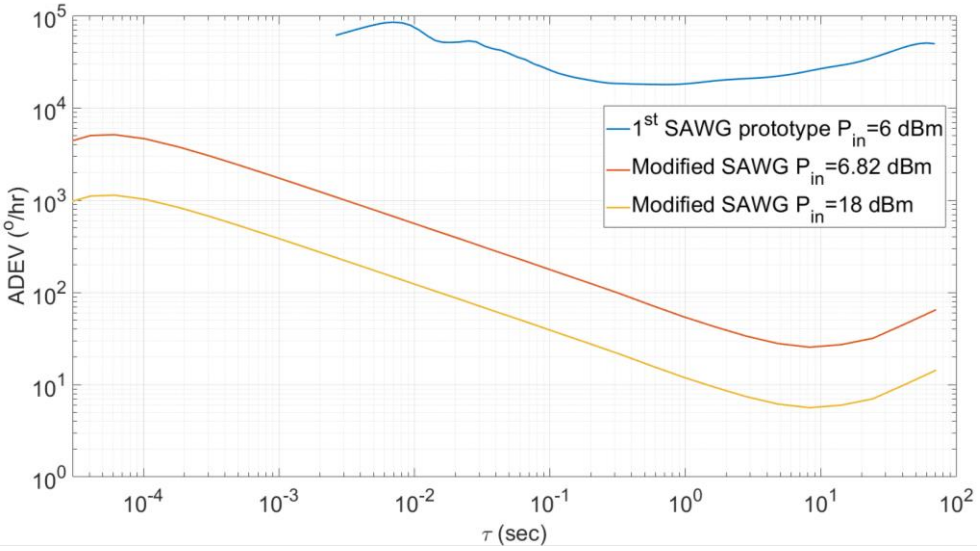

Figure 5.8: ADEV plot of SAWG using conventional and modified self-aligned process at different input powers. All SAWG have the same Λ and L_A .

Table 5.5: Summary of ARW and bias instability measured for SAWG using conventional and modified self-aligned process.

SAWG	ARW ($°/\sqrt{hr}$)	Bias instability ($°/hr$)
Conventional ($P_{in} = 6.82\ dBm$)	14.85	27,075
Modified ($P_{in} = 6.82\ dBm$)	1.15	37.6
Modified ($P_{in} = 18\ dBm$)	0.254	8.3

These demonstrations show that the SAWG is capable of achieving tactical grade performance [59], making it a competitive approach on part to other gyroscope solutions. After the minimization of the ARW and bias instability, we focused on investigating what impacted the RRW and drift of the SAWG. In many cases, the RRW and drift mask the actual bias instability making it difficult to even extract an accurate value of the bias instability. The reduction of RRW and drift can help in achieving longer stability, which was the motive behind the development of the thermal control system discussed in section 4.3. Fig. 5.9 shows that ADEV plot of the 2nd version of modified SAWG operating under various configurations with and without the heater operation and the control loop.

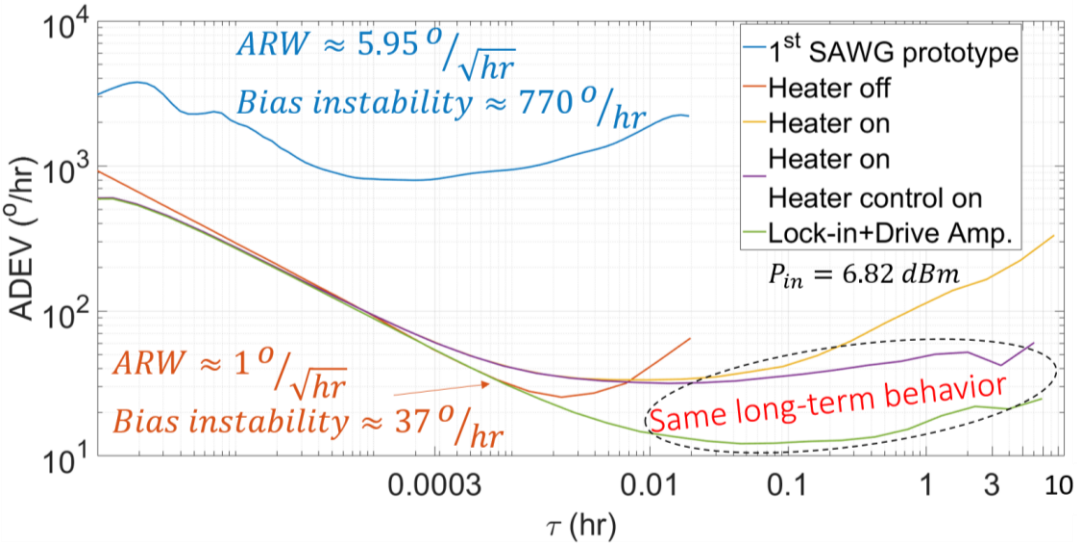

Figure 5.9: Allen deviation plot for the SAWG under various conditions and for the testing setup (Lock-in + drive Amp.) without the SAWG. The ARW (equivalent thermal noise) of the setup was scaled by 55x to match that of the SAWG to clarify the difference in the long-term stability region.

In addition, the ADEV of the standalone UHFLI lock-in amplifier is also inserted to shows that the drift of the SAWG is now limited by the drift of the ovenized crystal in the UHFLI. Focusing on the long-term stability, 24 hours of data were extracted for the various testing cases. The ovenized thermal control system showed the highest long-term stability with bias instability point at τ > 100 sec and Rate Random walk (RRW) of 5 milli deg/s/√Hz. The long-term stability of the SAWG is mostly limited by the stability of the ovenized crystal in the measuring instrument.

5.2.2. AOG Testing

Coupling of quadrature signal from drive to sense either electrically or by pillar scattering is one of the major challenges in the SAWG. It can desensitize the front-end electronics. Even if this was solved by using a wide dynamic range front-end or by the development of quadrature cancelation loops, noise coupling from the drive loop to the sense read-out would still remain a major challenge. The noise from the quadrature signal would directly appear in the ZRO leading to an increase in ARW and bias instability.

The AOG was able to mitigate quadrature coupling as reflected in all its measurements and demonstrations. The optical sensing is physically decoupled from the acoustic driving, which drastically minimized quadrature and had a direct impact on the gyroscope's stability enhancement. In this section, we present how different design parameters and read-out methods impact the performance of the AOG

The 1st AOG prototype was fabricated using the conventional SAWG process with a monolithically integrating MZI photonic structure. As shown in Fig. 5.10, the senor showed better stability compared to the 1st SAWG prototype due to the quadrature decoupling.

A modified AOG version was fabricated using the modified self-aligned process. The optical losses were addressed as discussed in section 3.2. The waveguide losses were reduced to $\sim 0.18\ dB/cm$ while the grating loss minimized to $\sim 12\ dB$, resulting in a total

loss of ~ 30 dB. Given these improvements, the modified AOG showed better noise performance, lower ARW and higher stability compared to the 1st AOG. In addition, the two optical read-out systems discussed in section 4.2.2 were used in the modified AOG measurements as in Fig. 5.11.

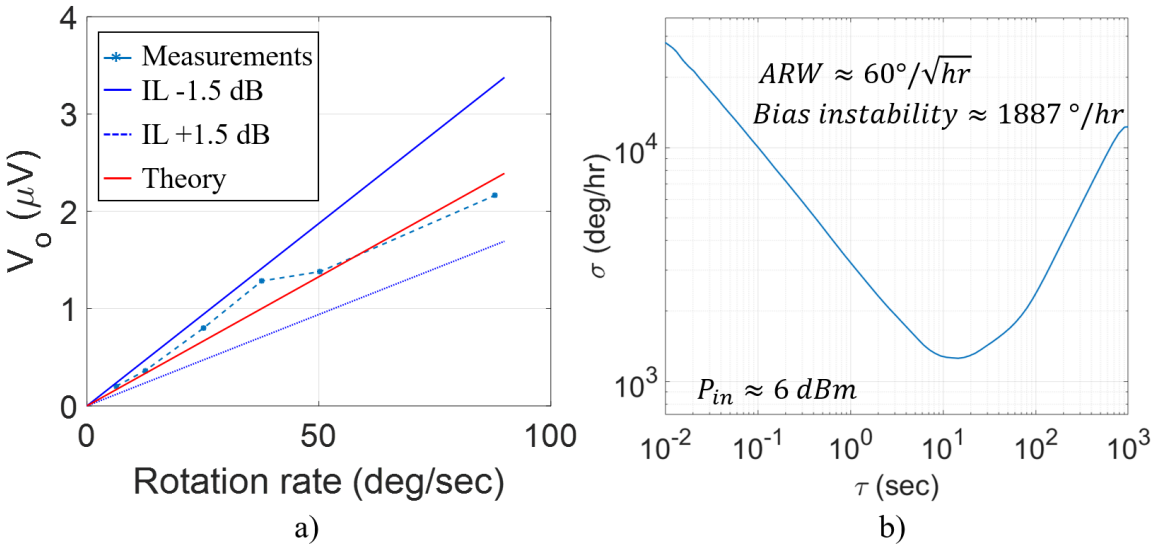

Figure 5.10: Gyro measurement of the 1st AOG where a) is the SF showing the expected variations in SF due to VGA misalignment causing optical insertion loss (IL) of $\pm 1.5\ dB$ while b) is the ADEV curve.

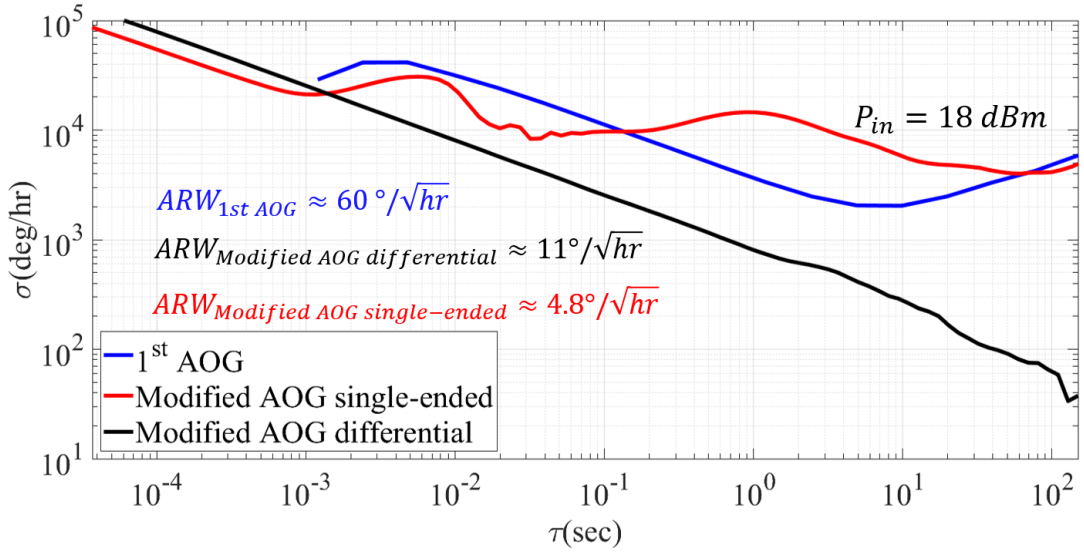

Figure 5.11: Measured Allan deviation for the ZRO of the 1st prototype and modified AOG using single-ended and differential read-out systems.

The differential system showed better stability and ability to reject common mode noise and variations compared to the single ended system. The differential modified AOG

achieved $\tau_{stability} > 300\ sec$ where the bias instability point was not reached during this measurement. However, the single-ended system was able to provide higher gain achieving lower ARW of ~4.8 $°/\sqrt{hr}$ compared to ~11 $°/\sqrt{hr}$ for the differential system at P_{in}=18 dBm.

The continuous effort toward the minimization of ARW motivated some modifications in the photonic devices. As discussed in section 2.1.3, an AOG with RT photonic structure was designed and fabricated. It has a great advantage over MZI due to its ability to increase the sensitivity using optical field enhancement, which is proportional to the finesse of photonic RT resonator. The photonic resonator achieved a quality factor of $\sim 95k$ resulting in high finesse and amplification factor of $\sim \times 2.15$ with respect to the single ended MZI read-out technique tested previously for the modified AOG. In addition, a bigger cavity was used to compare the AOG with MZI, $L_{A_{RT}} = 2L_{A_{MZI}}$ and $\frac{N_{p_{RT}}}{N_{p_{MZI}}} = \left(\frac{L_{A_{RT}}}{L_{A_{MZI}}}\right)^2$. From the ADEV plot shown in the Fig. 5.12, the AOG with RT was able to achieve $ARW = 0.55\ °/\sqrt{hr}$ which is about ~9 × reduction in ARW.

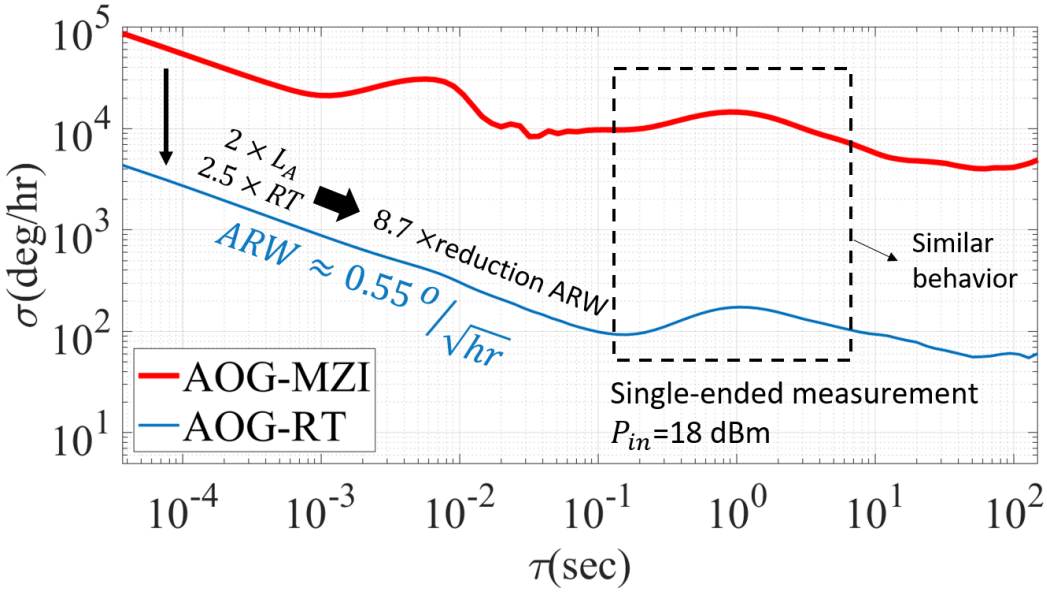

Figure 5.12: ADEV plot of AOG with MZI and RT showing the enhancements due to cavity size scaling and optical field enhancement in the RT and the similarity in their long-term stability behavior due to the nature of measurement system (single-ended).

Using single-ended read-out system, The RT AOG was not able to reject common mode variations. It was also noticed how the single-ended measurements of the AOG using both MZI and RT follow similar behavior in the long-term stability region. However, unlike the MZI, the ADEV of the RT does not show 60 Hz noise due to proper AC grounding and shielding techniques considered.

5.3. **Shock Testing**

To validate the proposed high-G survivability of the SAWG and AOG, SAW resonators built on the same LN substrates used for the synthesis of the SAWG and AOG were subjected to high-G testing. Their electrical response was tested before and after the shock test and compared. The high G-shock testing was performed using Hopkinson bar test setup shown in Fig. 5.12 The maximum shock applied was around 7 kG [59].

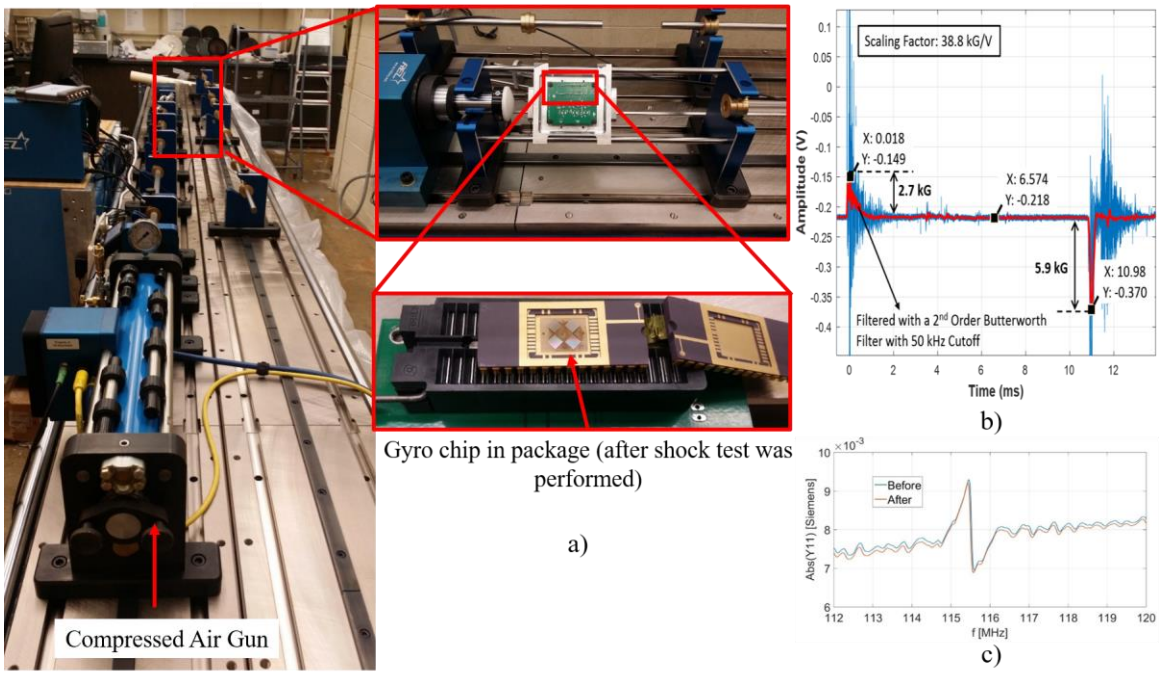

Figure 5.13: Shock testing setup and results where a) shows the structure of the Hopkinson bar setup and the way the sample is mounted, b) shows the +/- G applied due to the shock while c) shows the acoustic response |Y11| of the SAWG before and after the shock.

A slight difference was noticed in the Y_{11} measurements as shown in Fig. 5.12. The measurements of the response was repeated few times after the shock where the variations

were found to be within the noise level of the VNA used. In addition to the previous test, a new set of samples were also subjected to high-G shock testing at the Army Research Laboratory (ARL). All the samples in this set survived all the applied shocks from 10 kG to 50 kG which was verified by visual inspection only.

CHAPTER 6: CONCLUSIONS AND FUTURE WORK

6.1. Conclusion

The increasing demand for high performance INS has influenced technological innovations in gyroscopes. Many industries especially aviation and automotive are driving new technologies motivated by new autonomous, positioning, navigation applications. In this regard, this thesis introduced a new type of gyroscope called the acousto-optic gyroscope (AOG), which has a huge potential to overcome the challenges for navigation grade performance and meet the specifications of emerging applications.

As presented in chapter 2, the study of the AOG showed its ability to achieve tactical and navigation grade performance by scaling the device size, mass of pillars, electrical power and enhancement of the quality factor. The building blocks of both acoustics and photonics were designed and optimized to ultimately achieve the target AOG navigation grade performance. Specifically, LN with various cuts and directions were studied targeting orthogonal symmetry SAW propagation directions with high K_t^2 leading to the choice of Y-cut LN $\pm 45°$ relative to Z-direction. Reflector gratings were optimized to achieve high reflectivity per finger (2.89%) by the development of new grating structure combining both MA and GA gratings leading to the reduction of radiation loss. The different loss mechanisms impacting the quality factors were studied in details. Design techniques and new resonator structures were developed such as skewing, aperture widening and QARP which boosted the quality factor from ~1000 using conventional designs to 14,000.

All the previously described demonstrations would not be feasible without substantial modifications in the fabrication techniques. The fabrication flow for the various generations of devices was developed in-house. As described in chapter 3, a modified SAW process was developed to achieve self-alignment and minimize frequency mismatch due to

fabrication misalignment and tolerance errors. It was demonstrated that the pillar-electrode misalignment went down from being mask alignment limited ($> 0.5\ \mu m$) to mask feature limited (> 50 nm) with at least$10\times$ reduction in frequency mismatch using just low cost commercial mask technology [60]. The adoption of 1st layer alignment procedure lead to the minimization of frequency mismatch from 350 ppm to 44 ppm limited by wafer cut error. New pillars structure was developed by groove etching the LN substrate leading to the reduction of quadrature due to pillar scattering by 15 dB compared to that with regular metal pillar. Instead of W etching, a lift-off process of thick W film was developed to avoid the contamination of photonic devices. In this case, 3.2 μm and 6 μm of W were successfully lifted off. The packaging of SAWG/AOG and die bonding of VCSEL and PD on AOG were also demonstrated. Chapter 3 enucleated the challenges encountered in this 3D integration process and discussed how a solid approach was identified.

Control systems for SAWG and AOG were described in Chapter 4 where an open loop gyroscope sensing system was presented. A micro-oven was built using monolithically integrated heaters and SAW frequency thermometer. A thermal control loop was developed to control the micro-oven. The loop was developed to investigate the drift in SAWG. It was able to control the temperature and frequency variations to within $\pm 10\mu K$ and $\pm 0.2\ ppm$. The frequency fluctuations were limited by flicker noise. As shown by the ADEV curve, the measurements with the thermal control loop exhibited the smallest drift compared to the same response without the thermal loop. It was demonstrated that the drift became limited by the frequency drift in the crystal of the measuring instrument. In addition, a prototype of functional VCSEL and PD integration was demonstrated.

Three different samples of both SAWG and AOG were characterized. Those characterizations represent the 1st demonstration of functional SAWGs and AOGs. Using the SAWG samples, it was demonstrated how the increase in pillar thickness by $\sim 2\times$ and

cavity size by ~2.5 × can lead to the reduction of the ARW from 14.85 to 5.95°/$\sqrt{hr}$. It was also demonstrated how the modified SAWG process resulted in acoustic quality factor enhancement by 3×. Simliarly, the pillar thickness increase by 4× lead to the reduction of ARW from 14.85 to 1.15 °/$\sqrt{hr}$. In addition, it was shown that the quality factor of the SAWG has a direct impact on the bias instability (32 × reduction) and $\tau_{stability}$ (increased by more than one order of magnitude). The increase in driving power of the SAWG by 13× lead to the reduction of ARW from 14.85 to 1.15 °/$\sqrt{hr}$.

The AOG showed its advantage over the SAWG in terms of stability due to its ability to physically decouple the acoustic drive and optical sense mechanisms. The modified AOG with MZI was able to show $\tau_{stability} > 300$ sec without reaching the bias instability point. The differential measurements of the AOG showed its ability to reject common mode noise and variations compared to the single ended configuration. In addition, the ability of the RT to increase the output sensitivity by the optical field enhancement and reducing ARW was demonstrated. Compared to the AOG with MZI, the 2.15 × due to field enhancement in addition to 2 × in cavity size lead to the reduction of ARW from 4.8 to 0.55 °/$\sqrt{hr}$. In addition, the ability of the SAWG to survive high shocks was demonstrated. Two test sets were performed where the first was executed at CMU using a Hopkinson bar shock setup and electrically characterizing the sample before and after applying high G-shock at 7kG. The electrical characterization of the acoustic performance showed negligible difference meaning that run-to-run variations were kept to a minimum. The second set of gyroscopes was tested at ARL by applying high G-shocks on 5 different samples from 10 to 50 kG. All samples passed the visual inspection test.

The AOG showed outstanding performance in terms of stability and shock survivability. The ARW of the AOG was reduced by 109× compared to the 1st AOG prototype while that of the SAWG was reduced by 58.5 × compared to the 1st SAWG prototype. These

demonstrations show that both the AOG and SAWG are capable of achieving tactical grade performance. Further investigations are required in order to achieve navigation grade performance.

6.2. Future Work

One important parameter than needs to be exploited is the scalability of Λ. It was shown in the parametric study that Λ scaling between $150\mu m$ to $200\mu m$ can achieve navigation grade performance within the allowed form factor limitations. Although it sounds straight forward, many limitations are expected. The first is that the 500 μm thickness of a 4 inch wafer became comparable to the SAW penetration depth, which might affect SAW operation and acoustic losses. In addition, the sample handling represents a huge issue. With a $\sim 40 \times 40$ mm die, custom packaging is the only solution since it is not easy to find commercial ceramic packages of this size. The package design needs to consider the stress effect induced on the sample, which exponentially increases with die dimensions.

Another direction to pursue is the modification of RT photonic structures and processes. With the adoption of a photonic process capable of achieving low optical loss as the one reported in [30], two orders of magnitude enhancement in sensitivity are expected. In addition, an MZI-RT combined structure as the one proposed in [30] could be adopted in order to achieve differentiability and reject common mode noise, hence increasing AOG overall stability.

A long term plan to enhance the AOG performance is to explore different materials with higher acoustic and optic coefficients. One of the best candidates is using As_2S_3 which was proven to have 3X higher acousto-optic coefficient than that of LN. This can lead to $4\times$ improvement in the AOG sensitivity. Another revolutionary material is Sm-doped $PbTiO_3$ single crystal [61]. Initial study of its properties showed enormous piezoelectric coefficients several orders of magnitude higher than that of LN. If such material was

adopted, this can increase the oscillation amplitude of the pillars and ultimately enhance the sensitivity and reduce ARW.

For quadrature minimization due to pillar scattering, a LN deep trench etching process is required to realize groove etched pillars to replace metal pillars. This modification will have a direct impact on the reduction of quadrature, coupled noise and ultimately improves the noise and stability of the AOG.

APPENDIX A: Bond's transformations

This method is used to rotate non-square matrices such as the piezoelectric coupling ones (called d,e, g or h) to obtain the correct material parameters for a selected orientation. Since the stress form charge of the piezoelectric equation is considered, we are specifically interested in the e matrix. This method can also be used to rotate the squared matrix of the dielectric permittivity ϵ and the stiffness c. Elements of $[c]$ are in [GPa] while the one in the e matrix are expressed in [Cm-2]. Elements of $[\epsilon]$ are dimensional because normalized on ϵ_o. The Euler rotation matrices a_i where $i = x, y, z$ needed to be used to retrieve the final rotational matrix M. These 3x3 matrices implement a rotation of a generic angle θ around one of the principal axis x, y, z. Rotations are positive when counterclockwise respect to the axis with the right-hand convention.

$$a_x = \begin{bmatrix} 1 & 0 & 0 \\ 0 & \cos(\theta) & \sin(\theta) \\ 0 & -\sin(\theta) & \cos(\theta) \end{bmatrix} a_y = \begin{bmatrix} \cos(\theta) & 0 & -\sin(\theta) \\ 0 & 1 & 0 \\ \sin(\theta) & 0 & \cos(\theta) \end{bmatrix}$$

$$a_z = \begin{bmatrix} 1 & 0 & 0 \\ 0 & \cos(\theta) & \sin(\theta) \\ 0 & -\sin(\theta) & \cos(\theta) \end{bmatrix}$$

Once these matrices are specified according to the Bond's method the correct evaluation the material parameters can be realized building the rotation matrix M_i as described in []. In the following is reported the final results for M_x, M_y, M_z:

$$\begin{bmatrix} 1 & 0 & 0 & 0 & 0 & 0 \\ 0 & \cos^2(\theta) & \sin^2(\theta) & \sin(2\theta) & 0 & 0 \\ 0 & \sin^2(\theta) & \cos^2(\theta) & -\sin(2\theta) & 0 & 0 \\ 0 & -\sin(2\theta)/2 & \sin(2\theta)/2 & \cos(2\theta) & 0 & 0 \\ 0 & 0 & 0 & 0 & \cos(\theta) & -\sin(\theta) \\ 0 & 0 & 0 & 0 & \sin(\theta) & \cos(\theta) \end{bmatrix}$$

$$\begin{bmatrix} \cos^2(\theta) & 0 & \sin^2(\theta) & 0 & -\sin(2\theta) & 0 \\ 0 & 1 & 0 & 0 & 0 & 0 \\ \sin^2(\theta) & 0 & \cos^2(\theta) & 0 & \sin(2\theta) & 0 \\ 0 & 0 & 0 & \cos(\theta) & 0 & \sin(\theta) \\ \sin(2\theta)/2 & 0 & -\sin(2\theta)/2 & 0 & \cos(2\theta) & 0 \\ 0 & 0 & 0 & -\sin(\theta) & 0 & \cos(\theta) \end{bmatrix}$$

$$\begin{bmatrix} \cos^2(\theta) & \sin^2(\theta) & 0 & 0 & 0 & \sin(2\theta) \\ \sin^2(\theta) & \cos^2(\theta) & 0 & 0 & 0 & -\sin(2\theta) \\ 0 & 0 & 1 & 0 & 0 & 0 \\ 0 & 0 & 0 & \cos(\theta) & -\sin(\theta) & 0 \\ 0 & 0 & 0 & \sin(\theta) & \cos(\theta) & 0 \\ -\sin(2\theta)/2 & -\sin(2\theta)/2 & 0 & 0 & 0 & \cos(2\theta) \end{bmatrix}$$

Practically the M_i and a_i matrices are used to implement the transformations describe in Section creating three rotations corresponding to the three specified Euler angles (ϕ, θ, ψ). The total matrices M and a results in our case:

$$M = M_z M_x M_z$$

$$a = a_z a_x a_z$$

Once these matrices have been defined, the new properties can be calculated as:

$$C' = [M][c][M]^T$$

$$e' = [a][e][M]^T$$

$$\epsilon' = [a][\epsilon][a]^T$$

All these transformations were implemented in COMSOL in order to obtain the orientation of interest. The calculations of this method was numerically implemented in MATLAB as shown in the code below

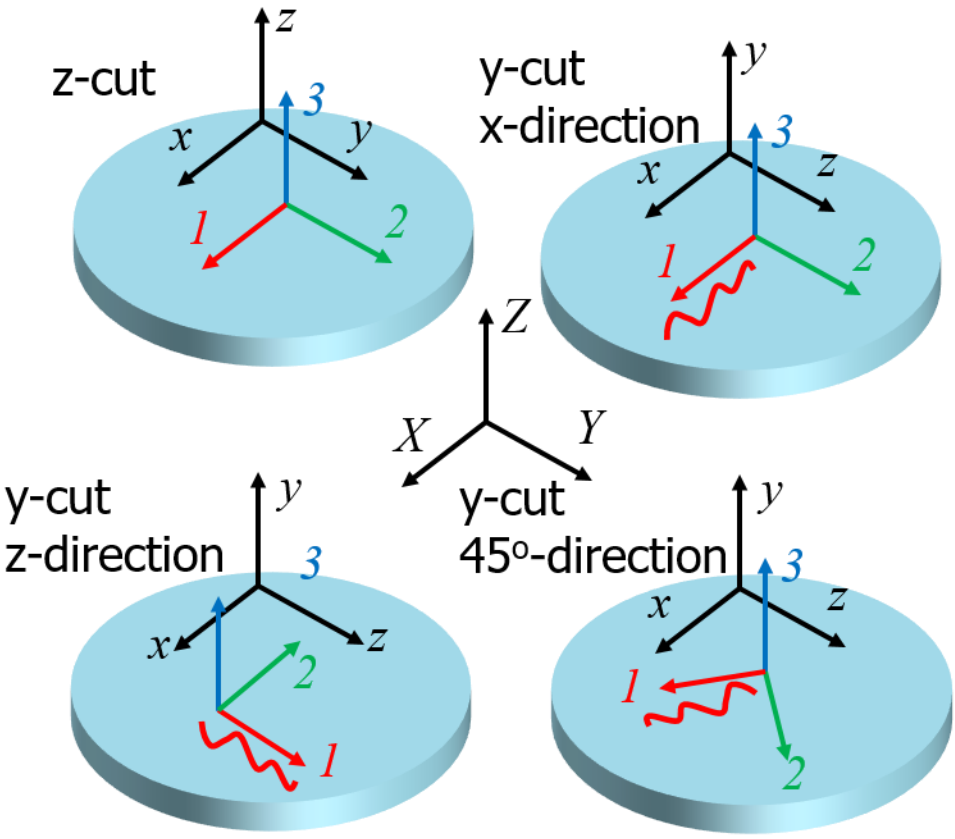


```
%% YZ theta CUT at theta = 0
%% YX theta CUT at theta = 90
%% Y45 theta CUT at theta = 45

z1 = 0;%
x = -90 * pi / 180;
z2 = (-90 + theta)* pi / 180;

%%
%% LiNbO3
%%Intial Z cut
c_LN = zeros(6,6);

c11 = 203;
c12 = 53;
c13 = 75;
c14 = 9;

c33 = 245;
c44 = 60;
c66 = 75;

c_LN(1,1) = c11;
c_LN(1,2) = c12;
c_LN(1,3) = c13;
c_LN(1,4) = c14;

c_LN(2,1) = c12;
c_LN(2,2) = c11;
c_LN(2,3) = c13;
```

```
c_LN(2,4) = -c14;

c_LN(3,1) = c13;
c_LN(3,2) = c13;
c_LN(3,3) = c33;

c_LN(4,1) = c14;
c_LN(4,2) = -c14;
c_LN(4,4) = c44;

c_LN(5,5) = c44;
c_LN(5,6) = c14;

c_LN(6,5) = c14;
c_LN(6,6) = c66;

c_LN = c_LN*1e9;



EP33_LN = zeros(3,3);

EP33_LN(1,1) = 45;
EP33_LN(2,2) = 45;
EP33_LN(3,3) = 27;

d36_LN = zeros(3,6);

d15 = 68e-12;
d22 = 21e-12;
d31 = -1e-12;
d33 = 6e-12;

d36_LN(1,5) = d15;
d36_LN(1,6) = -2*d22;

d36_LN(2,1) = -d22;
d36_LN(2,2) = d22;
d36_LN(2,4) = d15;

d36_LN(3,1) = d31;
d36_LN(3,2) = d31;
d36_LN(3,3) = d33;

E36_LN = d36_LN*c_LN;

P66_LN=zeros(6,6);

p11 = -0.026;
p12 = 0.09;
p13 = 0.133;
p14 = -0.075;
p31 = 0.179;
p33 = 0.071;
p41 = -0.151;
p44 = 0.146;
p66 = 0.5*(p11-p12);
```

```
P66_LN(1,1) = p11;
P66_LN(1,2) = p12;
P66_LN(1,3) = p13;
P66_LN(1,4) = p14;

P66_LN(2,1) = p12;
P66_LN(2,2) = p11;
P66_LN(2,3) = p13;
P66_LN(2,4) = -p14;

P66_LN(3,1) = p31;
P66_LN(3,2) = p31;
P66_LN(3,3) = p33;

P66_LN(4,1) = p41;
P66_LN(4,2) = -p41;
P66_LN(4,4) = p44;

P66_LN(5,5) = p44;
P66_LN(5,6) = p41;

P66_LN(6,5) = p14;
P66_LN(6,6) = p66;

r33 = 30.8e-12;
r13 = 8.6e-12;
r22 = 3.4e-12;
r51 = 28e-12;

r63_LN = zeros(6,3);
r63_LN(1,2) = -r22;
r63_LN(1,3) = r13;
r63_LN(2,2) = r22;
r63_LN(2,3) = r13;
r63_LN(3,3) = r33;
r63_LN(4,2) = r51;
r63_LN(5,1) = r51;
r63_LN(6,1) = -r22;

Dens_LN = 4.7e3;

L13 = [1 0 0];
L31 = L13';

epsilon_o = 8.85e-12;
%%
az1 = [cos(z1) sin(z1) 0;
   -sin(z1) cos(z1) 0;
   0          0      1];



ax = [1          0      0;
   0       cos(x) sin(x);
   0      -sin(x) cos(x)];

az2 = [cos(z2) sin(z2) 0;
```

```
   -sin(z2) cos(z2) 0;
   0          0      1];



Mz1 = [(cos(z1))^2 (sin(z1))^2    0        0            0       sin(2*z1);
   (sin(z1))^2 (cos(z1))^2    0        0            0      -sin(2*z1);
   0              0           1        0            0          0    ;

   0              0           0       cos(z1)    -sin(z1)      0    ;
   0              0           0       sin(z1)    cos(z1)       0    ;
   -sin(2*z1)/2   sin(2*z1)/2 0        0            0        cos(2*z1)
   ];



Mx = [1         0              0               0               0        0;
   0    (cos(x))^2   (sin(x))^2       sin(2*x)          0        0;
   0    (sin(x))^2   (cos(x))^2      -sin(2*x)          0        0;

   0    -sin(2*x)/2   sin(2*x)/2      cos(2*x)          0        0;
   0         0            0               0             cos(x)   -sin(x);
   0         0            0               0             sin(x)    cos(x)
   ];

Mz2 = [(cos(z2))^2 (sin(z2))^2    0        0            0       sin(2*z2);
   (sin(z2))^2 (cos(z2))^2    0        0            0      -sin(2*z2);
   0              0           1        0            0          0    ;

   0              0           0       cos(z2)    -sin(z2)      0    ;
   0              0           0       sin(z2)    cos(z2)       0    ;
   -sin(2*z2)/2   sin(2*z2)/2 0        0            0        cos(2*z2)
   ];

M = Mz2 * Mx * Mz1;
a = az2 * ax * az1;

c_dash = round((M * c_LN * M')/1e11, 4)*1e11;
E_dash = round(a * E36_LN * M', 4);
EPsilon_dash = round(a * EP33_LN * a', 4);
p_dash = round(M * P66_LN * M', 4);
r_dash = M * r63_LN * a';
peff = p_dash - r_dash*L31*L13*E_dash./(L13*EPsilon_dash*L31*epsilon_o);
```

APPENDIX B: ARW Derivation

Power spectral density (PSD) of Brownian noise is represented $PSD_{noise} = 4KT$ while Coriolis power$P_{cor} = \int F_{cor} \cdot dv$ where$F_{cor} = 2m_p v_{drv} \times \Omega$. From the definition of ARW:

$$ARW = \sqrt{\frac{PSD_{noise}}{P_{cor}}}\Omega$$

In a SAW resonator, the Coriolis mass (pillars) are continuously driven in an oscillatory motion a resonance. Solving the P_{cor}integral:

$$P_{cor} = \frac{1}{2} F_{cor} v_{sns}$$

For a Matched mode gyroscope, the sense resonator is operating at resonance frequency too where $x_{sns}$is given by:

$$x_{sns} = \frac{F_{cor}}{b\omega_{res}}$$

Substituting (2-3) in (1), ARW is represented by:

$$ARW = \frac{1}{x_{drv} m_p} \sqrt{\frac{2KTM_{res}}{\omega_{res} Q_{sns}}}$$

It is important to represent the ARW function in the input electrical power P_{in}which requires substituting with $x_{sns} = f(P_{in})$. Considering the conversion of electrical energy to mechanical energy $E_m = 1/2\ M_{res} v_{drv}^2$ and the definition of the total quality factor of the drive SAW resonator $Q_{drv} = \omega \frac{E_m}{P_{in}}, then$:

$$x_{drv} = \sqrt{\frac{2P_{in} Q_{drv}}{M_{res} \omega_{res}^3}}$$

Using (5), the ARW is rewritten as:

$$ARW = \omega \frac{M_{res}}{m_p} \sqrt{\frac{2KT}{Q_{drv} Q_{sns} P_{in}}}$$

APPENDIX C: Test setup solid modeling and designs

3-axis DUT holder

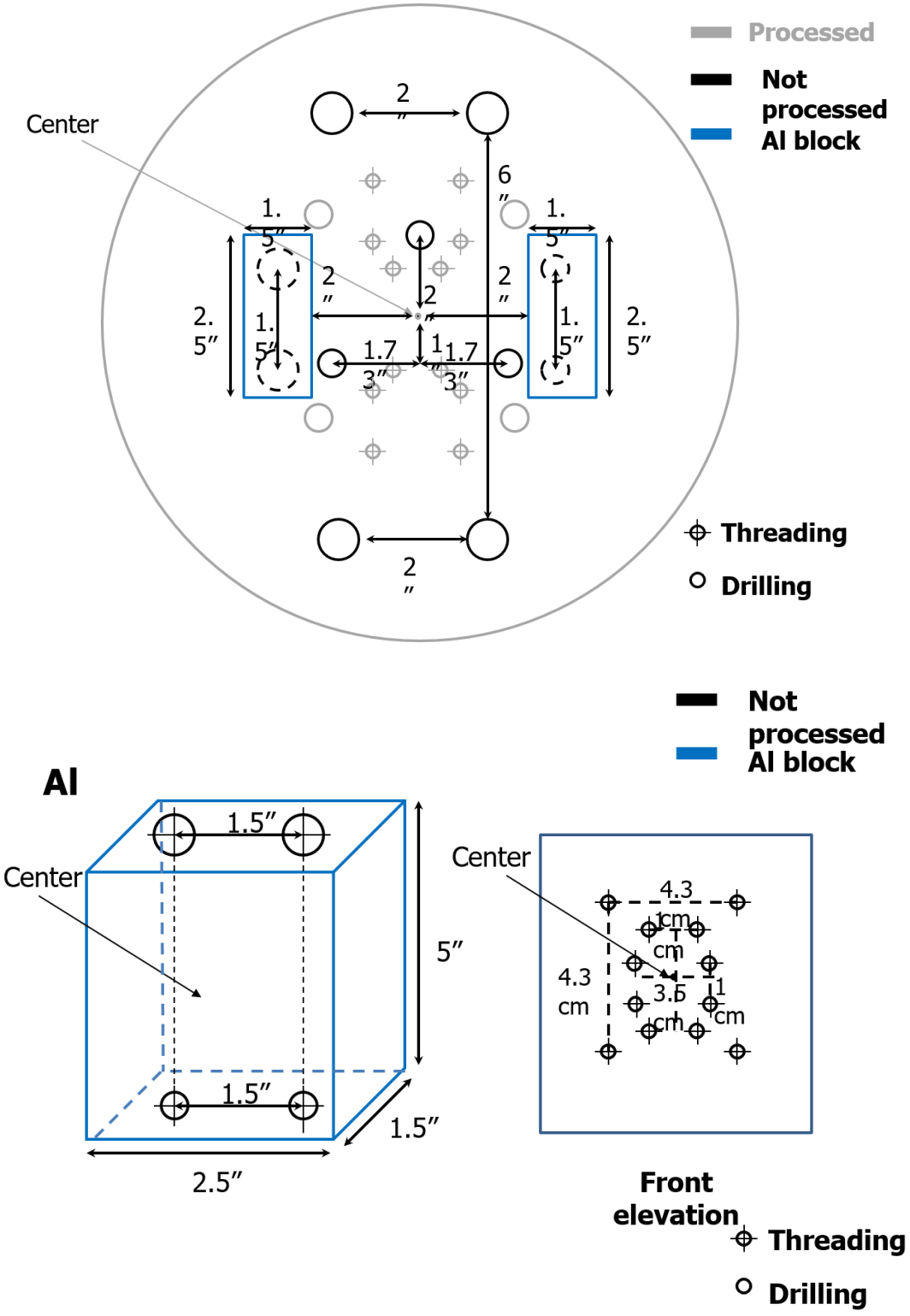

Integrated setup

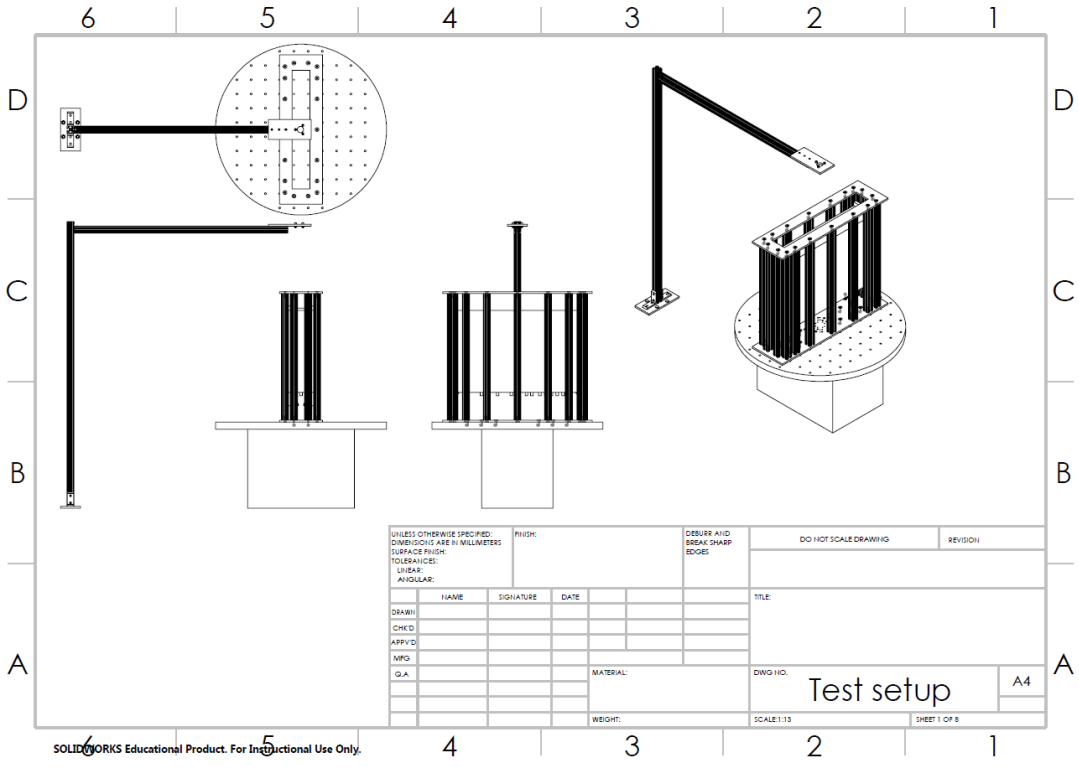
Test setup
A4
SOLIDWORKS Educational Product. For Instructional Use Only.

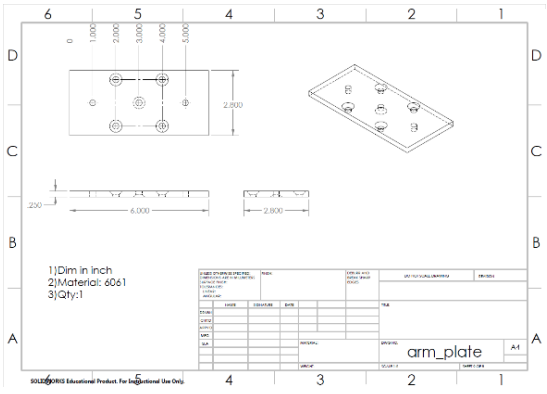
1)Dim in inch
2)Material: 6061
3)Qty:1
arm_plate
A4

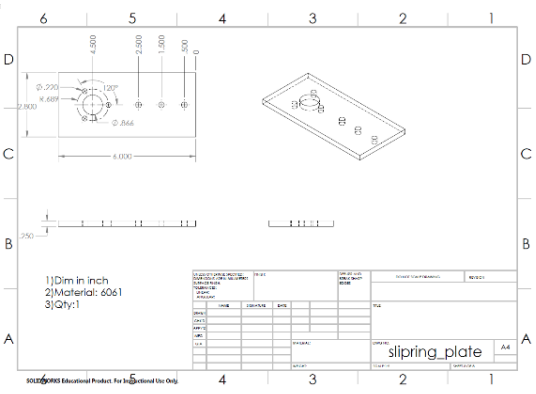
1)Dim in inch
2)Material: 6061
3)Qty:1
slipring_plate
A4

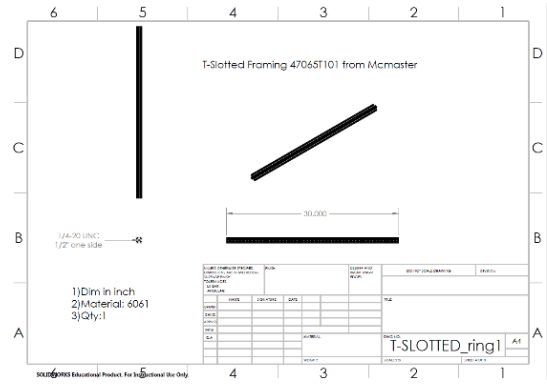
T-Slotted Framing 47065T101 from Mcmaster
1)Dim in inch
2)Material: 6061
3)Qty:1
T-SLOTTED_ring1
A4

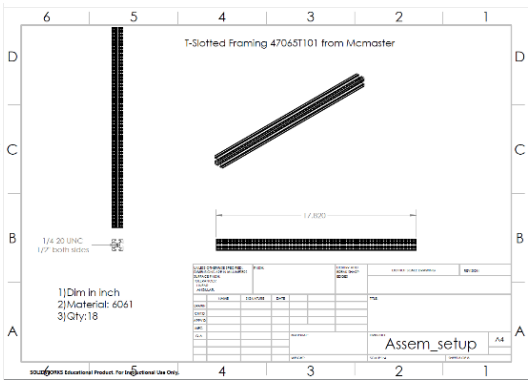
T-Slotted Framing 47065T101 from Mcmaster
1)Dim in inch
2)Material: 6061
3)Qty:18
Assem_setup
A4

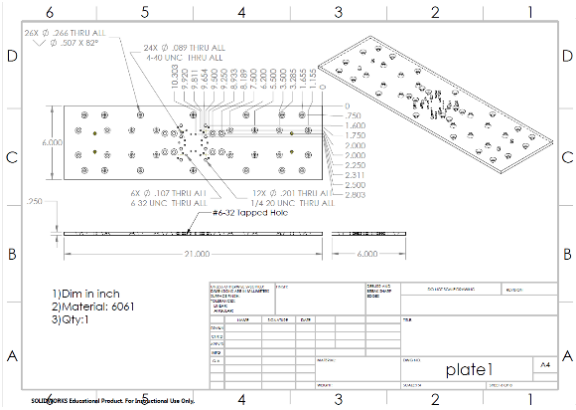
26X Ø .266 THRU ALL
Ø .507 X 82°
24X Ø .089 THRU ALL
4-40 UNC THRU ALL
6X Ø .107 THRU ALL
6-32 UNC THRU ALL
12X Ø .201 THRU ALL
1/4-20 UNC THRU ALL
#6-32 tapped Hole
21.000
6.000
1)Dim in inch
2)Material: 6061
3)Qty:1
plate1
A4
SOLIDWORKS Educational Product. For Instructional Use Only.

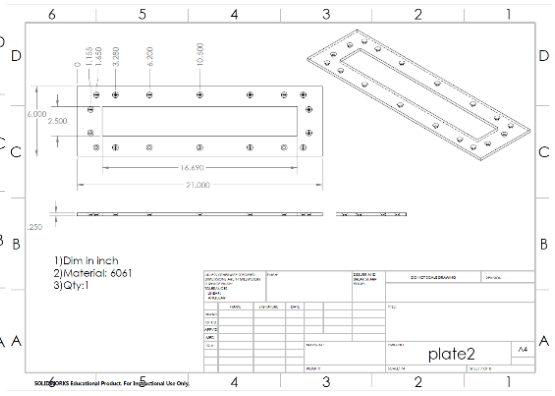
6.000
2.500
16.690
21.000
.250
1)Dim in inch
2)Material: 6061
3)Qty:1
plate2
A4
SOLIDWORKS Educational Product. For Instructional Use Only.

BIBLIOGRAPHY AND REFERENCES

[1] R. Dunn and others, “Ships, clocks and stars: The quest for longitude,” *Signals*, no. 115, p. 2, 2014.

[2] K. R. Britting, “Inertial navigation systems analysis.,” 1971.

[3] A. Annex, “Global Positioning System Standard Positioning Service Signal Specification.” Citeseer, 1995.

[4] M. Tanenhaus, D. Carhoun, T. Geis, E. Wan, and A. Holland, “Miniature IMU/INS with optimally fused low drift MEMS gyro and accelerometers for applications in GPS-denied environments,” in *Proceedings of the 2012 IEEE/ION Position, Location and Navigation Symposium*, 2012, pp. 259–264, doi: 10.1109/PLANS.2012.6236890.

[5] A. A. Trusov, I. P. Prikhodko, S. A. Zotov, and A. M. Shkel, “Low-dissipation silicon tuning fork gyroscopes for rate and whole angle measurements,” *IEEE Sens. J.*, vol. 11, no. 11, pp. 2763–2770, 2011.

[6] A. Grant, P. Williams, N. Ward, and S. Basker, “GPS Jamming and the Impact on Maritime Navigation,” *J. Navig. - J NAVIG*, vol. 62, 2009, doi: 10.1017/S0373463308005213.

[7] R. Polcawich, “Precise Robust Inertial Guidance for Munitions (PRIGM),” in *DARPA*.

[8] A. Devices, “No TitleHigh Performance, SPI Digital Output, Angular Rate Sensor ADXRS800.” [Online]. Available: https://www.analog.com.

[9] Y. Zhao, A. Ping Qiu, Q. Shi, and G. Ming Xia, “Sub-degree per hour split mode tuning fork gyroscope,” in *2016 IEEE International Symposium on Inertial Sensors and Systems*, 2016, pp. 115–116, doi: 10.1109/ISISS.2016.7435559.

[10] X. Yu, W. Lei, Z. Fan, and G. Lu, “A miniature low cost ring laser gyroscope inertial measurement unit,” in *2016 6th IEEE International Conference on Control System, Computing and Engineering (ICCSCE)*, 2016, pp. 7–9.

[11] D. M. Rozelle, A. D. Meyer, A. A. Trusov, and D. K. Sakaida, “Milli-HRG inertial sensor assembly – a reality,” in *2015 IEEE International Symposium on Inertial Sensors and Systems (ISISS) Proceedings*, 2015, pp. 1–4, doi: 10.1109/ISISS.2015.7102386.

[12] M. Kurosawa, Y. Fukuda, M. Takasaki, and T. Higuchi, “A surface-acoustic-wave gyro sensor,” *Sensors Actuators A Phys.*, vol. 66, no. 1–3, pp. 33–39, 1998.

[13] Q. Liu and X. Wu, “Design of a Novel MEMS IDT Dual Axes Surface Acoustic Wave Gyroscope,” in *2007 2nd IEEE International Conference on Nano/Micro Engineered and Molecular Systems*, 2007, pp. 817–820, doi: 10.1109/NEMS.2007.352143.

[14] A. Mahmoud, L. Cai, J. Bain, T. Mukherjee, and G. Piazza, “Acousto-Optic Gyroscope with Improved Sensitivity and 100 second Stability in a Small Form Factor,” in *2019 IEEE International Symposium on Inertial Sensors and Systems (INERTIAL)*, 2019, pp. 1–4, doi: 10.1109/ISISS.2019.8739521.

[15] M. Kurosawa, Y. Fukuda, M. Takasaki, and T. Higuchi, “A surface acoustic wave gyro sensor,” in *Proceedings of International Solid State Sensors and Actuators Conference (Transducers ’97)*, 1997, vol. 2, pp. 863–866 vol.2, doi: 10.1109/SENSOR.1997.635238.

[16] R. C. Woods, H. Kalami, and B. Johnson, “Evaluation of a novel surface acoustic wave gyroscope,” *IEEE Trans. Ultrason. Ferroelectr. Freq. Control*, vol. 49, no. 1, pp. 136–141, 2002.

[17] V. K. Varadan, W. D. Suh, P. B. Xavier, K. A. Jose, and V. V Varadan, “Design and development of a MEMS-IDT gyroscope,” *Smart Mater. Struct.*, vol. 9, no. 6, p. 898, 2000.
[18] Q. Liu, X. Wu, D. Di, P. Dong, and D. Fan, “Design of a novel MEMS IDT dual axes surface acoustic wave gyroscope,” in *2009 4th IEEE International Conference on Nano/Micro Engineered and Molecular Systems*, 2009, pp. 889–892.
[19] S. W. Lee, J. W. Rhim, S. W. Park, and S. S. Yang, “A micro rate gyroscope based on the SAW gyroscopic effect,” *J. Micromechanics Microengineering*, vol. 17, no. 11, p. 2272, 2007.
[20] N. Yazdi, F. Ayazi, and K. Najafi, “Micromachined inertial sensors,” *Proc. IEEE*, vol. 86, no. 8, pp. 1640–1659, 1998.
[21] A. Mahmoud, M. Mahmoud, T. Mukherjee, and G. Piazza, “Investigating the impact of resonant cavity design on surface acoustic wave gyroscope,” in *2018 IEEE International Symposium on Inertial Sensors and Systems (INERTIAL)*, 2018, pp. 1–4, doi: 10.1109/ISISS.2018.8358137.
[22] A. Mahmoud, T. Mukherjee, and G. Piazza, “Novel Acoustic Gratings with High Reflection Constant for Surface Acoustic Wave Gyroscopes,” in *2018 IEEE International Ultrasonics Symposium (IUS)*, 2018, pp. 206–212, doi: 10.1109/ULTSYM.2018.8579999.
[23] A. Mahmoud *et al.*, “Acousto-optic gyroscope,” in *2018 IEEE Micro Electro Mechanical Systems (MEMS)*, 2018, pp. 241–244, doi: 10.1109/MEMSYS.2018.8346529.
[24] M. Mahmoud *et al.*, “Novel on chip rotation detection based on the acousto-optic effect in surface acoustic wave gyroscopes,” *Opt. Express*, vol. 26, no. 19, pp. 25060–25075, Sep. 2018, doi: 10.1364/OE.26.025060.
[25] G. P. Ashraf Mahmoud, Tamal Mukherjee, “INVESTIGATING LONG-TERM STABILITY OF WIDE BANDWIDTH SURFACE ACOUSTIC WAVES GYROSCOPES USING A MONOLITHICALLY INTEGRATED MICRO-OVEN,” in *Micro Electro Mechanical Systems*, 2020.
[26] M. Mahmoud, S. Ghosh, and G. Piazza, “Lithium niobate on insulator (LNOI) grating couplers,” in *CLEO: Science and Innovations*, 2015, pp. SW4I--7.
[27] J. Xu and R. Stroud, *Acousto-optic devices: principles, design, and applications*, vol. 12. Wiley-Interscience, 1992.
[28] R. M. White, “Surface elastic-wave propagation and amplification,” *IEEE Trans. Electron Devices*, vol. 14, no. 4, pp. 181–189, 1967.
[29] B. A. Auld, “Rayleigh wave propagation,” in *Rayleigh-Wave Theory and Application*, Springer, 1985, pp. 12–28.
[30] M. Zhang, C. Wang, R. Cheng, A. Shams-Ansari, and M. Lončar, “Monolithic ultra-high-Q lithium niobate microring resonator,” *Optica*, vol. 4, no. 12, pp. 1536–1537, 2017.
[31] L. Cai, A. Mahmoud, and G. Piazza, “Low-loss waveguides on Y-cut thin film lithium niobate: towards acousto-optic applications,” *Opt. Express*, vol. 27, no. 7, pp. 9794–9802, 2019.
[32] R. M. White and F. W. Voltmer, “Direct piezoelectric coupling to surface elastic waves,” *Appl. Phys. Lett.*, vol. 7, no. 12, pp. 314–316, 1965.
[33] C. K. Campbell, “Obtaining the fundamental and harmonic radiation conductances of a reflective SAW interdigital transducer,” in *1998 IEEE Ultrasonics Symposium. Proceedings (Cat. No. 98CH36102)*, 1998, vol. 1, pp. 169–173.
[34] P. V Wright, “Reflectionless transducer.” Google Patents, 1990.
[35] S. Datta and B. J. Hunsinger, “First-order reflection coefficient of surface acoustic

waves from thin-strip overlays," *J. Appl. Phys.*, vol. 50, no. 9, pp. 5661–5665, 1979.
[36] B. K. Sinha and H. F. Tiersten, "Variational analysis of the reflection of surface waves by arrays of reflecting strips," *J. Appl. Phys.*, vol. 47, no. 7, pp. 2824–2832, 1976.
[37] M. T. Wauk and others, "Attenuation in microwave acoustic transducers and resonators.," 1969.
[38] B. A. Auld, *Acoustic fields and waves in solids*, vol. 8, no. 1. 1975.
[39] T. Yoneyama and S. Nishida, "Reflection and transmission of Rayleigh waves by the edge of a deposited thin film," *J. Acoust. Soc. Am.*, vol. 55, no. 4, pp. 738–743, 1974.
[40] C. Campbell, *Surface Acoustic Wave Devices for Mobile and Wireless Communications, Four-Volume Set*. Academic press, 1998.
[41] G. Hernández, *Fabry-perot interferometers*, no. 3. Cambridge University Press, 1988.
[42] W. E. Newell, "Surface wave piezoelectric resonator." Google Patents, 1970.
[43] W. P. Mason, "Physical acoustics and the properties of solids," *J. Acoust. Soc. Am.*, vol. 28, no. 6, pp. 1197–1206, 1956.
[44] H. A. Haus, "Modes in SAW grating resonators," *Electron. Lett.*, vol. 13, no. 1, pp. 12–13, 1977.
[45] K. S. Van Dyke, "The piezo-electric resonator and its equivalent network," *Proc. Inst. Radio Eng.*, vol. 16, no. 6, pp. 742–764, 1928.
[46] R. C. M. Li, R. C. Williamson, D. C. Flanders, and J. A. Alusow, "On the performance and limitations of the surface-wave resonator using grooved reflectors," in *1974 Ultrasonics Symposium*, 1974, pp. 257–262.
[47] A. J. Slobodnik, "Surface acoustic waves and SAW materials," *Proc. IEEE*, vol. 64, no. 5, pp. 581–595, May 1976, doi: 10.1109/PROC.1976.10180.
[48] K. Hashimoto and K.-Y. Hashimoto, *Surface acoustic wave devices in telecommunications*. Springer, 2000.
[49] H.-S. Tuan, "On bulk waves excited at a groove by Rayleigh waves," *J. Appl. Phys.*, vol. 46, no. 1, pp. 36–41, 1975.
[50] R. C. M. Li and J. A. ALUSOW, "Suppression of bulk-scattering loss at s.a.w.-resonator reflectors," *Electron. Lett.*, vol. 13, no. 19, pp. 580–581, 1977, doi: 10.1049/el:19770414.
[51] Y. Ebata, "Suppression of bulk-scattering loss in SAW resonator with quasi-constant acoustic reflection periodicity," in *IEEE 1988 Ultrasonics Symposium Proceedings.*, 1988, pp. 91–96 vol.1, doi: 10.1109/ULTSYM.1988.49348.
[52] Roditi, "Lithium Niobate Wafers." [Online]. Available: http://www.roditi.com/SingleCrystal/LiNbO3/LiNbO3-Wafers.html.
[53] M. Mahmoud, "Design, Fabrication, and Characterization of Monolithically Integrated Acoustic and Photonic Devices on Lithium Niobate Over Insulator (LNOI) Platform," Carnegie Mellon University, 2018.
[54] E. Tatar, "On-Chip Compensation of Stress, Temperature, and Nonlinearity in a MEMS Gyroscope," Carnegie Mellon University, 2016.
[55] "Norland Optical Adhesive 61." [Online]. Available: https://www.norlandprod.com/adhesives/NOA 61.html.
[56] Z. INSTRUMENTS, "UHFLI Lock-In Amplifier [online]{\copyright} 2012 [cit. 27.5. 2012]," *Dostupné z http//www. zhinst. com/docs/leaflets/zi_uhfli_leaflet. pdf*.
[57] D. Valério and J. S. Da Costa, "Tuning of fractional PID controllers with Ziegler--Nichols-type rules," *Signal Processing*, vol. 86, no. 10, pp. 2771–2784, 2006.
[58] A. Modules, "HIGH BANDWIDTH BIPOLAR TRANSIMPEDANCE

AMPLIFIER." [Online]. Available: https://www.analogmodules.com/admincenter/datasheets/313a.pdf.
[59] A. A. Trusov, "Allan Variance Analysis of Random Noise Modes in Gyroscopes," Ph. D. Thesis, University of California, Irvine, CA, USA, 2011.
[60] Compugraphic, "No Title." [Online]. Available: https://www.compugraphics-photomasks.com/us/.
[61] F. Li *et al.*, "Giant piezoelectricity of Sm-doped Pb (Mg1/3Nb2/3) O3-PbTiO3 single crystals," *Science (80-.).*, vol. 364, no. 6437, pp. 264–268, 2019.